TÉCNICO LISBOA

UNIVERSIDADE DE LISBOA
INSTITUTO SUPERIOR TÉCNICO

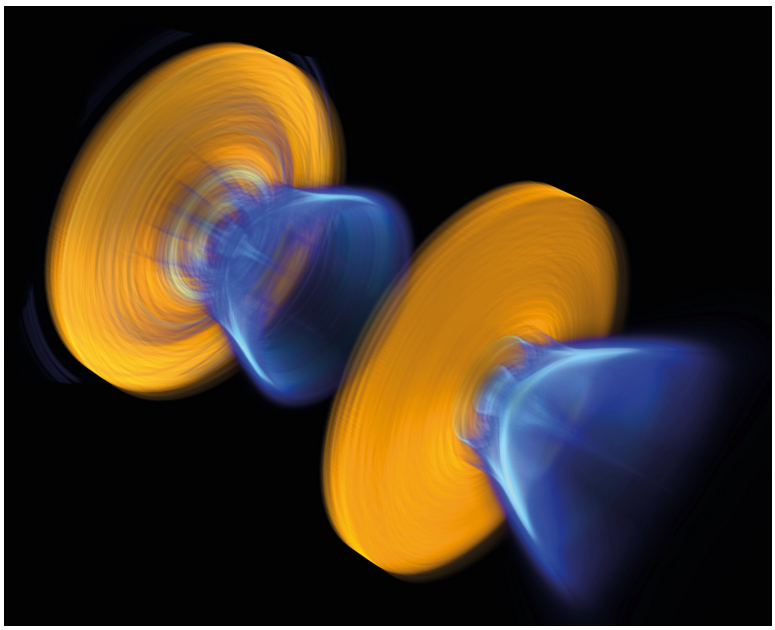

Superradiant and coherent radiation emission in plasma accelerator light sources

Bernardo Farinha Malaca

Supervisor: Doctor Jorge Miguel Ramos Domingues Ferreira Vieira
Co-supervisor: Doctor Ricardo Parreira de Azambuja Fonseca

Thesis approved in public session to obtain the PhD Degree in

Technological Physics Engineering

Jury final classification: Pass with Distinction

2024

UNIVERSIDADE DE LISBOA
INSTITUTO SUPERIOR TÉCNICO

Superradiant and coherent radiation emission in plasma accelerator light sources

Bernardo Farinha Malaca

Supervisor: Doctor Jorge Miguel Ramos Domingues Ferreira Vieira
Co-Supervisor: Doctor Ricardo Parreira de Azambuja Fonseca

Thesis approved in public session to obtain the PhD Degree in

Technological Physics Engineering

Jury final classification: Pass with Distinction

Jury

Chairperson: Doctor Luís Miguel de Oliveira e Silva, Instituto Superior Técnico, Universidade de Lisboa
Members of the Committee:
Doctor Luís Miguel de Oliveira e Silva, Instituto Superior Técnico, Universidade de Lisboa
Doctor Cédric Thaury, CNRS, ENSTA, École Polytechnique, Institut Polytechnique de Paris, França
Doctor Andreas Döpp, Faculty of Physics, Ludwig Maximilian University Munich, Alemanha
Doctor Jorge Miguel Ramos Domingues Ferreira Vieira, Instituto Superior Técnico, Universidade de Lisboa

Funding Institution
FCT: Fundação para a Ciência e a Tecnologia

2024

Resumo

Os aceleradores baseados em plasma podem agora criar feixes de electrões com uma qualidade muito elevada e recentemente cientistas alcançaram o objetivo de gerar luz muito brilhante em lasers de electrões-livres a partir destes feixes. Os lasers com perfil espaço-temporal estão agora a começar a atingir a maturidade e, portanto, a comunidade de física dos plasmas deve estudar as potenciais aplicações de tais feixes. O nosso trabalho consiste em novas formas de gerar luz muito brilhante a partir de configurações típicas de aceleração de plasma, tanto impulsionadas por laser como por feixe. Demonstramos que, utilizando perfis de densidade específicos, qualquer configuração de aceleração de plasma pode transformar-se num emissor de radiação coerente. Os perfis de corrente muito curtos que surgem nos campos de ondas propagam-se como uma única entidade, que denominamos quase-partícula. Demonstramos que poderíamos obter radiação de banda larga até ao ultra-violeta extremo (EUV) com uma luminosidade muito elevada. A criação de modulações periódicas do perfil de densidade fez com que a quase-partícula emita radiação de banda estreita no EUV. Também implementamos lasers espaço-temporais no código de partículas em célula OSIRIS, um dos códigos mais utilizados na comunidade. Ao utilizar estes impulsos em simulações, estudamos o impacto na geração de radiação e aceleração. Controlar a força ponderomotiva dá-nos acesso a novos regimes de Thomson *scattering* que brilham mais. A utilização destes lasers também pode gerar quase partículas sem a necessidade de perfis de densidade específicos. Por último, mostramos como acoplar um feixe de electrões, plasma e um laser espaço-temporal para gerar oscilações betatrão temporalmente coerentes. Este trabalho pode levar à emissão de raios-X de ciclo-único utilizando configurações de plasma.

Palavras-chave: Simulações Numéricas; Aceleradores de Partículas a Plasma; Feixes Espácio-temporais; Radiação Coerente; Superradiância

Title: Superradiant and coherent radiation emission in plasma accelerator light sources

Abstract

Plasma-based accelerators can now create electron beams with very high quality and have reached the goal of generating very bright light in free-electron lasers. Lasers with spatiotemporal shaping are now beginning to reach maturity, and therefore the plasma community must study the potential applications of such beams. Our work consists of new ways of generating very bright light from regular plasma acceleration setups, both laser-driven and beam-driven. We show that by using specific density profiles, any plasma acceleration setup may turn into a coherent radiation emitter. The very short current profiles that surge within the wakefields radiate as a single entity, which we labeled quasiparticle. We proved we could get broadband radiation up to the EUV at very high brightness. Creating periodical modulations of the density profile made the quasiparticle emit narrowband radiation at the EUV. We also implemented spatiotemporal lasers into the particle-in-cell code OSIRIS, one of the most used codes in the plasma community. By using these pulses in simulations, we studied the impact on radiation generation and acceleration. Controlling the ponderomotive force gives us access to new Thomson scattering regimes that shine brighter. Using these lasers we can generate quasiparticles without the need for specific density profiles. Lastly, we showed how to couple an electron beam, plasma, and a spatiotemporal laser to generate start temporally coherent betatron oscillations. This work may lead to single-cycle X-ray emission using plasma setups.

Keywords: Numerical Simulations; Plasma-Based Accelerators; Spatiotemporal shaped beams; Coherent radiation; Superradiance

Acknowledgements

I extend my deepest gratitude to all those who have contributed to the completion of this thesis.

First and foremost, I would like to express my sincere appreciation to Jorge Vieira and Ricardo Fonseca, for their invaluable guidance, great ideas, and insightful feedback throughout the entirety of this research. Your expertise, patience, and encouragement were instrumental in shaping this work.

I am also immensely grateful to GoLP (group of lasers and plasmas) for their collaborative spirit, stimulating discussions, and collective efforts, which have enriched my academic journey and broadened my perspectives. A special thanks go to my office mates: Robert, Miguel, Diogo, Filipe and Pablo, for putting up with me as long as you did. Thanks to Chiara and Rafael for reminding me of parts of this thesis I had already forgotten about. Thanks to Thales for watching all the Youtube videos so you could play pool as well as you did.

I have also to thank John Palastro, those 3 months felt way longer than that and it is one of the experiences I have ever been a part of. Thank you for your trust, your excellent (and quick!) feedback, and expertise.

To Dillon, Tanner, for all the golf games, pool matches and physics discussions. In that order.

I extend heartfelt thanks to the members of the jury, Andreas Döpp, Cédric Thaury, and Luís Oliveira e Silva, for the time spent reading and for the entertaining questions they posed during the thesis defense.

Special appreciation goes to my family for their boundless love, encouragement, and understanding. Their unwavering support and sacrifices has been the cornerstone of my academic pursuits, and I am profoundly grateful for their presence in my life. Thanks to my parents for the Monday night dinners, and thanks to my brothers for the overnight haxball matches.

To my girlfriend, Rita, I owe a debt of gratitude beyond words. Your unwavering belief in me, your patience, and your unconditional love have been my guiding lights throughout this journey. Your encouragement and understanding have lifted me up in

moments of doubt and celebration alike. Thank you for being my rock, and my source of joy. Your presence has made every step of this academic endeavor more meaningful and fulfilling.

I also wish to acknowledge the use of ISTcluster at IST, Marenostrum in Spain, and Lumi in Finland.

Thank you all for being part of this journey and for helping me realize this milestone in my academic career.

This thesis is a total human work and did not use any LLM throughout.

Contents

List of Figures

CHAPTER 1

INTRODUCTION

1.1 OVERVIEW

Bright radiation sources have led to advancements in a myriad of disciplines, such as ultrafast biology [1], chemistry [2], material science [3], radiotherapy [4], and quantum electrodynamics. The facilities around the world that produce the brightest radiation pulses can agglomerate many scientists and serve as a multi-disciplinary endeavor, such as DESY (stands for the Deutsches Synchroton, or the german synchrotron), or ELI (Extreme Light Infrastructure). Plasma scientists have shown over the last decades the possibility of decreasing the size of accelerators by several orders of magnitude. Since radiation production always involves particle acceleration, it should also be possible to miniaturize radiation facilities using compact plasma accelerators. This thesis concerns simple modifications to plasma acceleration setups and to lasers that can help create superradiant, coherent light sources at a fraction of the length (and cost).

The introduction provides a brief description of the main concepts of this work, from plasma accelerators to conventional radiation sources and numerical methods used.

1.2 PLASMA ACCELERATORS

Radiofrequency (RF) cavities are the conventional accelerating accelerating mechanism in accelerators worldwide. They can produce very energetic, low emittance particle beams, and have a very high work capacity. The accelerating electric fields are created by resonant waves inside the cavities, which are made out of metal or a superconducting material. Because high electric fields damage the material, the maximum accelerating field is below 100 MeV/m, with the typical value 10 times smaller

[5]. Hence, the ability to accelerate electrons to the GeV range using this technology requires accelerating facilities with 0.1-1 km lengths.

To miniaturize accelerators, one requires a material to withstand very large electric fields. Plasmas are a very promising alternative, as the typical electric fields sustained by plasma are given by [6]:

$$E_0[\mathrm{V/m}] \approx 96\sqrt{n_0[\mathrm{cm}^{-3}]}, \tag{1.1}$$

where n_0 is the plasma density. Therefore, the accelerating fields can reach the GeV/m in typical laboratory plasmas with density of the order of $n_0 = 10^{18}\mathrm{cm}^{-3}$, which represents a major improvement over the conventional accelerator techniques.

Plasma acceleration uses relativistic wakefields as the medium of acceleration. The driver of these wakefields can both be ultra-intense lasers or ultra-relativistic particle bunches. For particle acceleration, we are mostly interested in cases where nonlinear plasma waves surge, which is commonly known as the bubble regime [7], shown in Fig. 2.6. Even though the laser-driven or beam-driven wakefields are similar in many aspects, the physical processes behind them vary slightly.

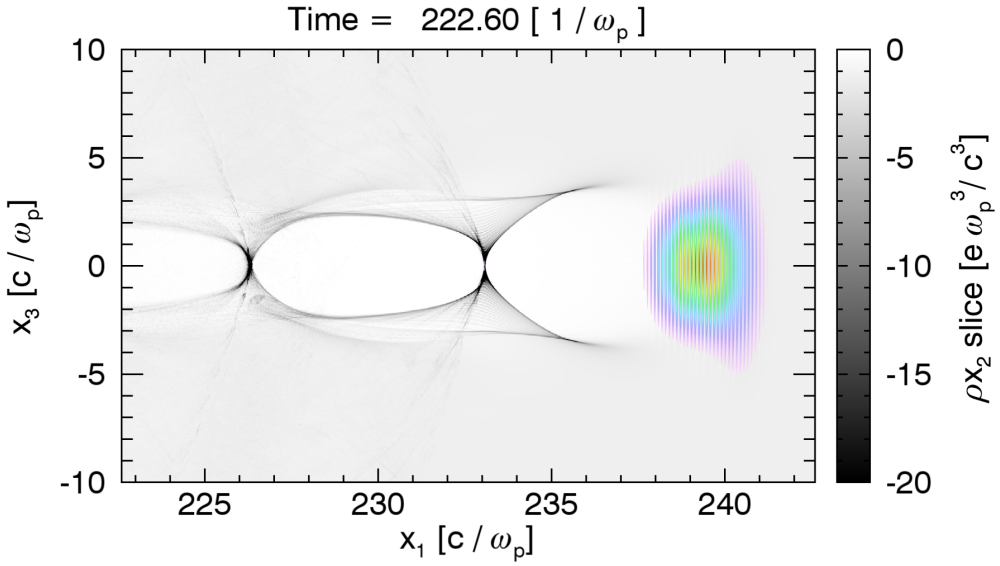

FIGURE 1.1: Nonlinear wakefield driven by a laser pulse (in rainbow colors)

In an LWFA (laser wakefield acceleration) regime [6, 8], the laser exerts a ponderomotive force onto the plasma electrons, which pushes them out of the propagation axis and leaves a positive charge region behind the laser. This region of positive charge works both as a focusing and accelerating medium for electrons, which makes

it an extraordinary accelerating mechanism. In a PWFA (plasma wakefield acceleration) regime [9, 10, 11], an ultra-relativistic particle beam exerts an electrostatic force onto the plasma electrons, pushing them out and creating a plasma wakefield that is similar to the LWFA case.

This nonlinear wakefield propagates at a phase velocity that corresponds to the speed of the driver of the wakefield (laser or particle beam), which is very close to the speed of light. Relativistic electrons in the bubble can become phase-locked with the wakefield and therefore accelerate to very large energies. There are multiple schemes to inject electrons into the bubble, such as external injection (where a conventional electron beam travels behind the driver), self-injection (where electrons from the sheath move into the wakefield), down-ramp injection (where a local dip in density leads to many electrons entering the wakefield at the same time) [12], ionization injection (where two gases coexist and one high-frequency laser travels behind the driver and ionize the secondary gas locally), some of which lead to accelerated bunches with high quality.

1.3 Radiation from plasma-based setups

In the realm of electromagnetic theory, light emission is fundamentally tied to the acceleration of charged particles. The nature of this emitted light — its frequency, intensity, and other characteristics — varies with the trajectory of the accelerating charges. To achieve high brightness, a common technique involves the use of particle beams, which aggregate many charged particles. This approach inherently results in higher radiation output compared to a single particle, due to the cumulative effect of multiple radiative sources. Following the principle of charged particle acceleration, plasmas serve as a powerful medium for generating high electromagnetic fields, facilitating a wide array of particle trajectories. These intense fields can dramatically alter the motion of charged particles, leading to a variety of light emissions across the electromagnetic spectrum. The manipulation of particle paths in high-field environments allows for the engineering of specific light characteristics, from the infrared to X-rays, depending on the particle energy and acceleration. This capacity to control particle trajectories within plasmas paves the way for precise manipulation of light emissions, opening up broad possibilities for both scientific exploration and technological innovation [13]. This section will introduce four different light sources that use plasmas.

1.3.1 Thomson Scattering

Thomson scattering is a laser-beam or laser-plasma interaction that can produce tunable, near-monochromatic, short x-ray pulses [14, 15]. In Thomson back-scattering, as an electron counter-propagates a laser pulse, it oscillates in the electromagnetic field

in a figure-8 motion, recently measured experimentally [16]. The emitted radiation depends on the normalized vector potential a_0, given by:

$$a_0 = \frac{eE}{\omega m_e c}, \tag{1.2}$$

where e, m_e, c, and E are the electron charge, electron mass, the speed of light and the maximum electric field. For small laser intensities ($a_0 \ll 1$), the electron oscillates at the laser frequency in its frame, and therefore the emitted radiation frequency matches the double Doppler-shifted laser frequency. However, as the normalized vector potential a_0 increases ($a_0 > 1$), the interaction becomes nonlinear, and the electron oscillates at harmonics of the laser frequency and therefore the radiated photons on-axis are of frequencies $\omega = nM_0\omega_0$, where

$$M_0 = \begin{cases} \gamma_0^2(1+\beta_0)^2/(1+a_0^2/2), & \text{e}-\text{beam} \\ 1, & \text{plasma} \end{cases}, \tag{1.3}$$

where the γ_0, $c\beta_0$, and a_0 are the electron Lorentz factor, the speed of electrons, and the laser normalized vector potential, respectively. The $(1+\beta_0)^2$ factor is the double-doppler shift that one observes in the lab frame.

When $a_0^2 \ll 1$ only the fundamental frequency is emitted. When $a_0^2 \gg 1$, the harmonical content expands up to a critical harmonical number $n_c \sim a_0^3$. In the case of laser-beam interaction, we exploit the relativistic factor γ and use ultra-relativistic beams to get a good monochromatic source (using $a_0^2 \ll 1$). However, in the laser-plasma interaction, one must use large a_0 (since $\gamma = 1$) and emit high frequencies. This radiation is incoherent, as the electrons in the beam or the plasma start at random phases in the laser fields.

If the laser photons are large enough to affect the motion of the electron, this is considered Compton scattering.

1.3.2 Betatron Radiation

In laser wakefield or plasma wakefield setups, the ion bubble provides a focusing region for electrons. Any particle beam travelling inside the ion bubble will then oscillate. For plasma wakefield setups, even the tail of the driver beam starts to oscillate as it propagates through plasma [17, 18]. For both LWFA [19] and PWFA, if there are electrons injected into the bubble they will also oscillate. These oscillations are called betatron oscillations. The betatron oscillation frequency ω_β is given by

$$\omega_\beta = \frac{\omega_p}{\sqrt{2\gamma}}, \tag{1.4}$$

where ω_p is the plasma frequency and γ is the electron Lorentz factor. Even though betatron radiation is temporally incoherent, it is spatially coherent. Spatial coherency

is determined by how electrons in the same transverse slice of the particle beam are coherent. Therefore, by using both a spatial filter (pinhole) and a spectral filter (beryllium window), betatron radiation coming from laser-plasma acceleration can already image a human bone [20]. Betatron radiation can also be used as a diagnostic for the transverse emittance of the accelerated electron beam in plasma acceleration setups [21].

1.3.3 Coherent Transition Radiation

As an electron bunch moves through a metal-vacuum boundary, the different speeds of electromagnetic waves in those materials make the electron accelerate near the boundary. If these particles arrive in a short bunch, then the particles radiate coherently for wavelengths larger than the bunch length and incoherently for shorter wavelengths [22]. This property can be readily seen on the emitted spectrum as a sharp intensity cutoff at a frequency that is characteristic of the bunch duration.

For a cylindrical symmetric electron beam with N electrons, the energy E emitted at frequency ω along θ is given by[23]:

$$\frac{d^2E}{d\omega d\Omega} = \left\langle \frac{d^2E_e}{d\omega d\Omega} \right\rangle \left[N + N^2 \left| F(\omega, \theta) \right| \right], \tag{1.5}$$

where ω is the frequency, Ω is the solid angle, θ is the emission angle, $\left\langle \frac{d^2E_e}{d\omega d\Omega} \right\rangle$ is the average of the single electron emission. The function $F(\omega, \theta) = \int n_e(\boldsymbol{x}) e^{-i\mathbf{k}\cdot\mathbf{x}} d\boldsymbol{x}$ is the three-dimensional Fourier transform of the charge distribution $n_e(\boldsymbol{x})$, where $\mathbf{k}$ is the wavevector and $\mathbf{x}$ are the spatial coordinates. The incoherent part of Eq. 1.5 is proportional to N, whereas the coherent bit goes with N^2. Even at a small charge of 1 pC, the coherent bit is about 6×10^6 larger than the incoherent one.

The coherent transition radiation diagnostic takes the spectral content from the electron beam to reconstruct $n_e(\boldsymbol{x})$. Usually, if one captures frequencies of $\lambda = 1\mu$m at a much higher brightness than $\lambda = 0.1\mu$m, the charge density must have some modulation at 1μm. Because one can only get access to the magnitude of F (and not the phase), assumptions on the spectrum have to be made to allow full reconstruction[13].

1.3.4 Free Electron laser driven by plasma accelerators

Free electron lasers are the brightest X-ray sources in the world. Recently, proof-of-concept experiments demonstrated free electron lasers operating with plasma-accelerated electron bunches. Both LWFA[24, 25] and PWFA [26] driven free-electron lasers could operate in the gain regime. These were major breakthroughs for the field, as plasma accelerators replaced conventional accelerators in one of the most desired applications.

A free-electron laser consists of a particle beam that oscillates in a periodic magnetic array (undulator) which wiggles the ultra-relativistic electron beam. If the magnetic field is B_0 and the undulator period is λ_u, the radiation is emitted at the wavelength[13]:

$$\lambda = \frac{\lambda_u}{2\gamma^2}\left(1 + \frac{K_0^2}{2}\right), \tag{1.6}$$

where $K_0 = 0.934 B_0[\mathrm{T}]\lambda_u[\mathrm{cm}]$ is the undulator strength parameter. If $K_0 > 1$ harmonics of that fundamental frequency also are emitted. As the radiation is emitted by the whole beam, the same radiation starts interacting with that beam. Depending on the phase difference between the electrons and the wave, these electrons either gain or lose energy, and an instability surges such that the beam becomes micro-bunched at emitted wavelength λ (the electron microbunches stay in the nodes of the amplified wave). As it modulates into microbunches, the beam starts emitting coherently, which results in an exponential amplification (gain regime) that only stops after saturation.

If the bunch is taken without previous modulation, the amplification starts from noise in the electron beam production. To make the process faster, facilities can seed the elect ron *a priori* [27], making coherence start earlier. The use of pre-modulation ensures that the instability starts from a level which is larger than the typical noise level, and therefore it reduces the length it takes for the saturation of the FEL instabiities. This also ensures that the process is reproducible.

However, one can see that a very large energy spread leads to a spread in λ and therefore prevents the microbunching and coherent emission. The maximum allowed energy spread for the beam in an FEL comes from the Pierce parameter

$$\rho = \left[\frac{1}{16}\frac{I_0}{I_A}\frac{K_0^2[JJ]^2}{\gamma^3\sigma_\perp^2 k_u^2}\right]^{1/3}, \tag{1.7}$$

where I_0 is the beam current, $I_A = 17$ kA is the non-relativistic Alfvén current, $\sigma_\perp$ is the beam transverse size, $k_u = 2\pi/\lambda_u$, and $[JJ] = [J_0(\xi) - J_1(\xi)]$ with $\xi = K_0^2/(4 + 2K_0^2)$. To successfully laser, the energy spread of the electron beam $\sigma_E \ll \rho$. Typically, quadrupoles are added to make $\sigma_\perp$ as small as possible, so that ρ increases. At typical LWFA parameters [24], $\rho \approx 5 \times 10^{-3} = 0.5\%$. Electron beams from LWFA are often in the 0.5%-1% range, which leads to several compressions and decompressions so that the slice energy spread decreases and allows lasing.

As the electrons lase, the power grows exponentially as $P \propto P_0 \exp(z/L_g)$, where z is the space travelled by the beam and L_g is the gain length, given by

$$L_g = \frac{1}{2\sqrt{3}k_u\rho} \tag{1.8}$$

Table 1.1 calculates both the Pierce parameter ρ and gain length L_g for $K = 2$ and $\lambda_u = 2.5$ cm. Because the light always travels faster than the beam, there is a

γ	λ [nm]	ρ	Gain length Lg0 [m]	Energy spread [%]	eN [mm mrad]	$\sigma_\perp$ [mm]
100	3750	1,1E-01	1,0E-02	7,5E+00	1,2E+04	2,2E+04
500	150	2,2E-02	5,1E-02	1,5E+00	4,6E+02	1,9E+03
5000	1,50	2,2E-03	5,1E-01	1,5E-01	4,6E+00	6,1E+01
10000	0,38	1,1E-03	1,0E+00	7,5E-02	1,2E+00	2,2E+01
20000	0,09	5,6E-04	2,1E+00	3,7E-02	2,9E-01	7,6E+00
50000	0,02	2,2E-04	5,1E+00	1,5E-02	4,6E-02	1,9E+00

TABLE 1.1: FEL parameters at $\lambda_u = 2.5$ cm and $K = 2$.

slippage effect, where the microbunches are now dephased in relation to the emitted light.

1.3.5 COHERENCE AND SUPERRADIANCE

In 1954, R. H. Dicke coined the term 'superradiance' by saying: 'For want of a better term, a gas which is radiating strongly because of coherence will be called "superradiant" '[28]. That work explained how a quantum-mechanical system may amplify radiation as the photons emitted by atoms could cause photon emission in nearby atoms with the same phase and therefore amplify the radiation. The superradiant light intensity grows with N^2, where N is the number of light emitters. Coherence is a more common term that applies to any two waves with a constant relative phase and measures the possibility of interference between them. Temporal coherence measures the possibility of interfering a wave with a copy of itself delayed by a time τ. The delay τ_C where we observe that the correlation between the original wave and the delayed wave drops significantly is called the coherence time. The coherence time is strongly associated to the bandwidth of the pulse $\delta\omega$, such that $\tau_C \delta\omega \simeq 1$. This means that a pulse with a lot of frequency content will have a short coherency time.

For a light source to be superradiant, it requires all the light emitters must emit in phase, as that means that the emitted radiation constructively interferes for the intensity to scale with N^2. However, a coherent light emitter is not necessarily superradiant. A very simple example comes from an FEL. Let us imagine that an electron beam inside of an FEL is doubled in size and charge, such that the density is kept constant. In the typical FEL configuration, the intensity at a detector will not be changed. The energy is effectively doubled, as the pulse (with the same intensity) is now twice as long. However, if the electron beam density goes up by a factor of 2, the intensity is increased by a factor of 4. Even though it is commonly said that in a FEL the intensity goes up with N^2, it goes with $(N/n)^2$, where n is the number of microbunches that are formed. One can notice that N/n just means the number of

particles in each microbunch. Even though every particle in a FEL is coherent with each other, only the ones that are in the same microbunch are superradiant.

There has been work done on how to make an FEL radiate superradiantly, which requires the FEL to be operated at saturation [29, 30, 31, 32, 33]. In that case, as the light overtakes the electron beam (because it is faster), it increases its energy while keeping a self-similar shape. The scaling in that case is effectively I^2, where I is the electron current, which indicates superradiance.

1.4 Numerical Methods

1.4.1 PIC codes

Particle-in-cell codes are electromagnetic codes that have charged particles interact self-consistently with the electromagnetic fields that are defined on a grid. The PIC loop usually takes 4 steps: particles are advanced in time according to the relativistic Lorentz force, the currents are deposited on the grid, the fields are advanced at the grid positions by using the time-dependent Maxwell's equation, and fields are interpolated back to the positions of particles.

The space derivatives required for Maxwell's equations use finite-difference algorithms. To get a 2^{nd} order method in space and time, the grids of the several components of the electromagnetic fields may be spaced by a half step, corresponding to the Yee scheme[34].

Our simulations used Osiris [35, 36], a fully parallelized, fully relativistic particle-in-cell (PIC) code. Osiris discretizes spatial dimensions in a grid. Electric and magnetic fields are defined at each grid point and are advanced in time using a finite difference solver for the time-dependent Maxwell's equations. Macroparticles exist inside the grid and represent an ensemble of real particles. The macroparticle momentum and position advance in time is performed via the Lorentz force. All simulations are run self-consistently in three spatial dimensions.

1.4.2 Radiation Diagnostic

This work employs the Radiation Diagnostic for OSIRIS. Radiation coming from plasma setups is present in particle-in-cell codes. However, the typical radiation emitted by particles goes with γ^2. This often means that to resolve the typical (high-frequency) emitted radiation in the grid, one faces tremendous computational costs. Until recently, obtaining the radiation coming from PIC simulations required running the simulation and obtaining the trajectories of particles. One can calculate the emitted radiation by computing the Fourier transform of the Liénard-Wiechert potentials, both completely outside the temporally PIC loop [37] or as the simulation progresses [38].

The spatiotemporal profile of the emitted radiation is not retrievable from the spectra. To overcome the limitation and get the correct spatiotemporal structure of the emitted light, one can calculate the radiation emitted by every particle at every timestep using the Liénard-Wiechert potentials[39]:

$$\mathbf{E}(\mathbf{x}, t_{det}) = e\left[\frac{\mathbf{n}-\boldsymbol{\beta}}{\gamma_p^2(1-\boldsymbol{\beta}\cdot\mathbf{n})^3R^2}\right]_{\text{ret}} + \frac{e}{c}\left[\frac{\mathbf{n}\times[(\boldsymbol{n}-\boldsymbol{\beta})\times\dot{\boldsymbol{\beta}}]}{(1-\boldsymbol{\beta}\cdot\boldsymbol{n})^3R}\right]_{\text{ret}}, \tag{1.9}$$

where $\boldsymbol{n}$ is the direction of emission, $c\boldsymbol{\beta}$ is the velocity of the particle, R is the distance from the detector and the subscript ret refers to the retarded time. The first term of the equation is negligible in the far-field. If a particle emits a photon at each timestep, the time interval between the arrival of two photons emitted in consecutive timesteps is $dt_{rad} = dt/(2\gamma_p^2)$, with dt being the PIC timestep. This is quite interesting, as now we can capture frequencies $2\gamma_p^2$ times larger than the frequencies we can sample on the grid.

To simulate a detector, we consider a region of space where radiation is tracked, and we evaluate Eq.1.9 in all the cells of the detector. For each timestep and each particle, we loop through each spatial cell of the detector and check in what time cell the radiation arrives. Because we assume that the radiation travels at the speed of light, it is easy to calculate the time cell, meaning that the time resolution can increase without increasing the computational load. The computing time is proportional to the number of spatial cells multiplied by the number of time steps in the simulation multiplied by the number of particles.

This algorithm provides the spatiotemporal features of the light, not only the spectral content. It can get much higher time resolution than the grid and can capture coherent effects.

1.5 Contents

In Chapter 2 we develop the main theoretical treatment of radiation sources in plasma, where we introduce the concept of quasiparticles and explain how to create very bright light sources from nonlinear plasma wakefields and plasma density modulations, both broadband and narrowband. In Chapter 3, we show how we programmed spatiotemporal light pulses into particle-in-cell codes. In Chapter 4 we detail some possible applications of these spatiotemporal pulses, both using idealized and more realistic simulations. In chapter 5 we introduce a radiation light source, that couples realistic spatiotemporal pulses, plasma, and ultrarelativistic electron beams to induce temporally coherent betatron oscillations.

CHAPTER 2

COHERENT RADIATION FROM PLASMA QUASIPARTICLES

2.1 INTRODUCTION

As mentioned in section 1.2, compact plasma accelerators [8, 9] could miniaturize particle acceleration, with accelerations up to hundreds of GeV in a centimeter. By making particles in such setups radiate, they also function as a complementary, compact radiation source. Betatron sources coming from plasma acceleration provide intrinsically ultra-short, spatially collimated and bright x-rays [42] for for applications in biology [1], high energy density [44] and material [45] science, and nonlinear quantum electrodynamics [3]. These sources are on the order of a few cm, but the emission is temporally incoherent, leading to a linear growth of the radiation intensity with the number of particles.

Superradiant coherent light sources (where the radiation intensity grows with the squared number of particles), such as free electron lasers (FEL), provide extremely bright ($> 10^{28}$ photons/s/mm^2/mrad^2/0.1%BW) light pulses, and enable advanced technological applications in multiple fields, such as chemistry and physics. The brightness and size of these sources are typically correlated. The LCLS (Linac Coherent Light Source, in Stanford), one of the brightest light source in the world), provides x-rays with peak/average brightness of $10^{32}/10^{22}$ photons/s/mm^2/mrad^2/0.1%BW, being several km long. The cost of such facilities can be more than 1 billion (10^9) euros, which prevents a wider adoption worldwide (there is currently no FEL in Portugal). In such sources the radiation intensity scales with the number of light-emitting particles *squared*, which for a nC of charge (typical charge of an electron beam) would mean radiation intensities 10^9 larger compared with an incoherent source. The superradi-

ance that underlies these sources plays a key role in all the scientific and technological applications enabled by free electron lasers [41].

The figure of merit of radiation sources is the peak brightness, measured in photons per second per source area per solid angle per total bandwidth. Figure 2.1 shows the peak brightness for several plasma-based radiation sources. In this chapter, we show that we can get down to 50 nm of emission up to 10^{30} ph/s/mm^2/mrad^2/0.1%BW, which is much brighter than typical plasma sources.

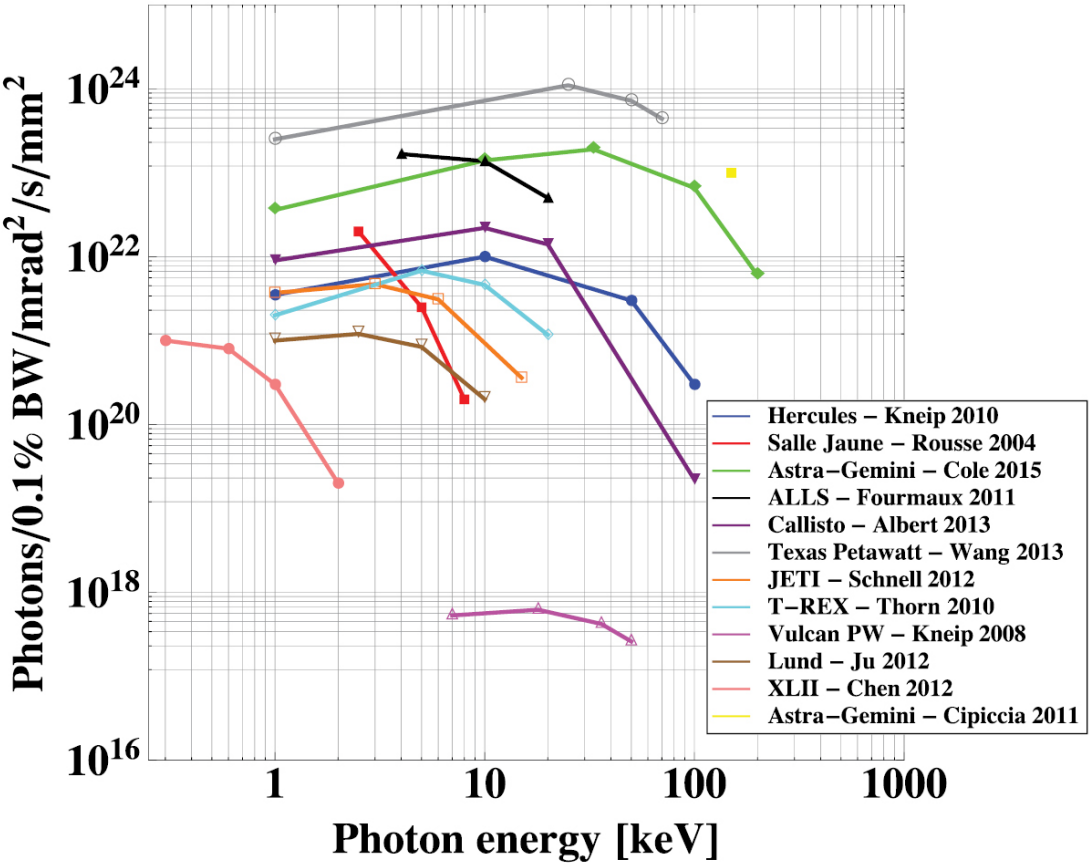

FIGURE 2.1: Peak brightness of betatron, Compton and bremsstrahlung radiation from LWFA compared to other types of sources in the same energy range. Sources included in this plot are: The APS synchrotron U30 undulator for harmonics 1, 3 and 5 (Argonne National Laboratory, USA), the ALS synchrotron (Lawrence Berkeley National Laboratory, USA), the Spring8 synchrotron (RIKEN, Japan), x-ray tubes (Copper and Molybdenum αK), the LCLS free electron laser (SLAC, USA), and high harmonics generation from laser-produced plasmas. Taken from [13].

To reach the brightness of FELs, plasma accelerator-based light sources need to become superradiant and temporally coherent. Such an advance could bring re-

search and technology that is only available in a handful of FELs worldwide directly to the many university, hospital, and industrial scale laboratories. Hence, the onset of temporal coherence and superradiance is an essential missing ingredient to create compact, affordable, and competitive plasma accelerator-based light sources.

Conventional free electron lasers are composed of an acceleration portion, about a couple kilometers, that accelerates electrons to several GeV. After they are accelerated, they undergo undulating motion in a separated undulator module, which is typically around 100 meters. In Fig. 2.2 we show the general layout of the European XFEL facility, in Hamburg, the brightest X-ray source in Europe.

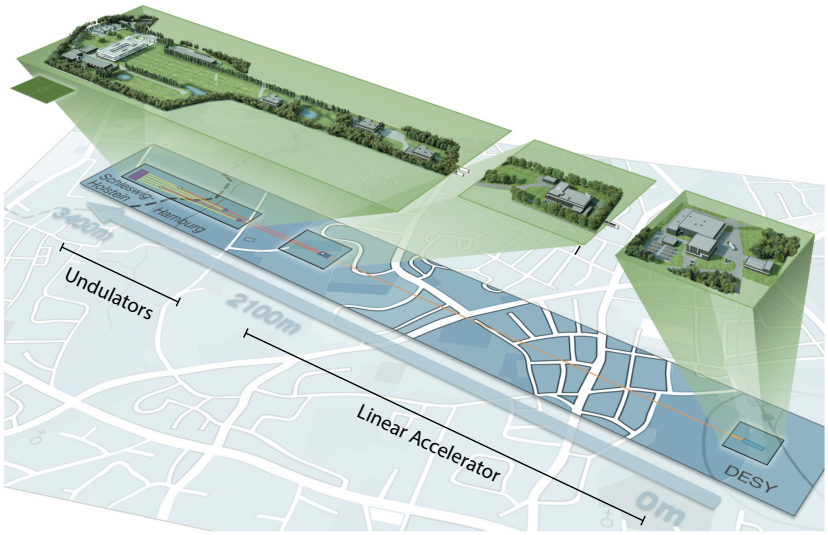

FIGURE 2.2: General layout of the European XFEL facility, with the DESY-Bahrenfeld site in Hamburg to the right and the research campus in Schenefeld with the experiment hall on the left. The overall length of the mostly underground facility is approximately 3.4 km, composed of 5.8 km of tunnels. Credits: XFEL https://www.xfel.eu/news_and_events/flyers_and_brochures/index_eng.html

Thanks to recent progress, plasma-based accelerators are now able to produce the high-quality standards [47], sub-percent energy spread required for FEL lasing [24, 25, 26]. Even though the acceleration portion of the FEL (a couple km) is reduced via the use of a plasma accelerator, the undulator portion (a couple hundred meters) is fixed. Therefore, there is demand for a superradiant process that relies solely on plasma to achieve this goal, allowing the miniaturization of the lasing portion of the FELs. Known methods consist, for example, of using plasma-based accelerators to create an ion-channel laser where bunches with an even higher quality oscillate [48], or bunches with specific spatiotemporal features (or generalized superradiance) [49]. This chapter, however, introduces a radiation concept that explores the coordinated motion of an ensemble of light-emitting particles, neglecting their singular trajectories

to focus on the whole group. The apparent trajectory of the ensemble determines key features of radiation, mimicking a single particle. The similarity between key radiation properties emmited by this group of particles, collectively, and of a finite-sized particleled led to denoting the former by quasiparticles. The definition of a quasiparticle in this work is a sharp current peak that is not necessarily constituted by the same group of particles, and where collective motion is independent from the constituent single particle motions.. As we will show, the onset of superradiance and temporal coherence by quasiparticles depends on a collective reorganization of a light-emitting medium, and not on the usual criteria for superradiant emission based on beam quality (which is a measure of uniformity of single particle trajectories).

The apparent trajectory of the quasiparticle controls the radiation features (such as broadband or narrowband). The range of possible velocities is expanded in comparison to single particles and the acceleration can be as high or as low as desired, even without the presence of strong electromagnetic fields. For example, as quasiparticles are in general a collective response to a perturbation in the light-emitting medium, they can travel at any velocity, even superluminal. This flexibility enables new mechanisms to obtain superradiance and temporal coherence effects.

Particles travelling faster than the phase velocity of light in a medium emit Cherenkov radiation, corresponding to broadband optical shocks travelling at an angle $\phi = \arccos(v/c_n)$, where v is the speed of the particle and c_n the phase velocity of the light in a medium [93]. Unlike never detected tachyonic particles, collective features moving superluminally exist, and were detected in previous plasma-based acceleration experiments [50, 51]. By optimizing such experiments, it is possible to create a quasiparticle that emits the equivalent superradiant coherent Cherenkov radiation, ideal for producing broadband radiation. Materializing in the laboratory such uncommon, but on-demand, broadband superradiant emission would enable medical and material processing applications not possible otherwise [52, 53]. By making a quasiparticle undergo an undulating motion we can produce temporally coherent, superradiant undulator radiation. This regime enables the production of narrow bandwidth emission, which is used by a myriad of applications, such as extreme ultraviolet nanolithography. There is also the possibility of combining both, creating a never-observed superluminal quasiparticle undulator, with an unprecedented radiation signatures, combining both Cherenkov and undulator features, depending on the angle. To get replicable results we focus on concepts that can operate in current plasma-based accelerator experiments and show comparable peak brightness to FELs operating in the extreme ultraviolet region.

This chapter is organized as follows: In Section 2.2.1, the concept of a quasiparticle is defined theoretically. In Section 4.3.1, both beam-driven and laser-driven quasiparticle Cherenkov effects are showcased, and the estimated brightness is calculated. In Section 2.6, the undulating quasiparticle concept is shown for several differ-

ent parameters.

2.2 QUASIPARTICLE RADIATION

2.2.1 THEORY

To properly study the quasiparticle radiation concept, it is important to know how a current density spike radiates from the Liénard-Wiechert potentials. The intensity radiated by a given current density $\mathbf{j}[\mathbf{r},t]$ per solid angle per unit frequency in the far-field [54] is:

$$\frac{d^2I}{d\omega d\Omega} = (\simeq)\frac{\omega^2}{4\pi^2c^3}\left|\int d\mathbf{r}\int dt\ \mathbf{n}\times[\mathbf{n}\times\mathbf{j}(\mathbf{r},t)]\ \exp\left[i\omega(t-\mathbf{n}\cdot\mathbf{r}/c)\right]\right|^2, \tag{2.1}$$

where t is the time of emission (retarded time), $\mathbf{r}$ is the position, ω is the radiation frequency, Ω the solid angle and $\mathbf{n}$ is a unit vector that sets the observation direction. The observation direction is given, in spherical coordinates, by

$$\mathbf{n} = [\cos(\theta), \sin(\theta)\sin(\varphi), \sin(\theta)\cos(\varphi)], \tag{2.2}$$

where θ is the angle with respect to the x-axis and φ is the angle with respect to the z-axis in the $y-z$ plane.

Equation (2.1) applies to arbitrary current density profiles, but to get insight into how collective effects affect radiation, we choose $\mathbf{j}(\mathbf{r},t) = \mathbf{j}[\mathbf{r}-\mathbf{r_c}(t)]$. This corresponds to a spatially localized current density profile that maintains a constant shape moving along the trajectory given by $\mathbf{r}_c(t)$. As we will show, this trajectory will set some key features of the radiation emitted by this current profile, as if it were a single finite-sized particle undergoing a trajectory given by $\mathbf{r_c}(t)$. Because of that property, we denote such a current density profile as a quasiparticle.

The most suitable coordinates to describe this system are $\boldsymbol{\xi} = \mathbf{r}-\mathbf{r_c}(t)$, $\tau = t$. In co-moving frame variables $(\boldsymbol{\xi},\tau)$, Eq. (2.1) can then be written as:

$$\begin{aligned}\frac{d^2I}{d\omega d\Omega} =&(\simeq)\frac{\omega^2}{4\pi^2c^3}\left|\int d\boldsymbol{\xi}\int d\tau\ \mathbf{n}\times[\mathbf{n}\times\mathbf{j}(\boldsymbol{\xi})]\ \exp\left[i\omega(\tau-\mathbf{n}\cdot(\boldsymbol{\xi}+\mathbf{r_c}(\tau))/c)\right]\right|^2\\ =&\frac{\omega^2}{4\pi^2c^3}\left|\int d\boldsymbol{\xi}\ \mathbf{n}\times[\mathbf{n}\times\mathbf{j}(\boldsymbol{\xi})]\exp[-i\omega\ \mathbf{n}\cdot\boldsymbol{\xi}/c]\right|^2\left|\int d\tau\ \exp\left[i\omega(\tau-\mathbf{n}\cdot\mathbf{r_c}(\tau)/c)\right]\right|^2,\end{aligned} \tag{2.3}$$

In the co-moving frame, the spatial ($\boldsymbol{\xi}$) and temporal (τ) integrals are independent of each other. In particular, it is important to note that the integration that contains the quasiparticle trajectory depends only on τ. The spatial integration over $\boldsymbol{\xi}$ is a multi-dimensional Fourier transform of the current density profile in the co-moving frame.

This integral will thus contain the spatial frequencies associated with the current profile. We therefore denote this integration as the quasiparticle shape factor $\boldsymbol{\mathcal{S}}(\omega,\Omega)$. With this definition, we recast Eq. (2.3) as:

$$\frac{d^2I}{d\omega d\Omega} = \frac{\omega^2}{4\pi^2c^3}\,|\boldsymbol{\mathcal{S}}(\omega,\Omega)|^2\left|\int d\tau\,\exp\left[i\omega(\tau-\mathbf{n}\cdot\mathbf{r_c}(\tau)/c)\right]\right|^2, \tag{2.4}$$

where we define the quasiparticle shape factor as

$$\boldsymbol{\mathcal{S}}(\omega,\Omega) = \int d\boldsymbol{\xi}\,\mathbf{n}\times[\mathbf{n}\times\mathbf{j}(\boldsymbol{\xi})]\exp[-i\omega\,\mathbf{n}\cdot\boldsymbol{\xi}/c] \tag{2.5}$$

2.2.2 Quasiparticle shape factor

The shape factor $\boldsymbol{\mathcal{S}}$ is a multi-dimensional Fourier transform over the spatial dimensions of the quasiparticle. As a result, we can further, re-cast $\boldsymbol{\mathcal{S}}$ as follows:

$$\boldsymbol{\mathcal{S}}(\omega,\Omega) = \mathbf{n}\times\left[\mathbf{n}\times\tilde{\mathbf{j}}(\mathbf{k}_{\tilde{\xi}})\right], \tag{2.6}$$

where $\tilde{\mathbf{j}}(\mathbf{k}_{\tilde{\xi}})$ is the Fourier transform of the current and $\mathbf{k}_{\tilde{\xi}} = \omega\mathbf{n}/c$ is the corresponding spatial frequency.

Equation (2.6) justifies our quasiparticle physical interpretation of the theory. To show this, we first notice that $\tilde{\mathbf{j}}$ can be generally separated into two functions, containing the low and the high spatial-frequency components of $\tilde{\mathbf{j}}$, and which we denote as $\tilde{\mathbf{j}}_0$ (describing the low-frequency regions of the spectrum) and $\tilde{\mathbf{j}}_1 \equiv \tilde{\mathbf{j}} - \tilde{\mathbf{j}}_0$ (carrying the high spatial frequencies). Here, high and low spatial frequencies are in comparison to the typical spatial frequency corresponding to the spatial features of the ensemble. The inverse Fourier transform of $\tilde{\mathbf{j}}_0$ is then a (smooth) function that envelopes the current profile. It provides a macroscopic description of the quasiparticle and therefore ignores its microscopic structure. In addition, $\tilde{\mathbf{j}}_0$ gives the low-frequency contents corresponding to the macroscopic structure of the quasiparticle, whose shape function, $\boldsymbol{\mathcal{S}}_0$, is given by $\boldsymbol{\mathcal{S}}_0(\omega,\Omega) = \left|\mathbf{n}\times\left[\mathbf{n}\times\tilde{\mathbf{j}}_0(\mathbf{k}_{\tilde{\xi}})\right]\right|$. It is this part that is independent of single particle motion.

The inverse Fourier transform of $\tilde{\mathbf{j}}_1$ contains information about the microscopic structure of the quasiparticle, which is due to the point-like nature of electrons. It is therefore a non-smooth function, which has spikes at the location of each quasiparticle electron. Hence, $\tilde{\mathbf{j}}_1$ gives the high-frequency components of the quasiparticle shape function $\boldsymbol{\mathcal{S}}_1$, which is given by $\boldsymbol{\mathcal{S}}_1(\omega,\Omega) = \left|\mathbf{n}\times\left[\mathbf{n}\times\tilde{\mathbf{j}}_1(\mathbf{k}_{\tilde{\xi}})\right]\right|$. Naturally, $\boldsymbol{\mathcal{S}} = \boldsymbol{\mathcal{S}}_0 + \boldsymbol{\mathcal{S}}_1$. In our formulation $\boldsymbol{\mathcal{S}}_0$ is responsible for the superradiant/coherent part of the radiation, while $\boldsymbol{\mathcal{S}}_1$ gives the incoherent part. We now focus our analysis on the radiation properties originating from $\boldsymbol{\mathcal{S}}_0$.

The suggestive form of Eq. (2.4) is analogous to that of a finite-sized single charged particle. To understand why, focus on the complex phase factor in Eq. (2.4),

which is exactly the same for a single charge and for a quasiparticle. An intriguing property then follows: within the bandwidth of $\boldsymbol{\mathcal{S}}(\omega, \Omega)$, a quasiparticle radiates as if it were a single finite-sized charged particle moving along $\mathbf{r}_c(\tau)$, regardless of the microscopic single electron quasiparticle dynamics.

It is then clear that the macroscopic quasiparticle shape, such as that captured by a particle-in-cell code, which usually ignores the point-like nature of electrons, and therefore disregards the internal quasiparticle microscopic structure, fully defines the quasiparticle shape function for wavelengths longer than the inter-particle distance. For these wavelengths, the radiation produced by the quasiparticle does not depend on the microscopic electron motion, but only on its shape and trajectory, as if it were a finite-sized particle executing the same trajectory. Interestingly, it is already possible to measure these structures in the laboratory, using femtosecond electron microscopy [55, 56].

We note that it is also possible to recover the single, point-like particle radiation spectrum from the current density description in Eq.(2.1). For point-like particles, the current density $\mathbf{j}$ is given by $\mathbf{j}(\mathbf{r}, t) = \sum_p c q_p \boldsymbol{\beta}_p \delta[\mathbf{r} - \mathbf{r}_\mathbf{p}(t)]$, where δ represents the Dirac delta function, the subscript p refers to the p-th particle, q_p the particle charge, $\mathbf{r}_\mathbf{p}$ the particle position and $\boldsymbol{\beta}_p$ the ratio of the particle speed to the speed of light. Plugging the current density into Eq. (2.1) simplifies the space integral, leading to:

$$\frac{d^2 I}{d\omega d\Omega} = \frac{\omega^2}{4\pi^2 c} \left| \sum_p q_p \int dt\, \mathbf{n} \times \left[\mathbf{n} \times \boldsymbol{\beta}_p\right] \exp[-i\omega(t - \mathbf{n} \cdot \mathbf{r}_\mathbf{p}(t)/c)] \right|^2 . \tag{2.7}$$

which recovers the well-known expression for the radiation spectrum emitted by a collection of point-like particles.

2.2.3 Benchmark simulations: single particle vs. collective radiation

To confirm this prediction of our theory, we conducted two-dimensional simulations describing the radiation from two electron bunches with different energies, 1 GeV and 10 GeV, but whose centroid undergo identical trajectories in the presence of an external magnetic field. The electron bunch size is bi-Gaussian with $(\sigma_x, \sigma_y) = (5.32\,\mu\text{m}, 5.32\,\mu\text{m})$, which corresponds to a FWHM size of 12.5 μm. The peak bunch density is $n_{b0} = 10^{16}$ cm^{-3}. We used longitudinal temperatures of 19 MeV and 61 MeV to randomize initial bunch particle positions for the 1 GeV and 10 GeV electron bunches at the start of the curved part of the trajectory, respectively. Bunch currents in both simulations are very similar, as bunch electrons travel at nearly the speed of light. An external magnetic field of magnitude 0.3 MG and 3 MG was used to curve electron bunches with 1 GeV and 10 GeV respectively, so the radius of curvature was kept the same. Bunches start moving from an unmagnetized spatial region to ensure a zero initial

force on bunch electrons at the start of the simulations. The radiation was collected in the far field using RaDiO [39], which retrieves radiation from simulation particle positions assuming they are point-like, and nowhere uses the current profile for calculations. Both electron bunches have a charge of 2 nC.

Figure 2.3 compare the radiation spectrum for both electron beams. Radiated intensity per frequency per solid angle is nearly the same in both cases for wavelengths longer than 12.5 μm. It is clear from the spectra shown in Fig. 2.3a-b that there is no difference between the radiation of two beams where one is 1 GeV and the second is 10 GeV. This is particularly clear in Fig. 2.3c, which shows the corresponding spectra at $\theta = 0.01$ rad. At shorter wavelengths, the 10 GeV bunch produces more radiation than the 1 GeV. Additional simulations with an electron beam with half the FWHM dimensions (6.25 μm) show that the radiation spectra are identical for wavelengths longer than 6.25 μm, shown in Fig. 2.3d.

Results in Fig. 2.3 are then in full agreement with our arguments above, in which we predicted that the low-frequency components (with wavelengths longer or of the order of the quasiparticle size) are independent of the microscopic nature and single electron trajectories with the quasiparticle.

2.3 QUASIPARTICLES IN PLASMA

We have established that a quasiparticle is a quasi-stationary localized current profile that travels along a certain trajectory. One simple example of a quasiparticle is a particle beam, in which the current profile of the whole beam travels with the beam speed, which served as benchmark for our theory in Section 2.2.3. In fact, coherent transition radiation is intimately connected with this concept, and we can look at Section 1.3.3 as a corollary of Eq.2.4. This quasiparticle trajectory is connected to the trajectory of the electrons inside the beam, and therefore is limited by the physical laws that apply to the electrons, such as the relativistic speed limit or the need for large fields to exert bigger accelerations. This happens with all quasiparticles that are always composed of the same constituent particles.

It is possible for a quasiparticle to have different constituent particles at different propagation times. In this case, the quasiparticle can be freed from the physical limitations that constrain the trajectory of single particles. For example, being a collective effect, quasiparticles may travel faster than light and have large accelerations without using fields. Because the constituent particles must be different at different times, they should not copropagate with the quasiparticle. In this work all quasiparticles come from transverse motion. At the same time, the shape of the quasiparticle should be as small as the wavelength we want to emit at, which leads to higher plasma densities, as the typical structures are of the order of c/ω_p.

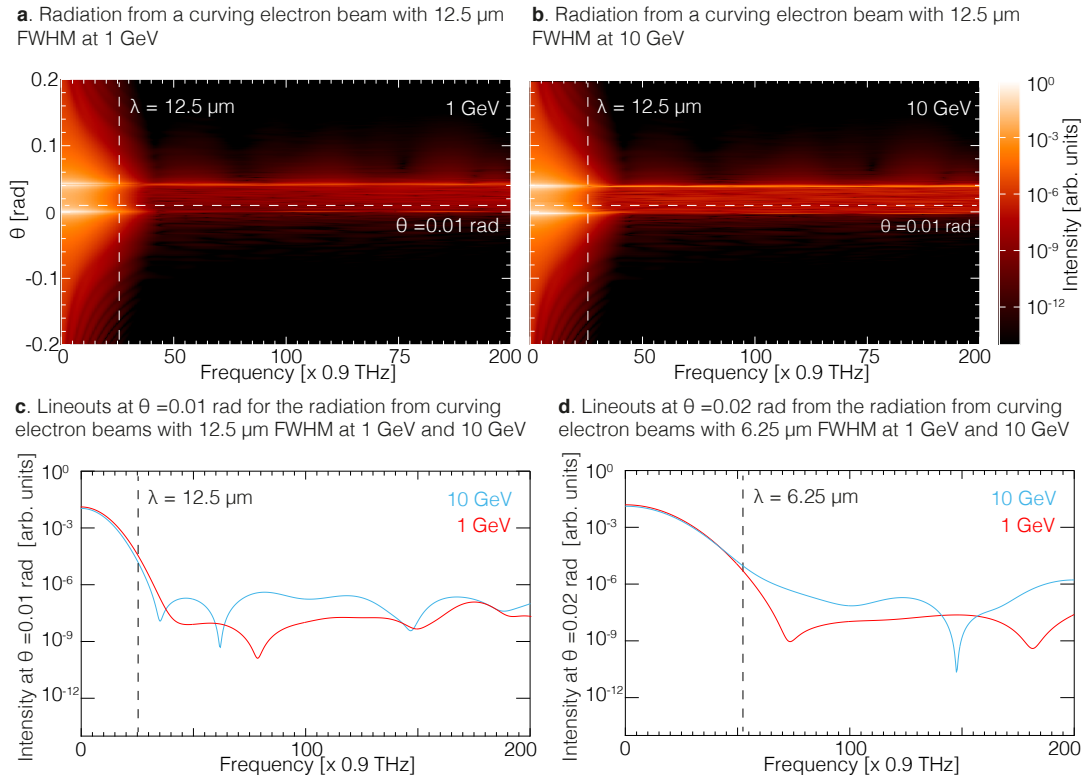

FIGURE 2.3: Radiated intensity per frequency per solid angle in two 2D simulations where the electron beam follows a circular trajectory given by an external magnetic field. a. Radiation from a beam where electrons have 1 GeV each. b. Radiation from a beam where electrons have 10 GeV each. Vertical dashed lines in a. and b. locate the frequency where the radiation wavelength equals the FWHM size of the electron beam (12.5 μm) c. Lineout of a. and b. at $\theta = 0.01$ rad. d. Equivalent lineouts at $\theta = 0.02$ rad for a simulation where the electron beam has half the size (6.25 μm).

One of the typical setups that generates quasiparticles are plasma-based accelerators, as the setup itself tends to generate very localized current profiles precisely due to the transverse motion of the background electrons. Figure 2.4 illustrates the shape function $\boldsymbol{\mathcal{S}}(\omega, \Omega)$ in the context of plasma-based accelerators. In Fig. 2.4a, an ultra-relativistic electron bunch radially expels the plasma electrons from its path. Most of the radially expelled electrons accumulate in a thin sheath which crosses the axis periodically, leading to a strongly nonlinear wakefield in the so-called blowout regime [57, 58]. When the sheath electrons cross the axis, they form sub-plasma-skin-depth density spikes that produce most of the radiation in the wakefield in the absence of trapping (see Fig. 2.4b). Such highly dense electron spike plays the role of a quasiparticle. Figure 2.4c then depicts the corresponding $\omega^2 \boldsymbol{\mathcal{S}}(\omega, \Omega)$. Here, the coherent part of the quasiparticle spectrum goes up to $\omega_{\max} \simeq 150\, \omega_p$.

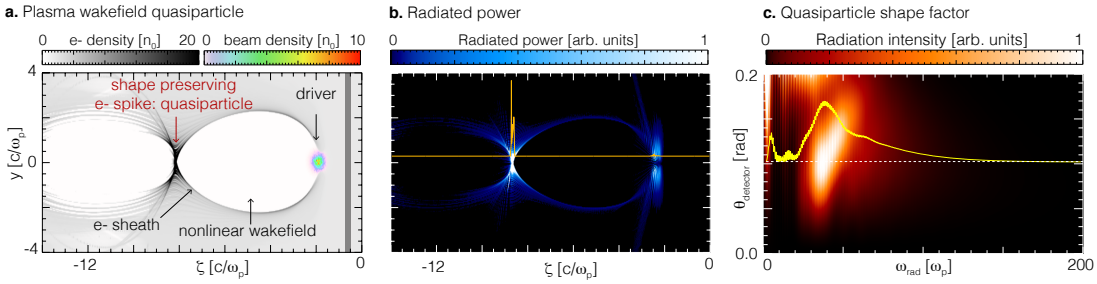

FIGURE 2.4: Nonlinear plasma wakefields and their radiation. a. Three-dimensional particle-in-cell simulation using Osiris where an electron beam drives a nonlinear plasma wakefield in the blowout regime. The plasma density is in gray, and the density of the electron bunch driver is in rainbow colors. In a frame that moves at the wake phase velocity, the electron spike at the back of the plasma oscillation is a nearly propagation-invariant structure. b. Radiated power from the nonlinear wakefield in a. A horizontal lineout is in orange. Colors are saturated to improve visualization. c. Shows the shape function $\omega^2|\mathbf{S}(\omega)|^2$ for the nonlinear wakefield, determined using the post-processing radiation algorithm RaDiO (see methods). This is equivalent to the radiation emitted by a thin electron slice in ξ as it crosses the electron bunch driver and returns to the axis. The radiation was recorded in a virtual detector placed in the far field. The yellow line shows a lineout of $\omega^2|\boldsymbol{\mathcal{S}}(\omega,\Omega)|^2$ at $\theta = 0.1$ rad.

2.4 BROADBAND RADIATION FROM THE QUASIPARTICLE CHERENKOV EFFECT

We are now in position of using the quasiparticle theory to explore quasiparticle radiation production. We are looking for very high radiation intensities and high frequency generation. One example of this is Cherenkov radiation.

We first recall that an electron moving faster than the speed of light in a medium generates optical shocks, commonly known as Cherenkov radiation. Cherenkov radiation constructively interferes at the Cherenkov angle, given by $\theta_C = \arccos(v/c_n)$. Here v is the electron velocity, and c_n is the speed of light in the medium. Because of relativity, Cherenkov radiation is forbidden in vacuum, as $v < c$.

Unlike single electrons, however, quasiparticles can travel faster than the speed of light in vacuum because they are a result of a collective effect. In order to describe the radiation from a superluminal quasiparticle, we then consider that the centroid trajectory $\mathbf{r}_c$ of the quasiparticle is given by $\mathbf{r_c}(\tau) = v_c\tau\ \mathbf{e_x}$. Substitution in Eq.(2.4)

yields:

$$\begin{aligned}\frac{d^2I}{d\omega d\Omega} &= \frac{\omega^2}{4\pi^2c^3}\left|\boldsymbol{\mathcal{S}}(\omega)\right|^2\left|\int_{T/2}^{T/2} d\tau \exp\left[i\omega(\tau-\mathbf{n}\cdot\mathbf{r_c}(\tau)/c\right]\right|^2 \\ &= \frac{\omega^2}{4\pi^2c^3}\left|\boldsymbol{\mathcal{S}}(\omega)\right|^2\left|\int_{T/2}^{T/2} d\tau \exp\left[i\omega\tau\left(1-\frac{v_c\cos(\theta)}{c}\right)\right]\right|^2 \\ &= \frac{\omega^2}{4\pi^2c^3}\left|\boldsymbol{\mathcal{S}}(\omega)\right|^2 T^2\mathrm{sinc}^2\left[\frac{\omega T}{2}\left(1-\frac{v_c\cos(\theta)}{c}\right)\right],\end{aligned} \tag{2.8}$$

Equation (2.8) shows that all frequencies in $\boldsymbol{\mathcal{S}}(\omega,\Omega)$ grow quadratically with propagation time (distance) at the Cherenkov angle defined as $\cos(\theta) = c/v_c$, provided that $v_c > c$. Because of the constant inflow of electrons in the collective motion, the intensity growth then also scales with the number of particles squared, which is a key feature of superradiance. Figure 2.5d (inset frame) shows this quadratic growth. However, the total radiation emission (accounting for all angles) grows linearly with time, indicating that the quadratic growth at an angle must be simultaneous with decoherent emission at other angles, as shown in Eq. (2.8). As the time of propagation increases, the range of angles for which one measures quadratic growth decreases.

The resonance function, and thus the radiated intensity, reach their maximum value when $\alpha = 0$, or equivalently when:

$$1-\frac{v_c\cos\theta}{c} = 0 \Leftrightarrow \cos\theta \equiv \cos\theta_c = \frac{c}{v_c}. \tag{2.9}$$

Equation (2.9) coincides with the well known Cherenkov radiation condition in vacuum for a point-like particle, but it now applies to quasiparticles. Even though their microscopic constituents (e.g., electrons) necessarily propagate with $v < c$, quasiparticles can travel at any speed. It is this peculiar property that enables quasiparticle Cherenkov emission, provided $v_c > c$, whereas point-like particles can never satisfy Eq. (2.9).

According to Eq. (2.9), superluminal quasiparticles generate an optical shock directed at the Cherenkov cone-angle θ_c. The optical shock forms because the phases of multiple light rays, emitted at different times (or, equivalently, by different particles), constructively interfere at θ_c. The radiated peak at the Cherenkov angle then exhibits a favourable scaling with T^2. In turn, T^2 scales with the square of the number of radiating particles, N^2. This is a key property of superradiance. To clarify why, note that T relates to the number of emitters as $N \propto n_0 v_c T \Leftrightarrow T \propto N/(n_0 v_c) \propto N$, with n_0 being the number density of light-emitting particles. Hence, the spectral density of the emitted radiation exhibits the typical superradiant scaling given by $\mathrm{d}^2I/(\mathrm{d}\omega\mathrm{d}\Omega) \propto T^2 \propto N^2$.

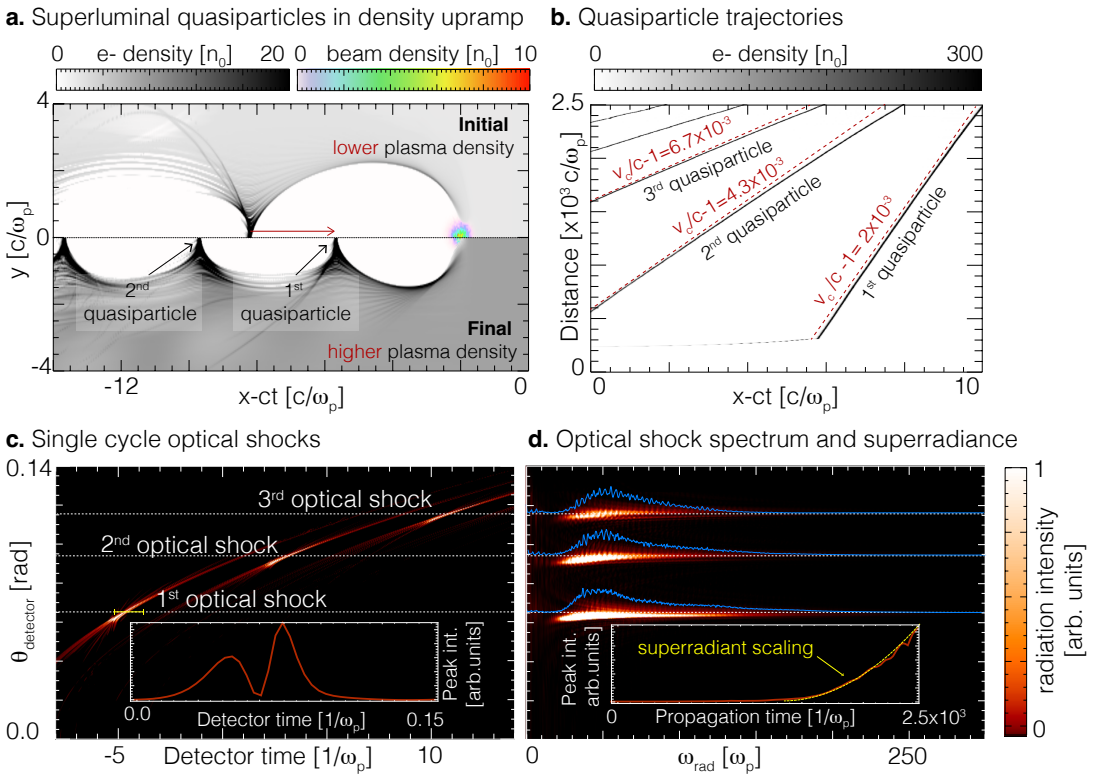

FIGURE 2.5: Onset of quasiparticle Cherenkov emission. a. Three-dimensional simulation result (see methods) showing plasma wakefields driven by an ultra-relativistic electron bunch in a plasma density upramp. Plasma electron density is in gray, and electron bunch density appears in rainbow colours. Top/bottom frames show the nonlinear wakefield structure earlier/later in the propagation. The quasiparticle trajectory is superluminal because the plasma wavelength decreases for higher plasma density. b. Waterfall plot showing the quasiparticle trajectories in a frame moving at c. The waterfall plot consists of on-axis lineouts of plasma electron density stacked as a function of propagation distance. c. Quasiparticle Cherenkov radiation optical shocks emitted by three electron spike quasiparticles in a virtual detector placed in the far-field. Colours show radiated intensity, determined numerically using a post-processing radiation tool (see methods). The inset is a zoom of the horizontal lineout shown in yellow, showing the the Cherenkov optical shock is a single cycle pulse. d. Corresponding spectral intensity. The inset demonstrates the favourable scaling (yellow) of the peak radiation intensity (red) with propagation distance.

2.4.1 PLASMA PROFILE

Superluminal electron spike quasiparticles can be created in the laboratory using plasma-based accelerator setups, where we can control the velocity via an appropriate plasma density profile. In Chapter 3 we will mention another way to generate these superluminal spikes, the *flying focus*, where the group speed of a laser focus can move at

arbitrary speeds.

Figure 2.5 illustrates the onset of superradiant quasiparticle Cherenkov emission in nonlinear wakefields driven by electron bunch drivers. Figures 2.5a-b demonstrate that a spatially varying plasma density profile can accurately control the trajectory (and velocity) of the dense electron spike at the back of the nonlinear plasma wave, which here play the role of the quasiparticle trajectory $\mathbf{r}_c(\tau)$ (and quasiparticle velocity v_c). This control is possible because the local plasma density sets the local plasma wavelength and, as a result, the distance from the driver to the first electron spike. Similar mechanisms, based on the so-called accordion effect.

To determine the electron spike trajectory as a function of the plasma density we based our derivation on Ref. [65]. Let us assume that the time-dependent longitudinal position of the electron spike $x_c(t)$ is given by the equation $x_c(t) = v_d t - \lambda_p[x_c(t)]$, where v_d is the speed of the driver, and $\lambda_p[x_c(t)]$ is the propagation-distance-dependent plasma wavelength. Taking the time derivative yields the following expression for the electron spike velocity $v_c t = \mathrm{d}x_c(t)/\mathrm{d}t$, given by:

$$v_c(t) = v_d - \frac{d\lambda_p[x_c(t)]}{dt} \approx v_d \left(1 - \frac{d\lambda_p(x)}{\mathrm{d}x}\right), \tag{2.10}$$

where we took $x_c \simeq x$ (x is the propagation distance), a valid approximation for a sufficiently smooth plasma density profile. According to Eq. (2.10), the first electron spike after the driver travels with a constant velocity $v_c = v_{c1}$ provided that:

$$\lambda_p(x) = \left(1 - \frac{v_{c1}}{v_d}\right) x + \lambda_{p0} \tag{2.11}$$

We recall that $\lambda_p \simeq 2\pi c/\omega_p$ (e.g. $\lambda_p = 106$ μm for an electron density of $n_e = 10^{17}\mathrm{cm}^{-3}$) and $n/n_0 = \omega_p^2/\omega_{p0}^2$, where $n_0 = n(x = 0)$ is the initial plasma density, and $\omega_{p0} = \omega_p(x = 0)$ is the corresponding electron plasma frequency. Substituting in Eq. (2.11) leads to the following expression for the propagation-distance-dependent plasma density profile along x:

$$n(x) = n_0 \frac{\lambda_{p0}^2}{[(1 - v_{c1}/v_d)x + \lambda_{p0}]^2} \simeq n_0 \left[1 + \frac{2(v_c/c - 1)}{\lambda_{p0}} x\right], \text{if } (1 - v_c/c)(x/\lambda_{p0}) \ll 1 \tag{2.12}$$

For a speed of $1.001c$ at a density of $n_0 = (10^{17} - 10^{18})$ cm^{-3} the initial ramp would be $(18.86 - 60.6)\%/\mathrm{cm}$. Equation (2.12) applies to the first electron spike. It is straightforward to calculate the speed of the n$^{\text{th}}$ electron spike, which is at a distance $n\lambda_p$ away from the driver.

$$v_{cn} - v_d = -n\frac{d\lambda_p(x)}{dt} = n(v_{c1} - v_d), \tag{2.13}$$

where v_{cn} is the speed of the n$^{\text{th}}$ electron spike. This implies that the Cherenkov-like cone angle of every spike is different (for $v_{c1} \neq v_d$) and therefore the radiation is angularly separated. This is seen in Fig. 2.5b, where $v_{cn} - c \approx nc(2 \times 10^{-3})$ [in the simulations $v_d \simeq c$] and in Fig. 2.5c, where we observe a clear temporal and angular separation of the shocks created by the multiple spikes/quasiparticles. In wakefield acceleration, the more superluminal the quasiparticle, the larger the longitudinal dimensions of the quasiparticle [67]. It is interesting to note that because of it the shape function of the n-th quasiparticle always contains more frequencies than the $(n+1)$-th quasiparticle. This is immediately clear from Fig. 2.5d, where we immediately observe a decrease in bandwidth as the emission angle increases.

It is relevant to state that subluminal speeds are also possible to obtain using the plasma density given by Eq. (2.12). However, electron self-injection can occur when $v_{cn} < c$. As the injected electrons accelerate to speeds close to c, we will have two radiation sources in the setup: the quasiparticle moving subluminally and the injected electron beam inside the ion bubble. Not only the radiation patterns created by these sources may be indistinguishable in a detector in the far-field, but the injected electrons also contribute to a growth in the bubble size, meaning it is harder to maintain a constant quasiparticle speed.

According to the discussion above, plasma density ramps can enable experimental demonstrations of coherent emission from quasiparticles in plasma accelerators. Plasma density ramps have long been experimentally demonstrated (e.g., in downramp injection in LWFA) by tilting the gas jet with respect to the propagation axis.

Figure 2.5c shows the far-field radiation intensity profile produced by superluminal quasiparticles. The spatiotemporal intensity profile indicates the presence of three optical shocks, which appear as bright radiation bursts that are both angularly and temporally separated. The optical shocks form at the Cherenkov angle set by the velocity of each quasiparticle, exactly as predicted by Eq. (2.9). The inset in Fig. 2.5c is a magnification of the temporal profile of the first optical shock, which clearly shows that it is a single-cycle optical pulse. The corresponding frequency spectra, shown in Fig. 2.5d, extend all the way up to $\omega \gtrsim 200\ \omega_p$. The inset of Fig. 2.5d, which shows the peak radiation intensity with propagation distance, illustrates the favourable quadratic scaling typical of superradiance. Hence, this mechanism can produce a train of superradiant, single-cycle, angularly and temporally isolated optical shocks.

2.4.2 LWFA SIMULATIONS

We can also produce a superradiant optical shock with laser pulses as drivers. Figure 2.6 shows that the superradiant quasiparticle Cherenkov effect can also be realized

in a LWFA. Figure 2.6a, which depicts the laser-driven wakefield structure, shows the characteristic electron spikes that play the role of quasiparticles. As a result, an optical shock appears at the Cherenkov angle in Fig. 2.6c, exactly where predicted. Because of the direct laser interaction with the plasma, we mix the quasiparticle effect with Thomson scattering, corresponding to radiation at laser harmonics. The radiated energy produced by the quasiparticle in Fig. 2.6 is three times higher than the energy radiated into the third harmonic of the laser frequency, demonstrating that the process produces clear, experimentally detectable signatures. To have a better physica understanding of the process, we plotted the 3D version of Fig. 2.6a in Fig. 2.18 (at the end of this chapter).

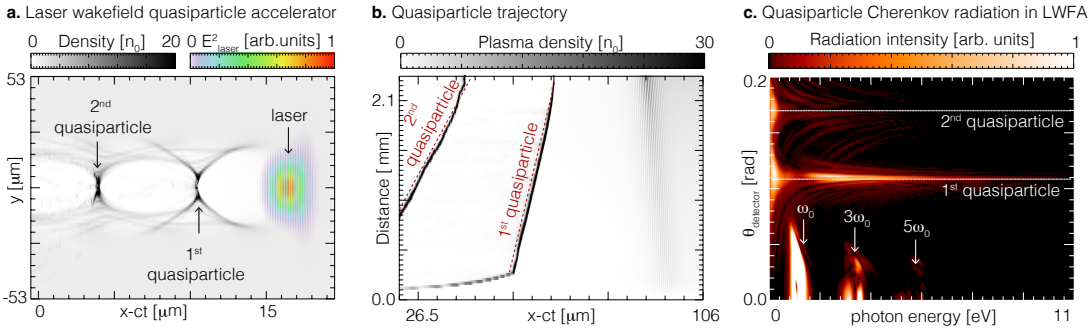

FIGURE 2.6: Quasiparticle Cherenkov radiation in a laser wakefield accelerator. a. Laser driven plasma wakefields. Plasma density appears in gray, and the square of the laser electric field in rainbow colours. b. Waterfall plot showing the quasiparticle trajectories in a frame moving at c. The waterfall plot consists of on-axis lineouts of plasma electron density stacked as a function of propagation distance. c. Corresponding spectral intensity in a virtual detector in the far field. The white dashed lines are placed at the Cherenkov angles corresponding to the velocity of the first and second quasiparticles. The fundamental laser frequency, and its harmonics are also visible.

2.5 Optimizing brightness from PWFA simulations

2.5.1 Current density shape

To further understand the structure of $\mathcal{S}(\omega, \Omega)$, we conducted additional full 3D and cylindrically symmetric simulations in order to relate the nonlinear wakefield blowout radius with the typical thickness of the electron spike at the bubble back, which gives a figure for the (macroscopic) quasiparticle spectral bandwidth.

Figure 2.7 summarises the results. It shows that as the blowout radius increases, the longitudinal size of the rear of the wakefield decreases. Simulations show electron spike thicknesses that can be lower than 1% of the plasma skin depth, down

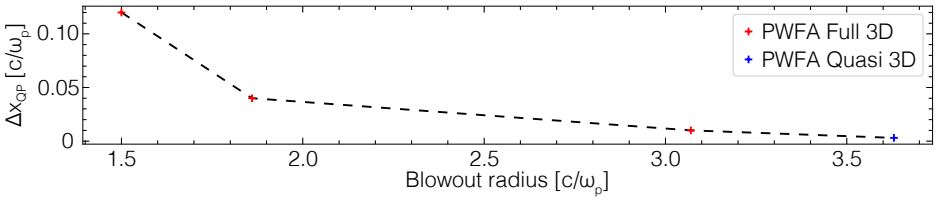

FIGURE 2.7: Longitudinal size (FWHM) of the current density profile at the rear of the wakefield as a function of the blowout radius.

to 0.003 c/ω_p for large enough blowout radii. This means that the macroscopic quasiparticle structure can emit coherently at similarly small wavelengths. For plasma densities of $n_0 = 10^{18}$ cm^{-3} this gives 16 nm or 77 eV. These simulations were first conducted with a cold plasma background, but we also investigated the role of plasma temperature and collisions. Simulations showed that plasma temperature and collisions increase the thickness of the spike by a few tens of percent. For the simulation with the smallest electron spike thickness (0.003 c/ω_p), both a background electron temperature and collisions increased the thickness by a factor of 1.5, which would give us about 25 nm or 49 eV.

By using cylindrically symmetric simulations, we performed high resolution simulations with increasingly higher blowout radii. Since the thickness of the electron spike at the rear of the wakefield decreases as the blowout radius increases (cf. Fig. 2.7), these simulations would not have been possible in 3D as the computational requirements were too high. This subsection then shows simulation results of a cylindrically symmetric PIC simulation using a SLAC-like electron bunch, predicting high peak brightness at photon energies close to 40 eV. The simulation was conducted in Osiris.

To simulate an electron beam in quasi-3D, we considered a Gaussian profile given by

$$n(x,y,z) = n_{b0} \exp\left(-\frac{z^2}{2\sigma_z}\right) \exp\left(-\frac{x^2}{2\sigma_x}\right) \exp\left(-\frac{y^2}{2\sigma_y}\right), \tag{2.14}$$

where n_{b0} is the peak electron beam density, z is the longitudinal direction, x and y are the transverse directions and σ_a relates to the size across the a direction. To determine the total charge Q one must integrate over the three dimensions, yielding

$$Q[\text{nC}] = n_{b0}[\text{cm}^{-3}]\sigma_x[\mu\text{m}]\sigma_y[\mu\text{m}]\sigma_z[\mu\text{m}]\frac{2\sqrt{2}\pi^{3/2}}{6.24\times10^{21}} \tag{2.15}$$

We considered an over-dense beam with peak density $n_{b0} = 24n_0$ propagating in the x direction with relativistic factor $\gamma = 19569.5$, with corresponding energy $E \simeq 10$GeV. The momentum spread in the x, y, and z directions is $(\Delta p_x, \Delta p_y, \Delta p_z) =$

$(195.6, 18.6143, 18.6143)\ m_e c$. The driver density profile is Gaussian, with dimensions $(\sigma_x, \sigma_r) = (0.38, 0.94) c/\omega_p$. These parameters correspond to an electron plasma density $n_0 = 1.0 \times 10^{18}$ cm^{-3} for a beam with 3 nC. The corresponding electron bunch dimensions along x is 2 μm and along r is 5 μm. The numerical PIC grid contains 16000×2000 cells, with 3×3 electrons per cell and a total simulation volume of $(\Delta x \times \Delta r) = 14 \times 14\ (c/\omega_p)^2$. The electron background temperature is 10 eV. The plasma profile was given by Eq. (2.12) with $v_{c1} = 1.002c$ and $\lambda_{p0} = 6\ c/\omega_p$.

We modelled 2.5 mm of propagation after the bubble was fully formed. Due to nonlinearities, the rear of the wakefield does not move at a fixed speed. Thus, to retrieve the brightness, we fitted the quasiparticle trajectory by a second order polynomial function of the propagation distance, shown in Fig. 2.8a (blue). The full width half maximum (FWHM) of the dense electron spike thickness (quasiparticle) formed at the back of the nonlinear wakefield, close to the axis, is 25 nm. This would correspond to coherent photon emission at around 50 eV.

We determined $\boldsymbol{\mathcal{S}}(\omega, \theta)$ using the current density at a given propagation distance, and performed a numerical integration of the radiation energy by using the second order polynomial fit to the quasiparticle trajectory. By following this procedure, we estimated the brightness evolution as a function of propagation distance. The peak brightness after 2.5 mm is 10^{28}ph/s/cm^2/mrad^2/0.1%BW at a photon energy of 40 eV and at an angle $\theta = 0.075$ rad.

Similarly shaped dense electron spikes could also be produced in the LWFA, at a normalized laser vector potential $a_0 = 6$, $\lambda = 800$ nm, electron density of $n_0 = 1.95 \times 10^{18}$, duration of 70 fs and spotsize of $W_0 = 18$ μm. However, quasiparticle velocity variations were greater and therefore led to smaller brightnesses in the accumulated propagation distance. In principle, the quasiparticle velocity becomes more stable at lower densities (where computational requirements are higher than at higher plasma density), where the laser evolution is less evident.

2.5.2 Non-idealities

Quasiparticle Acceleration

Equation (2.8) assumes constant v_c. As stated above, when $v_c > c$, this ensures that the radiation intensity grows quadratically with propagation distance (time) for all frequencies at the Cherenkov angle. In practice, and for example as result of the self-consistent propagation of an electron beam or laser pulse driver in the plasma, v_c can fluctuate. It is therefore important to quantify the influence of these fluctuations on the superradiant scaling.

We assume that the quasiparticle velocity is $v_c = v_{c0} + \Delta v$, where $\Delta v \ll v_c$ is a perturbation to the average centroid velocity. These velocity variations can change

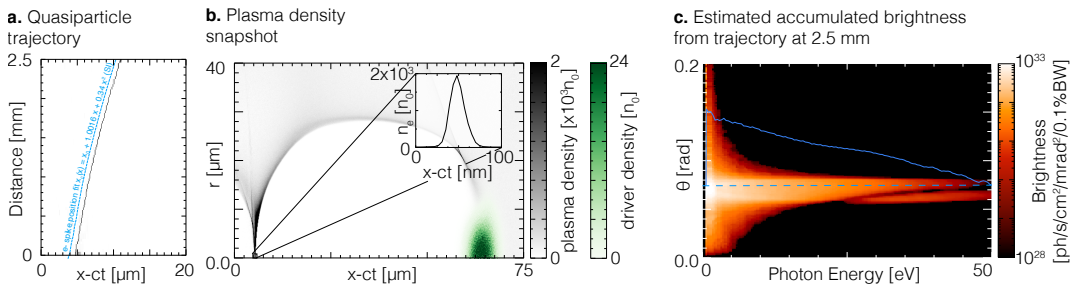

FIGURE 2.8: Simulation data from a SLAC-like beam propagating in a plasma at $n_0 = 10^{18}\text{cm}^{-3}$. a. Waterfall plot showing the quasiparticle trajectory in a frame moving at c as a function of the propagation distance. Quadratic fit of the quasiparticle trajectory in blue. b. Plasma density (in gray) and driver density (in green) at a propagation distance of 0.3 mm. Inset plot shows the thickness of the dense electron spike at rear of the wakefield on-axis (i.e. $r = 0^-$m). c. Estimated accumulated brightness after 2.5 mm of propagation, as a function of photon energy and emission angle. Lineout taken at $\theta = 0.075$ rad shown in blue (maximum and minimum of the scale are the same as the plot).

the Cherenkov emission angle. If they are sufficiently large, velocity fluctuations can stop the quadratic superradiant scaling above a certain propagation distance and frequency. This occurs when the sinc function in Eq. (2.8) changes from 1 to 0 as a result of the velocity fluctuations, or equivalently, when the argument of the sinc changes from 0 to π or $-\pi$ at a given angle. Constructive interference above a certain frequency ω then stops after a propagation time T_m, given by:

$$T_m \sim \frac{2\pi c}{\omega|\Delta v|}, \tag{2.16}$$

where we assumed that the Cherenkov emission angle is $\theta \ll 1$. The condition obtained in Eq. (2.16) shows that a certain variation Δv of the quasiparticle velocity limits the maximum period of time (propagation distance) under which constructive interference occurs. It also shows that this time (distance) decreases for higher frequencies.

According to Eq. (2.8), the typical angular width of the Cherenkov radiation cone, $\theta_{\max} = |\theta_+ - \theta_-|$, decreases with propagation distance. Here θ_+ and θ_- are the angles for which the sinc function in Eq. (2.8) is 1 and -1, respectively. Constructive interference stops when the variation of the Cherenkov angle, due to Δv, is greater than this typical angular thickness $\theta_{\max}$.

Figure 2.9 uses this criterium to complement the calculation above with a more precise estimate of the maximum propagation distance for which there is constructive interference, applied to the PWFA and LWFA simulation results. To produce the plots in Fig. 2.9, we first fitted a polynomial function to the simulation data to determine the quasiparticle propagation velocity as a function of propagation distance. We set v_{c0} as the electron spike velocity corresponding to the prediction given by Eq. (2.10).

In addition, $\Delta v(x) = v_c(x) - v_{c0}$, where $v_c(x)$ is the propagation dependent velocity of the electron spike at the back of the nonlinear wakefield. We determine θ_+ and θ_- by setting the argument of the sinc function to π and $-\pi$. Figure 2.9 compares $\Delta\theta(x)$ with $\theta_{\max} = |\theta_+ - \theta_-|$. Superradiant growth stops when $\Delta\theta \gtrsim \theta_{\max}$.

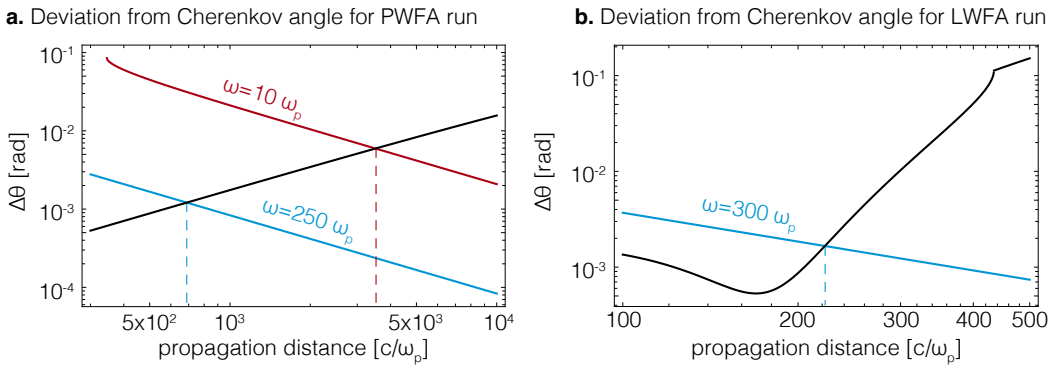

FIGURE 2.9: Deviation $\Delta\theta$ from Cherenkov angle (black) determined by fitting the position of the dense electron spike at the back of the nonlinear wakefield to a polynomial function of the propagation distance. The maximum allowed deviation $\theta_{\max}$ are in light-blue and/or in red. Superradiance stops at the locations defined by the dashed lines. Note that the x axis does not start at $x = 0$. a. Shows $\theta_{\max}$ for two radiation frequencies $\omega = 10\omega_p$ (in red) and $\omega = 250\omega_p$ (in blue) as a function of propagation distance for the PWFA run shown in Fig. 2.5. The fit is a second order degree polynomial function of the propagation distance. b. Maximum allowed deviation θ_{max} for frequencies of $300\omega_p$ (in blue) as a function of propagation distance. The fit is a forth order degree polynomial function of the propagation distance.

Figure 2.9a shows that, in the PWFA run, the superradiant scaling holds up to a propagation distances $\lesssim 700c/\omega_p$ at $\omega = 250\ \omega_p$, whereas quadratic growth can be sustained up to $\lesssim 3500\ c/\omega_p$ for $\omega = 10\omega_p$. Due to the driver evolution, the electron spike velocity is less stable in the LWFA run than in the PWFA. Figure 2.9b then shows that the intensity at $\omega = 300\ \omega_p$ can grow quadratically up to $\lesssim 220\ c/\omega_p$. For a plasma density $n_0 = 10^{18}$ cm^{-3}, this corresponds to photon energies of roughly 12 eV.

To visualize the impact of a changing quasiparticle velocity, we calculated the time integral seen in Eq. (2.4) for both an ideal trajectory and the fitted trajectory in Fig. 2.8. Figure 2.10 shows these results. When the quasiparticle velocity is constant, the radiation energy is fully located around the Cherenkov angle, particularly at higher photon energies. Quasiparticle velocity variations lead to an angular radiation emission spread, over the angular range that goes from $\theta \simeq 0.063$ rad to $\theta \simeq 0.076$ rad. The radiation energy has a noticeable decrease at higher photon energies, as particles stop radiating coherently, as previously discussed in Eq. (2.16).

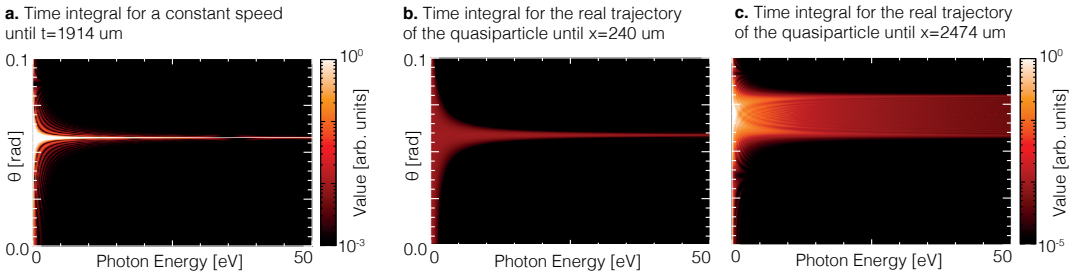

FIGURE 2.10: Influence of a variable quasiparticle velocity in the time integral in Eq. 2.4 a. Time integral for a constant speed of $v = 1.001684c$ until a propagation distance of $x = 1914$ μm. b-c. Time integral considering a propagation distance dependent quasiparticle velocity, retrieved from simulations, until $x = 240 - 2474$ μm of propagation. The scales are the same in all three plots. Note that θ only varies between $0 - 0.1$ rad, unlike in the previous Fig. 2.8, where θ varies in the range $0 - 0.2$ rad.

2.5.3 GRID RESOLVED RADIATION

Even though RaDiO lets us look at frequencies larger than those allowed by the grid size, the Cherenkov-like emission is broadband and therefore the PIC code is able to capture part of the emitted beam. To observe the emission of Cherenkov radiation in the PIC simulation directly, we conducted two simulations, one with the specific linear profile given by the approximation of Eq.2.12 and another with a constant profile. We then multiplied the electric field by the distance to the axis (as these are axisymmetric simulations) and compared both cases, shown in Fig.2.11. While in the upramp case we immediately find the electromagnetic shock, in the constant profile the radiation is mostly produced by the self-injected electron beam.

2.5.4 RADIATION DIAGNOSTICS

The radiated power in Fig. 2.4b was obtained using the relativistic Larmor formula, given by [54]:

$$P \propto \gamma^6 \left[\dot{\boldsymbol{\beta}}^2 - (\boldsymbol{\beta} \times \dot{\boldsymbol{\beta}})\right], \tag{2.17}$$

where macroparticle position and speed are taken from simulations, and the corresponding PIC simulation particle acceleration is calculated using the **E** and **B** fields at the particle position.

All other remaining radiation calculations are done at PIC simulation run time using the Radiation Diagnostic for Osiris (RaDiO) [39]. The calculations use the position, velocity, and acceleration of each PIC macroparticle, which is known at each time step. RaDiO determines the spatio-temporal profile of radiated electric fields by accumulating these fields in each temporal and angular cell, allowing for the evaluation of

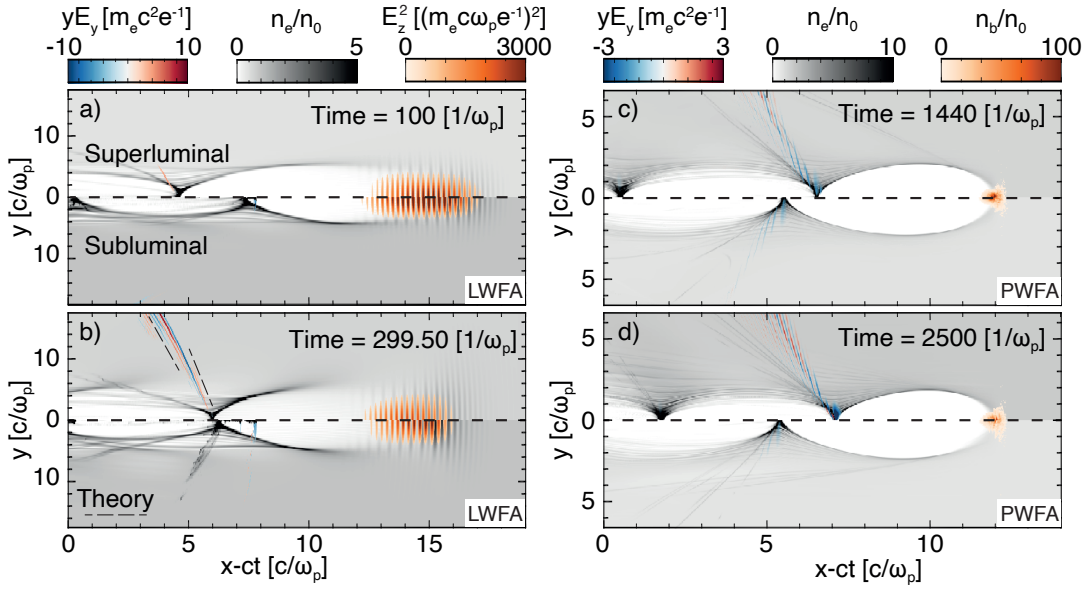

FIGURE 2.11: Onset of Cherenkov-like optical shock in 3D PIC simulations using linear up-ramps. Upper (lower) half of each panel correspond to superluminal (subluminal) velocity of the electron spike at the bubble back. Left (right) collumn panels refer to laser pulse (particle beam) driven cases. The laser and particle driver appear in red, Plasma electron density in gray, and radiated electric field in blue-red. The radiated electric field is multiplied by the distance to the axis in order to compensate for radiation diffraction.

temporal and spatial coherence effects using the following expression [54]:

$$\mathbf{E}_{\text{rad}} = \frac{e}{c}\left[\frac{\mathbf{n}\times(\mathbf{n}-\boldsymbol{\beta})\times\dot{\boldsymbol{\beta}}}{(1-\boldsymbol{\beta}\cdot\mathbf{n})^3 R}\right]_{\text{ret}}, \tag{2.18}$$

where R is the distance to the detector, the subscript ret means that all quantities are determined at the retarded time t_{ret}, and where the detector time, t_{det}, is $t_{\text{det}} = t_{\text{ret}} + |R|/c$. In addition, $\boldsymbol{\beta}$ is the particle velocity normalized to c, $\dot{\boldsymbol{\beta}}$ its corresponding time derivative. All radiation detectors used in these simulations are spherical. For the case of the laser driver simulations, the detector temporal cell size is $\Delta t = 0.0049c/\omega_p$ and the angular cell size is $\Delta\phi = 1.1$ mrad. The detector contains 256×6144 cells in the ϕ and temporal dimensions, respectively. For the case of the electron bunch driver, the temporal cell size is $\Delta t = 0.0036c/\omega_p$ and the spatial cell size is $\Delta\phi = 0.073$ mrad. The detector contains 2048×6144 cells in the ϕ and temporal dimensions, respectively.

For both cases, $\Delta\theta$ is not defined as fields are calculated only for a slice at $\theta = \pi/2$ (radiation emitted to the front of the driver at $y = 0$).

2.6 NARROWBAND EMISSION FROM QUASIPARTICLE UNDULATOR RADIATION

Quasiparticle Cherenkov emission leads to superradiance over the entire quasiparticle (broad) bandwidth. The quasiparticle concept can also be used to generate narrow bandwidth, temporally coherent radiation. To investigate this radiation in a configuration directly accessible to experiments, we consider a longitudinally undulating quasiparticle trajectory. The longitudinal quasiparticle undulator exploits the so-called accordion effect, which could be experimentally realized with ionization induced plasma density gratings [68] and corrugated plasma channels [69, 70], combined with a density ramp to adjust the mean quasiparticle velocity.

In contrast with quasiparticle Cherenkov radiation, which is intrinsically broadband, undulator radiation is useful to produce coherent light with narrow linewidths. The undulation amplitude can be controlled in a nonlinear wakefield by adjusting the a parameter in Eq. (2.22). The average longitudinal plasma density profile controls the average quasiparticle velocity.

To determine the corresponding radiation spectrum, we assume that the quasiparticle trajectory is given by $\mathbf{r}_c(\tau) = v_c\tau + \Delta x_c \sin(\omega_c\tau)\ \mathbf{e_x}$, where v_c is the average quasiparticle velocity, Δx_c is the amplitude of the oscillation, and ω_c is the oscillation frequency. This expression accurately captures simulation result. Substituting $\mathbf{r}_c$ in Eq. (2.4) yields:

$$\begin{aligned}
\frac{d^2I}{d\omega d\Omega} &= \frac{\omega^2}{4\pi^2c^3}\left|\boldsymbol{\mathcal{S}}(\omega,\Omega)\right|^2\left|\int_{T/2}^{T/2} d\tau \exp\left[i\omega(\tau - \mathbf{n}\cdot\mathbf{r_c}(\tau)/c\right]\right|^2 \times \\
&= \frac{\omega^2}{4\pi^2c^3}\left|\boldsymbol{\mathcal{S}}(\omega,\Omega)\right|^2 \times \\
&\quad \times \left|\int_{T/2}^{T/2} d\tau \exp\left[i\omega\left(\tau - \frac{v_c\cos(\theta)\tau}{c} - \frac{\Delta x_c\ \sin(\omega_b\tau)\cos\theta}{c}\right)\right]\right|^2 \\
&= \frac{\omega^2}{4\pi^2c^3}\left|\boldsymbol{\mathcal{S}}(\omega,\Omega)\right|^2 \times \\
&\quad \times \left|\int_{T/2}^{T/2} d\tau \exp\left[i\omega\left(\tau - \frac{v_c\cos(\theta)\tau}{c}\right)\right]\exp\left[\frac{i\omega\ \Delta x_c\ \cos\theta}{c}\sin(-\omega_b\tau)\right]\right|^2
\end{aligned}$$

We can simplify the expression above using the Jacobi-Anger expansion:

$$\exp(ib\sin\sigma) = \sum_{-\infty}^{\infty} J_n(b)\exp(in\sigma), \tag{2.19}$$

which then leads to:

$$\begin{aligned}
\frac{d^2I}{d\omega d\Omega} &= \frac{\omega^2}{4\pi^2c^3}\left|\boldsymbol{\mathcal{S}}(\omega)\right|^2 \times \\
&\times \left|\int_{T/2}^{T/2} d\tau \exp\left[i\omega\left(\tau - \frac{v_c\cos(\theta)\tau}{c}\right)\right]\sum_{m=-\infty}^{\infty} J_m\left(\frac{\Delta x_c\,\omega\cos\theta}{c}\right)\exp(-im\omega_b\tau)\right|^2 \\
&= \frac{\omega^2}{4\pi^2c^3}\left|\boldsymbol{\mathcal{S}}(\omega)\right|^2 \times \\
&\times \left|\sum_{m=-\infty}^{\infty} J_m\left(\frac{\Delta x_c\,\omega\cos\theta}{c}\right)\int_{T/2}^{T/2} d\tau \exp\left[i\omega\left(\tau - \frac{v_c\cos(\theta)\tau}{c} - \frac{m\tau\omega_b}{\omega}\right)\right]\right|^2 \\
&= \frac{\omega^2}{4\pi^2c^3}T^2\left|\boldsymbol{\mathcal{S}}(\omega)\right|^2 \times \\
&\times \left|\sum_{m=-\infty}^{\infty} J_m\left(\frac{\Delta x_c\,\omega\cos\theta}{c}\right)\mathrm{sinc}\left\{\frac{T}{2}\left[\omega\left(1 - \frac{v_c\cos\theta}{c}\right) - m\omega_c\right]\right\}\right|^2,
\end{aligned} \tag{2.20}$$

Equation (2.20) shows that the radiation intensity is maximum when the argument of the sinc function vanishes. This condition is fulfilled at the resonant harmonic frequencies, which are given by:

$$\omega_m(\theta) = \frac{m\omega_c}{1 - \frac{v_c\cos\theta}{c}}. \tag{2.21}$$

Equation (2.21) recovers the well-known expression for the resonant harmonic frequencies of standard undulator radiation. Close to the axis, where $\cos\theta \approx 1$, resonant frequencies correspond to the double Doppler shifted quasiparticle oscillation frequency, being given by $\omega_m \simeq m2\gamma^2\omega_c$, where $\gamma = 1/|\sqrt{1-\beta^2}|$, and where $\beta = v_c/c$ is the average quasiparticle velocity normalized to c. Note that this result holds for both subluminal and superluminal quasiparticles. When $v_c > 2c$, the resonant frequencies are lower than the oscillation frequency ω_c. This is a manifestation of an inverse Doppler effect, which has never been observed under these conditions. We note that, just as if it were a point-like particle, the radiation intensity grows quadratically with propagation distance at the resonant harmonics defined by Eq. (2.21), as shown in Fig 2.15c (inset plot). The narrowband spectrum contrasts with the broadband emission from quasiparticle Cherenkov radiation.

2.6.1 Plasma Density Profile for Undulating Quasiparticles

Equations (2.20-2.21) generalize undulator radiation to quasiparticles traveling with an arbitrary velocity. Except for the shape factor $\boldsymbol{\mathcal{S}}(\omega,\Omega)$, Eqs. (2.20-2.21) coincide

exactly with the spectral intensity emitted by a point-like particle propagating along the quasiparticle trajectory $\mathbf{r}_c(\tau) = [v_c\tau + \Delta x_c \sin(\omega_c\tau)]\mathbf{e}_x$.

It is possible to wiggle the quasiparticle by manipulating the plasma density, with a very similar approach to the one of the superluminal quasiparticle. Including a longitudinal sinusoidal modulation in Eq. (2.12), such that,

$$n(x) = n_0[1 + \alpha \sin(\omega_c x)]\frac{\lambda_{p0}^2}{[(1 - v_{c1}/v_d)x + \lambda_{p0}]^2}, \tag{2.22}$$

creates a longitudinally undulating quasiparticle. Starting from the density profile $n(x)$, one is able to get the speed of the quasiparticle along the propagation

$$\begin{aligned} v_c(x) &= v_d\left(1 - \frac{\mathrm{d}\lambda_{p0}(x)}{\mathrm{d}x}\right) \\ &= v_d - (v_d - v_{c1})(1 + \alpha\sin(\omega_c x)) + \frac{1}{2}[(v_d - v_{c1})x + \lambda_{p0}v_d]\frac{\omega_c\alpha\cos(\omega_c x)}{(1 + \alpha\sin(\omega_c x))^{3/2}} \end{aligned} \tag{2.23}$$

Assuming $\alpha \ll 1$ one can see that the amplitude of the oscillation is $\Delta x \approx \frac{1}{2}[(v_d - v_{c1})x + \lambda_{p0}v_d]\alpha$. This means that for a superluminal quasiparticle the oscillations get smaller as the propagation distance x increases, whereas for a subluminal quasiparticle speed the amplitude of oscillation increases with the propagation distance. The minimum speed of the quasiparticle depends on v_{c1}, α and ω_c via

$$v_{c,min} = v_{c1}(1 - \frac{1}{2}\lambda_{p0}\alpha\omega_c) \tag{2.24}$$

If the minimum quasiparticle speed is too small, electrons will get self-injected and enlarge the bubble, deviating the quasiparticle from the desired trajectory. It is necessary then to have α and ω_c small enough that the speeds of the electrons are not sufficient to enter inside the bubble and alter the quasiparticle speed temporarily. We found that self-injection can occur, even for a superluminal quasiparticle, provided that α is sufficiently large. We therefore found that $\alpha = 0.05$ or smaller worked well for a wide range of quasiparticle velocities.

Ionization induced plasma density gratings [68] were demonstrated in the laboratory thanks to the beating pattern created by two ionizing laser pulses, and can be combined with a density ramp to adjust the mean quasiparticle velocity. Furthermore, other techniques to produce corrugated plasmas have also been experimentally demonstrated using additional two methods [69, 70]. The first uses an axicon to map radial intensity modulations of an incident pulse to a line focus with longitudinal intensity modulations. The line-focused pulse preferentially ionizes and heats a clustered gas where its intensity is high, which after, hydrodynamic expansion results in

a corrugated plasma channel. The second method uses periodically placed wires distributed along a slot gas jet to obstruct the flow of the clustered gas. The gas density is higher where it is unobstructed, resulting in density modulations upon ionization and heating by a laser pulse. Using these methods, modulations with $35 - 300$ μm periods with contrast ratios (modulation depths) in excess of 0.9 have been generated in densities relevant to our work (i.e. $n \simeq 10^{18}$ cm^{-3}).

2.6.2 Subluminal Quasiparticle Undulator Radiation

We compared Eq. (2.21) with additional simulations featuring longitudinally oscillating quasiparticles. In the sub-luminal regime with $v_c = 0.999c$, and according to Fig. 2.12a, the quasiparticle oscillates at the predicted frequency, set by the spatial periodicity of the plasma density profile. The agreement between theory and simulations is excellent.

Figure 2.12b shows the theoretical radiation spectrum associated with the quasiparticle trajectory alone, as given by Eq. 2.20. We therefore retrieved the theoretical quasiparticle trajectory using Fig. 2.12a, and used this trajectory in Eq. (2.20) suitably normalised to $\omega^2|\mathcal{S}|^2/(4\pi^2c^3)$. The different harmonics correspond exactly to the resonant frequencies given by Eq. (2.21). The radiation intensity at the resonant frequency harmonic m vanishes at the zeros of the corresponding Bessel J_m function. In Fig. 2.12c, we multiplied the radiation spectrum in Fig. 2.12b by $\omega^2|\mathcal{S}|^2/(4\pi^2c^3)$. We numerically determined $\mathcal{S}$ using the currents from the PIC simulation. This is a semi-theoretical radiation spectrum for the undulating quasiparticle. This result compares very well with the spectrum measured by the RaDiO simulation, shown in Fig. 2.12d. To provide further evidence, we show (yellow dashed line) the theoretically predicted Bessel function zeros in Figs. 2.12b-d.

2.6.3 Superluminal Quasiparticle Undulator Radiation

When $v_c > c$, the quasiparticle undulator spectrum contains features from quasiparticle Cherenkov radiation and undulator radiation. It is interesting to further explore the radiation intensity as a function of the radiation intensity at the Cherenkov angle corresponding to the average quasiparticle velocity. According to Eq. (2.20), the radiation intensity at the Cherenkov angle is given by:

$$\begin{aligned}\left.\frac{d^2I}{d\omega d\Omega}\right|_{\theta=\arccos(c/v_c)} &= \frac{\omega^2}{4\pi^2c^3}T^2\left|\boldsymbol{\mathcal{S}}(\omega)\right|^2\left|\sum_{m=-\infty}^{\infty}J_m\left(\frac{A\omega\cos\theta}{c}\right)\operatorname{sinc}\left\{-\frac{T}{2}m\omega_c\right\}\right|^2, \\ &\approx \frac{\omega^2}{4\pi^2c^3}T^2\left|\boldsymbol{\mathcal{S}}(\omega)\right|^2\left|J_0\left(\frac{A\omega\cos\theta}{c}\right)\right|^2\end{aligned} \tag{2.25}$$

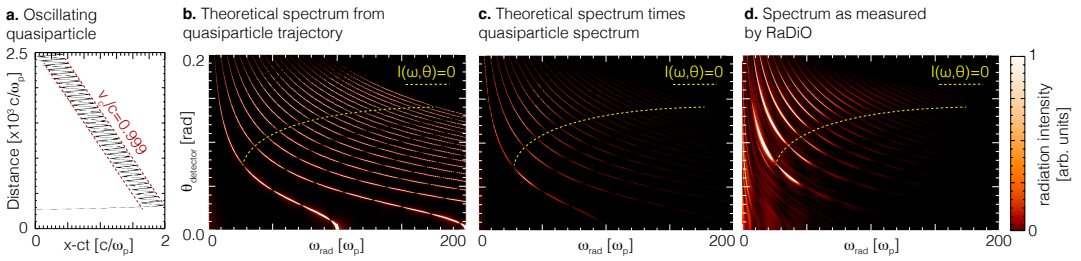

FIGURE 2.12: a. Waterfall plot showing the quasiparticle trajectory in frame moving at c. Each horizontal line corresponds to an on-axis lineout of the plasma density as a function of propagation distance. b. Theoretical spectral intensity in a virtual detector in the far field according to Eq. (2.20) with $\boldsymbol{\mathcal{S}}(\omega, \Omega) = 1$. c. Theoretical spectral intensity in a virtual detector according to Eq. (2.20) with $\boldsymbol{\mathcal{S}}(\omega, \Omega)$ taken from the simulation. d. Spectral intensity in a virtual detector as measured by RaDiO. The yellow dashed lines correspond to the position of zeros in Eq. (2.20). The yellow line in plots b-d represents the position of the zeros in Eq. (2.20). The Δx_c was measured at 0.15625 $[c/\omega_p]$, v_c was measured at $0.999c$ and $\omega_c = 0.1\omega_p$.

where we assumed that for sufficiently long propagation times T, all but the $m = 0$ component in the sum vanishes. This is an excellent approximation since

$$\mathrm{sinc}(-Tm\omega_c/2) \to 0 \tag{2.26}$$

as $T \to \infty$. Equation (2.25) is in excellent agreement with the simulation results, provided that we use the oscillation amplitude A provided by the simulations. Specifically, we observed that the zero emission frequencies in the radiation emission spectra matched the zeros of the J_0 function. This is clear in Fig. 2.13c-d.

Figure 2.13 depicts superluminal quasiparticle undulator radiation for $v_c = 1.0003c$. Figure 2.13a shows the quasiparticle trajectory, which propagates forward in the $(x - ct, x)$ frame. Theoretical undulator harmonics from the quasiparticle trajectory, shown in Fig. 2.13b, demonstrate the existence of a distinct radiation signal at the Cherenkov angle which is absent from standard sub-luminal undulator radiation. As discussed above in Eq. (2.25), this comes from the Bessel J_0 function. The semi-theoretical spectrum (Fig. 2.13c) and the spectrum from the RaDiO simulation (Fig. 2.13d) also agree very well. The agreement is further evidenced by the location of the zeros of the intensity spectrum which are set by the Bessel functions. This is particularly clear at the Cherenkov angle (white dashed line).

Figure 2.14 illustrates a superluminal undulating quasiparticle regime where $v_c = 1.003c$. We can identify, in Fig. 2.14a, two differences from earlier cases. First, the simulation captures oscillations from three quasiparticles. Second, the amplitude of the oscillation changes with time. Let us start by exploring the latter. Figure 2.14b shows the theoretical resonant harmonic spectrum predicted from the quasiparticle trajectory, found through Eq. (2.20) normalized to $\omega^2|\boldsymbol{\mathcal{S}}|^2/(4\pi^2c^3)$ and for fixed quasi-

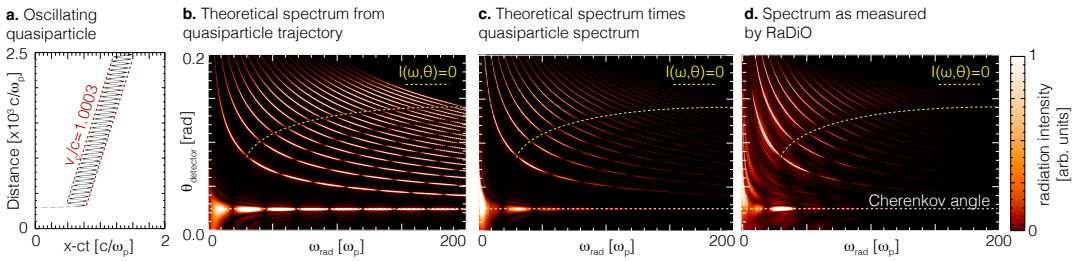

FIGURE 2.13: a. Waterfall plot showing the quasiparticle trajectory in frame moving at c. Each horizontal line corresponds to an on-axis lineout of the plasma density as a function of propagation distance. b. Theoretical spectral intensity in a virtual detector in the far field according to Eq. (2.20) with $\boldsymbol{\mathcal{S}}(\omega, \Omega) = 1$. c. Theoretical spectral intensity in a virtual detector according to Eq. (2.20) with $\boldsymbol{\mathcal{S}}(\omega, \Omega)$ taken from simulation. d. Spectral intensity in a virtual detector as measured by RaDiO The yellow dashed lines correspond to the position of zeros in Eq. (2.20). The yellow line in plots b-d represents the position of the zeros in Eq. (2.20). The Δx_n was measured at 0.125 $[c/\omega_p]$ and v_c was measured at $1.003c$. The Cherenkov angle corresponding to v_c is represented with a white dashed line.

particle oscillation amplitude. Because v_c is constant but the oscillation amplitude A changes, resonant frequencies [given by Eq. (2.21)] will not vary, but the zeros of the Bessel functions in Eq. (2.20) will move along the the resonant harmonic frequencies lines [Eq. (2.20)]. Therefore, the radiation is continuously emitted along the resonant harmonic frequencies defined by Eq. (2.21). This explains the difference between the theoretical lines in the semi-theoretical plot in Fig. 2.14c and RaDiO collected radiation in Fig. 2.14d.

Figure 2.14c contains additional new features, which we attribute to the quasiparticles that correspond to subsequent electron spikes after the first. Unlike in quasiparticle Cherenkov radiation, which features a clear angular separation of the radiation emitted by different quasiparticles, in the undulating case, this separation is not as clear since there is strong emission over a wider angular region than in Cherenkov radiation.

2.6.4 NOTABLE FEATURES OF QUASIPARTICLE UNDULATOR RADIATION

Figure 2.15 demonstrates the corresponding quasiparticle undulator radiation in the PWFA. The simulations in Fig. 2.15 use a longitudinally corrugated plasma channel combined with a density ramp. The density modulation depth and spatial period control the quasiparticle oscillation amplitude and frequency, respectively. Figure 2.15a shows undulator radiation from a subluminal quasiparticle. Just as if it were produced by a single charge, the quasiparticle undulator spectrum is more pronounced in the vicinity of the resonant frequencies, which are accurately predicted by Eq. (2.21).

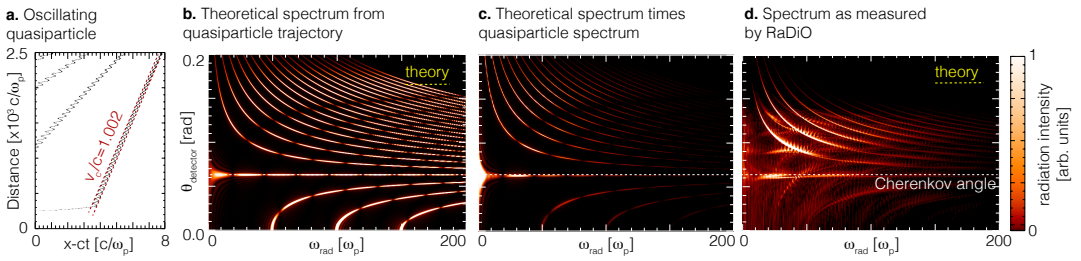

FIGURE 2.14: a. Waterfall plot showing three quasiparticle trajectories in frame moving at c. Each horizontal line corresponds to an on-axis lineout of the plasma density as a function of propagation distance. b. Theoretical spectral intensity in a virtual detector in the far field according to Eq. (2.20) with $\boldsymbol{\mathcal{S}}(\omega,\Omega) = 1$ and only considering the first quasiparticles c. Theoretical spectral intensity in a virtual detector according to Eq. (2.20) with $\boldsymbol{\mathcal{S}}(\omega,\Omega)$ taken from the simulation. d. Spectral intensity in a virtual detector as measured by RaDiO. The yellow dashed lines in b-d correspond to the position of zeros in Eq. (2.20). The Δx_c was not constant throughout the simulation but a value of 0.125 c/ω_p was assumed and v_c of the first quasiparticle was measured at $1.002c$. The Cherenkov angle corresponding to v_c is represented with a white dashed line.

We now investigate a new superluminal undulator radiation regime, which brings unique spectral signatures that are not accessible to conventional undulators. For example, Eq. (2.21) captures an unusual infinite Doppler shift effect at the Cherenkov angle, where $I \propto |\boldsymbol{\mathcal{S}}(\omega,\Omega)|^2 T^2 J_0^2(\omega \Delta x_c / v_c) \propto T^2$. Figures 2.15b-c show an example of superluminal quasiparticle undulator radiation. The inset in Fig. 2.15c (orange curve) reproduces the superradiant scaling with T^2 at the Cherenkov angle. The spectral intensity at the resonant frequencies outside the Cherenkov angle also grows with $I \propto T^2 \propto N^2$ (inset in Fig. 2.15c, yellow). Moreover, resonant frequencies asymptotically converge to the Cherenkov angle, as predicted by Eq. (2.21). Because the amplitude of the quasiparticle oscillation is large, multiple resonant frequency harmonics result in a broadband (single-cycle) pulse train, seen in the inset of Fig. 2.15b. The circled region in Fig. 2.15c show an interesting enhancement effect occurring when resonant harmonics from multiple quasiparticles cross.

2.6.5 GENERAL

PARTICLE-IN-CELL SIMULATIONS

It is important to establish what are the parameters used in the computer simulations already shown. Osiris simulations consider an intense laser pulse or particle beam as drivers to excite a plasma wave. These numerical experiments operate in the so-called nonlinear blowout or bubble regime, standard in plasma acceleration experiments. To enter in the nonlinear blowout regime, particle driver simulations (Fig. 2.4, Fig. 2.5

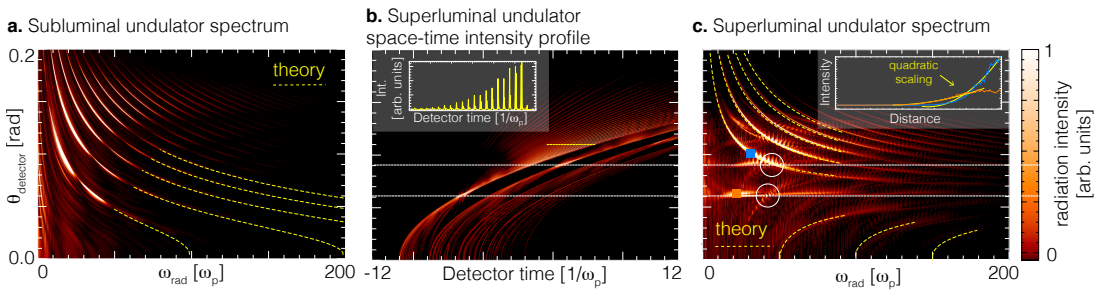

FIGURE 2.15: Quasiparticle undulator radiation for an oscillating quasiparticle with $\omega_c = 0.1\ \omega_p$ and $\Delta x_c = 0.25c/\omega_p$. a. Spectral intensity of undulator radiation from a subluminal quasiparticle with $v_c/c = 0.999$. Theoretically calculated resonant frequencies are in yellow. b. Spatiotemporal profile of the radiated intensity in a virtual detector in the far field from superluminal oscillating quasiparticle with $v_c/c = 1.0003$. The white dashed lines mark the Cherenkov angle corresponding to the first and second quasiparticle. The inset shows a lineout taken at the interval defined by the yellow dashed line. c. Corresponding spectral radiation intensity. The yellow dashed lines are the theoretically calculated resonant frequencies. The inset shows the evolution of the peak intensity with propagation distance at the positions marked by the squares (Cherenkov angle in orange, first resonant harmonic in blue). The circles show crossing positions between resonant frequency harmonics produced by different quasiparticles.

and Fig. 2.15) use an over-dense electron bunch. The bunch density profile in the (3D) simulations is given by:

$$n(x,y,z) = n_{b0} \exp\left(-\frac{z^2}{2\sigma_z}\right) \exp\left(-\frac{x^2}{2\sigma_x}\right) \exp\left(-\frac{y^2}{2\sigma_y}\right), \tag{2.27}$$

where n_{b0} is the peak electron beam density, x is the longitudinal direction, y and z are the transverse directions and $\sigma_{x/y/z}$ is the bunch size in the direction x, y or z. Corresponding total bunch charge Q is:

$$Q[\mathrm{nC}] = n_{b0}[\mathrm{cm}^{-3}]\sigma_x[\mu\mathrm{m}]\sigma_y[\mu\mathrm{m}]\sigma_z[\mu\mathrm{m}]\frac{2\sqrt{2}\pi^{3/2}}{6.24\times10^{21}} \tag{2.28}$$

Simulations use peak bunch density $n_{b0} = 120n_0$, relativistic factor $\gamma = 19569.5$ and energy $E \simeq 10$ GeV. The electron bunch momentum spread in the x, y, and z directions is $(\Delta p_x, \Delta p_y, \Delta p_z) \simeq (195.6, 18.6, 18.6)\ m_e c$. The bunch sizes in all three dimensions is $(\sigma_x, \sigma_y, \sigma_z) \simeq (0.19, 0.19, 0.19)\ c/\omega_p$. For a plasma density $n_0 = 8.35 \times 10^{16}\ \mathrm{cm}^{-3}$ and for an electron bunch with 1 nC, as available in state-of-the-art facilities, this corresponds to $(\sigma_x, \sigma_y, \sigma_z) = (3.4, 3.4, 3.4)\ \mu$m.

Simulations with a laser pulse (Fig. 2.6) consider a diffraction limited, Gaussian laser pulse with peak normalised vector potential $a_0 = 4$ (corresponding to peak intensity $I = 3.3 \times 10^{19}\ \mathrm{W/cm}^2$). Initially, the laser duration at full-width-half-maximum

is $\tau = 2.76\ c/\omega_p = 35$ fs. Transversely, the laser pulse is Gaussian with spot-size $w_0 = 4.89\ c/\omega_p = 18.6\ \mu$m. The ratio between the central laser frequency, ω_0, and plasma frequency, $\omega_p = [e^2 n_0/(m_e \epsilon_0)]^{1/2}$, is $\omega_0/\omega_p = 30$. This is equivalent to a background plasma density $n_0 = 1.95 \times 10^{18}$ cm^{-3} for a central laser wavelength $\lambda_0 = 2\pi c/\omega_0 = 800$ nm. Other values of the ratio ω_0/ω_p, (or, equivalently, different plasma densities) yield identical conclusions.

Simulations use a window that moves at c with dimensions $14 \times 13.2 \times 13.2$ [$20 \times 65 \times 65$] $(c/\omega_p)^3$ for the particle driver [laser driver] configuration with a timestep of 0.0048 [0.00665] $(1/\omega_p)$. The simulation window contains $2800 \times 330 \times 330$ [$3000 \times 324 \times 324$] cells, each with $2 \times 1 \times 1$ [$2 \times 1 \times 1$] particles.

The plasma density profile is composed of an initial linear upramp followed by an engineered profile to support constant wakefield phase speeds. The profile is given by

$$n(x) = \begin{cases} 0 & \text{if } x \in [0, x_1[\\ \frac{x-x_1}{x_2-x_1} & \text{if } x \in [x_1, x_2] \\ \{1 + \alpha \sin[\omega_c (x - x_2)]\} \frac{\lambda_{p0}^2}{[(1-v_c)(x-x_2)+\lambda_{p0}]^2} & \text{if } x \in]x_2, x_2 + \frac{\lambda_{p0}}{v_c - 1}[\end{cases} \tag{2.29}$$

where x_1, x_2 are the start and end of the linear ramp ($x_2 - x_1 = 100 c/\omega_p$ for Fig. 2.4 and Fig. 2.5 and $60 c/\omega_p$ for Fig. 2.17), α controls the undulation amplitude (for Fig. 2.5 and Fig. 2.6 α is set to 0, in Fig. 2.15 α was set to 0.05), ω_c is the undulator frequency (was set to $0.1\omega_p$ for simulations in Fig. 2), λ_{p0} is the plasma wavelength.

2.7 BRIGHTNESS

To estimate the brightness of the source, we start with the expression for the radiation energy per frequency per solid angle in the far-field (in cgs units) [54]:

$$\frac{d^2 I}{d\omega d\Omega} = \frac{\omega^2}{4\pi^2 c^3} \left| \int \int d\mathbf{r} dt\ \mathbf{n} \times [\mathbf{n} \times \mathbf{j}(\mathbf{r}, t)] \exp[i\omega(t - \mathbf{n} \cdot \mathbf{r}/c)] \right|^2 \tag{2.30}$$

For relativistic electrons, $|\mathbf{n} \times [\mathbf{n} \times \mathbf{j}]| \sim n_{\rm qp} e c \sin\theta$, where $n_{\rm qp}$ is the average quasiparticle density. To perform the spatial integration we then approximate the quasiparticle by a uniform current cube with transverse and longitudinal sizes given by $\sigma_\perp c/\omega_p$ and $\sigma_\parallel c/\omega_p$ respectively. To perform the time integration we multiply the resulting integrand by the propagation time T/ω_p, and assume that we are close to the Cherenkov angle for which the complex exponential in Eq. (2.30) is close to unity. The resulting photon number emitted by the quasiparticle during T/ω_p is the ratio between the radiation energy at a given frequency and the corresponding photon energy

$\hbar\omega$, being given by:

$$\frac{\mathrm{d}^2 N_{\mathrm{ph}}}{\mathrm{d}\omega \mathrm{d}\Omega} = \frac{\omega}{4\pi^2 \hbar c^3} n_{\mathrm{qp}}^2 \sin^2(\theta) \left(\frac{T}{\omega_p}\right)^2 \left(\frac{\sigma_\perp c}{\omega_p}\right)^4 \left(\frac{\sigma_\parallel c}{\omega_p}\right)^2. \tag{2.31}$$

The brightness corresponds to the number of photons emitted within a small bandwidth $\Delta\omega/\omega \simeq 10^{-3} = 0.1\%$, and within a small angular spread $\Delta\theta^2 = 1\ \mathrm{mrad}^2$. If we assume that the photon number is constant within the bandwidth and angular spread (which is an excellent approximation for our conditions), the brightness B, which is the number of photons emitted per unit time, per bandwidth, per solid angle, is $(\mathrm{d}N_{\mathrm{ph}}/\mathrm{d}\Omega)\Delta\theta^2(\Delta\omega/\omega)(\omega_p/T)(\omega_p/\sigma_\perp c)^2$. This yields:

$$\begin{aligned} &B[\mathrm{ph/s/mm^2/BW/rad^2}] \simeq \\ &\simeq \frac{\alpha c}{4\pi^2} \left(\frac{\omega}{\omega_p}\right)^2 \left(\frac{\Delta\omega}{\omega}\right) \Delta\theta^2 \left(\frac{c}{\omega_p}\right)^3 n_{qp}^2 \sin^2\theta\ (T[\omega_p^{-1}])^2 (\sigma_\perp[c/\omega_p])^2 (\sigma_\parallel[c/\omega_p]) \end{aligned} \tag{2.32}$$

in which α is the fine structure constant, c is the speed of light, ω the emitted wavelength, ω_p the plasma frequency, n_{qp} the quasiparticle density, $(\Delta\omega/\omega)$ the bandwidth, T is the coherent emission time normalized to ω_p^{-1}, and $\Delta\theta^2$ is the angular apperture. This equation holds for wavelengths larger than $\sigma_\parallel$.

An example, consistent with standard PWFA or LWFA setups, is for $n_0 = 10^{17}\ \mathrm{cm}^{-3}$, $n_{qp} = 100 n_0$, $\sigma_\parallel = 300\mathrm{nm} = 0.02\ c/\omega_p$, $\sigma_\perp = 1.6\mu\mathrm{m} = 0.1 c/\omega_p$, $T = 5\mathrm{ps} \simeq 100\omega_p^{-1}$, $\Delta\theta = 1$ mrad, and a bandwidth of 0.1% leads to

$$B = 5 \times 10^{28} \mathrm{ph/s/mm^2/0.1\%BW/mrad^2}$$

for photons of 4 eV at the Cherenkov angle. Using, instead, $n_0 = 10^{18}\ \mathrm{cm}^{-3}$ and keeping the quasiparticle size and propagation time constant in units of c/ω_p and $1/\omega_p$, respectively, the brightness is $B = 2 \times 10^{29} \mathrm{ph/s/mm^2/0.1\%BW/mrad^2}$ for photons of 12 eV at the Cherenkov angle. It is, nevertheless possible to obtain even smaller quasiparticle sizes. We show an example with similar brightnesses at about 40 eV below in section 2.5. A comparison with other light sources is shown in Fig. 2.16.

2.8 Numerical calculation of the brightness from PIC simulations

To calculate brightness coming from cylindrically symmetric simulations, we first recall the definition of $\boldsymbol{\mathcal{S}}(\omega, \Omega)$:

$$\boldsymbol{\mathcal{S}}(\omega, \Omega) = \int d\boldsymbol{\xi}\ \mathbf{n} \times [\mathbf{n} \times \mathbf{j}(\boldsymbol{\xi})] \exp[-i\omega\ \mathbf{n} \cdot \boldsymbol{\xi}/c]. \tag{2.33}$$

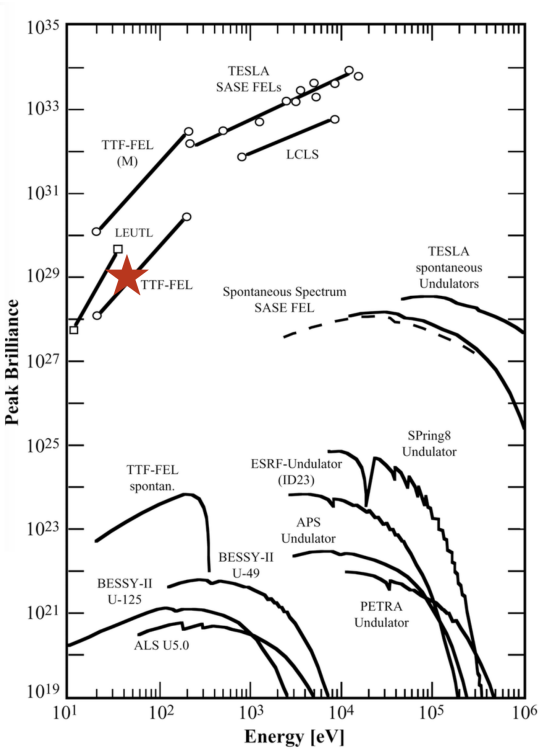

FIGURE 2.16: Comparison between several plasma light sources. Our example is shown with a red star.

To perform the integration in Eq. (2.33), we assume cylindrical geometry and symmetry. In cylindrical coordinates, $\mathbf{j}(\boldsymbol{\xi}) = (j_x, j_r, j_\phi = 0)$, where j_x is the current along the longitudinal x direction, j_r is the radial current, and $j_\phi = 0$ is the azimuthal current, which we can neglect in a cylindrically symmetric geometry. The corresponding 3D cartesian geometry current components is then given by:

$$\mathbf{j}(x, y, z) = (j_x, j_r \sin\phi, j_r \cos\phi), \tag{2.34}$$

where ϕ is the polar angle. By substituting Eq. (2.34) in Eq. (2.33) and performing the angular integration along ϕ leads to:

$$\begin{aligned}
&\boldsymbol{\mathcal{S}}(\omega, \Omega) = \\
&\{ -2\pi \int e^{-ix\omega\cos\theta} r \sin\theta \left(iJ_1(r\omega\sin\theta) j_r(x,r)\cos\theta + J_0(r\omega\sin\theta) j_x(x,r)\sin\theta \right) \mathrm{d}r\mathrm{d}x, \\
&\pi \int e^{-ix\omega\cos\theta} r \left(2iJ_1(r\omega\sin\theta) j_r(x,r)\cos^2\theta + J_0(r\omega\sin\theta) j_x(x,r)\sin\theta \right) \sin 2\theta \mathrm{d}r\mathrm{d}x, \\
&0\},
\end{aligned} \tag{2.35}$$

Equation (2.35) can be directly calculated from the diagnostics from cylindrically symmetric simulations, or from 3D simulation results assuming cylindrical symmetry. To determine the brightness, we follow the procedure outlined above.

The following formula provides an estimate for the peak brightness:

$$B\ [\mathrm{ph/s/mm^2/0.1\%BW/mrad^2}] \simeq$$
$$\simeq \frac{\alpha(c[\mathrm{cm/s}])}{4\pi^2\times 10^{11}}\left(\frac{\omega}{\omega_p}\right)^2\left(\frac{c}{\omega_p}\right)^3 (n_{\mathrm{qp}}[\mathrm{cm^{-3}}])^2\left(T[{\omega_p}^{-1}]\right)^2\left(\sigma_\perp[\mathrm{c}/\omega_p]\right)^2\left(\sigma_\parallel[\mathrm{c}/\omega_p]\right)\sin^2\theta, \tag{2.36}$$

where $\alpha \simeq 1/137$ is the fine structure constant, n_{qp} is the quasiparticle density, $\sigma_\perp$ and $\sigma_\parallel$ are the transverse and longitudinal quasiparticle sizes. Equation (2.36) holds for radiation wavelengths λ that are longer than the quasiparticle size (i.e., for $\lambda \gtrsim \sigma_\parallel$).

2.8.1 Avoiding slippage effect

Equation (2.36) predicts a favourable scaling of peak brightness with propagation distance as $B \propto T^2$. This scaling is a result of an interesting and important aspect, according to which for the coherent part of the quasiparticle spectrum, the radiated intensity may grow without bound, and even surpass the theoretical limit of an FEL. In an FEL there is slippage between the radiation and electron microbunch. This slippage effect fundamentally limits constructive interference of radiation emitted at separate times during propagation. Superluminal quasiparticles, travelling with a constant velocity, provide a mechanism to completely avoid this slippage effect. This unusual scaling cannot be realised with single electrons (or electron bunches) that travel slower than c. In practice quasiparticles may accelerate, as a result of non-ideal plasma density profiles and driver self-evolution. These effects lead to a time-dependent Cherenkov angle spread, which limits the peak brightness. A rule of thumb for the maximum propagation time T over which constructive interference occurs is given by $T \simeq 2\pi c/(\omega\Delta v)$, where Δv is the quasiparticle velocity variation. Thus, and while an absolutely constant $v_c \geq c$ may be complicated to achieve in practice, this never ending constructive interference regime is still an exciting possibility.

Equation (2.36) can accurately predict peak brightness considering an appropriate limit for T. According to Eq. (2.36), peak brightness of

$$B \simeq 2\times 10^{29}\ \mathrm{ph/s/mm^2/0.1\%BW/mrad^2} \tag{2.37}$$

can be achieved for a quasiparticle with density $n_{\mathrm{qp}} = 10^{20}\ \mathrm{cm^{-3}}$ (corresponding to $100n_0$, where $n_0 = 10^{18}\ \mathrm{cm^{-3}}$ is a typical background plasma density), with $\sigma_\perp = 0.1\ c/\omega_p = 0.5\ \mu\mathrm{m}$, $\sigma_\parallel = 0.02\ c/\omega_p = 0.1\ \bar{}\mathrm{m} \simeq c/\omega$ (corresponding to 10 eV photons), $\theta = 0.1$ rad and $T = 100\ \omega_p^{-1} = 0.5\mathrm{mm}/c$, closely corresponding to the simulation

results in Fig. 2.5. Figure 2.17 shows an estimate for the peak brightness according to Eq. (2.36) as a function of photon energy. It demonstrates high peak brightness over a photon energy range spanning nearly ten octaves, and encompassing regions where light sources are scarce (e.g., THz gap and extreme ultra-violet). Peak brightness for extreme ultra-violet photons is hence comparable to free-electrons lasers operating in the same frequency range [41]. In comparison with other sources, our quasiparticle radiation is much brighter than betatron, Compton or bremsstrahlung radiation, albeit only good in the XUV range.

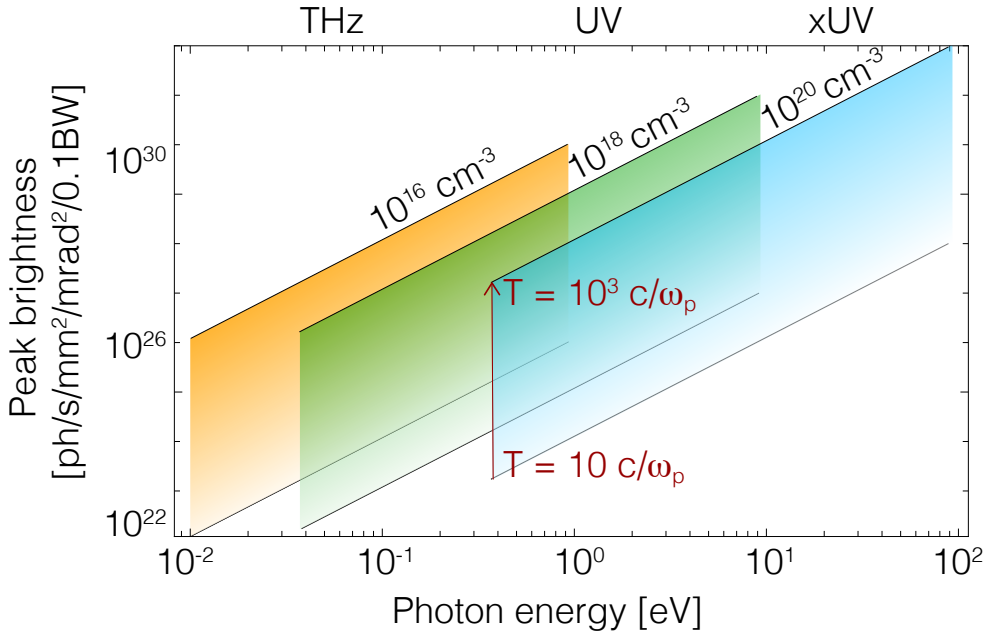

FIGURE 2.17: Peak brightness estimated as a function of photon energy for nonlinear wakefield quasiparticle radiation, spanning frequencies ranging from THz to extreme ultra-violet. The figure shows peak brightness calculated using Eq. (2.36) for three different plasma densities, considering $\sigma_\perp = 0.1\, c/\omega_p = 0.5\ \mu$m, $\sigma_\parallel = 0.02\, c/\omega_p = 0.1\ \mu$m $\simeq c/\omega$, and $n_{\rm qp} = 100\, n_0$. The bottom of each shaded region uses $T = 10/\omega_p$, and the top considers $T = 1000/\omega_p$. The photon energy range at each density corresponds to frequencies ranging from $\omega \geq \omega_p$ (only frequencies above ω_p can propagate out of the plasma) and $\omega \leq 250\ \omega_p$ (typical upper frequency boundary radiated by nonlinear wakefield quasiparticles)

2.9 CONCLUSIONS

Critical to the realization of the concept is the ability to control the quasiparticle velocity and acceleration. Thus, while the concept paves the way to an exciting range of new possibilities, the quasiparticle velocity can only be controlled up to a given

precision in experiments, which provides practical limits for obtaining constructive interference in the quasiparticle radiation concept, and limit its peak brightness.

In general, quasiparticle trajectories in nonlinear wakefields can be controlled using tailored plasma density profiles, but also structured laser pulses with tuneable group velocities [72, 71, 73, 74, 75]. Because there is much freedom to control the quasiparticle velocity, the quasiparticle radiation concept can enable a new class of temporally coherent, superradiant light sources in previously unconsidered conditions and configurations. Examples include superradiant versions of quasiparticle Thomson scattering, photon acceleration, and synchrotron radiation. Moreover, the concept can be used, for example, to explore new effects such as the reversed Doppler-shift predicted for superluminal particles [76] or to provide a surrogate for studying radiation from the extreme accelerations experienced in the vicinity of exotic astrophysical objects, such as black holes. A generalization of our concept for nonlinear optics is possible by replacing the current density $\mathbf{j}$ by the time derivative of the polarisation density of a nonlinear optical system, i.e., by making the substitution $\mathbf{j} \rightarrow \partial_t \mathbf{P}$, where $\mathbf{P} = \epsilon_0 \chi \mathbf{E}$ and χ is the susceptibility tensor, which can depend nonlinearly on the electric field $\mathbf{E}$. Similarly, ordered arrangements of spin can be interpreted as quasiparticles and analyzed using Eqs. (2.4) and (2.5) by substituting $\mathbf{j} \rightarrow \nabla \times \mathbf{M}$, where $\mathbf{M}$ is the magnetization. In the near term, quasiparticle radiation can be realized using widely available experimental resources, making it suitable for experimental demonstration at existing laser and plasma accelerator laboratories, including hybrid LWFA-PWFA regimes.

2.10 Outputs

2.10.1 Papers in refereed Journals

B. Malaca, M. Pardal, D. Ramsey, J.R. Pierce, K. Weichman, I.A. Andryiash, W.B.Mori, J.P.Palastro, R.A.Fonseca, J.Vieira, *Coherence and superradiance from a plasma-based quasiparticle accelerator*, Nature Photonics (2023),
https://doi.org/10.1038/s41566-023-01311-z

2.10.2 Invited Talks

B. Malaca, M. Pardal, D. Ramsey, J.R. Pierce, K. Weichman, I.A. Andryiash, W.B.Mori, J.P.Palastro, R.A.Fonseca, J.Vieira, *Coherence and superradiance from a plasma-based quasiparticle accelerator*, European Advanced Accelerator Concepts Workshop, Isola d'Elba, Italy (September 2023)

2.10.3 Contributed Talks

B. Malaca, M. Pardal, D. Ramsey, J.R. Pierce, K. Weichman, I.A. Andryiash, W.B.Mori, J.P.Palastro, R.A.Fonseca, J.Vieira, *Coherence and superradiance from a plasma-based quasi-particle accelerator*, Laser and Plasma Accelerators Workshop, Lagos, Portugal (March 2023)

B. Malaca, M. Pardal, D. Ramsey, J.R. Pierce, K. Weichman, I.A. Andryiash, W.B.Mori, J.P.Palastro, R.A.Fonseca, J.Vieira, *Superradiance and temporal coherence in the non-linear blowout regime*, Advanced Accelerator Concepts Workshop, Long Island, NY, USA (November 2022)

2.10.4 Posters in Conferences

B. Malaca, M. Pardal, D. Ramsey, J.R. Pierce, I.A. Andryiash, W.B.Mori, J.P.Palastro, R.A.Fonseca, J.Vieira, *Coherent light from plasma waves in density gradients*, Lisbon, Portugal (May 2022)

B. Malaca, M. Pardal, D. Ramsey, J.R. Pierce, I.A. Andryiash, W.B.Mori, J.P.Palastro, R.A.Fonseca, J.Vieira, *Superradiance from superluminal nonlinear plasma wakefields*, 48^{th} European Conference on Plasma Physics, remote (June 2022)

B. Malaca, J.Vieira, *Superluminal plasma waves and coherent radiation*, PhD Open Days, Lisbon (November 2021)

2.10.5 Prizes

PPCF/EPS Student Poster Prize at the 48th EPS Plasma Physics conference

2.10.6 Media attention

This work has been featured in the publication BBC Science Focus, Gizmodo, and Physics World, along with 36 other different outlets, according to Altmetric.

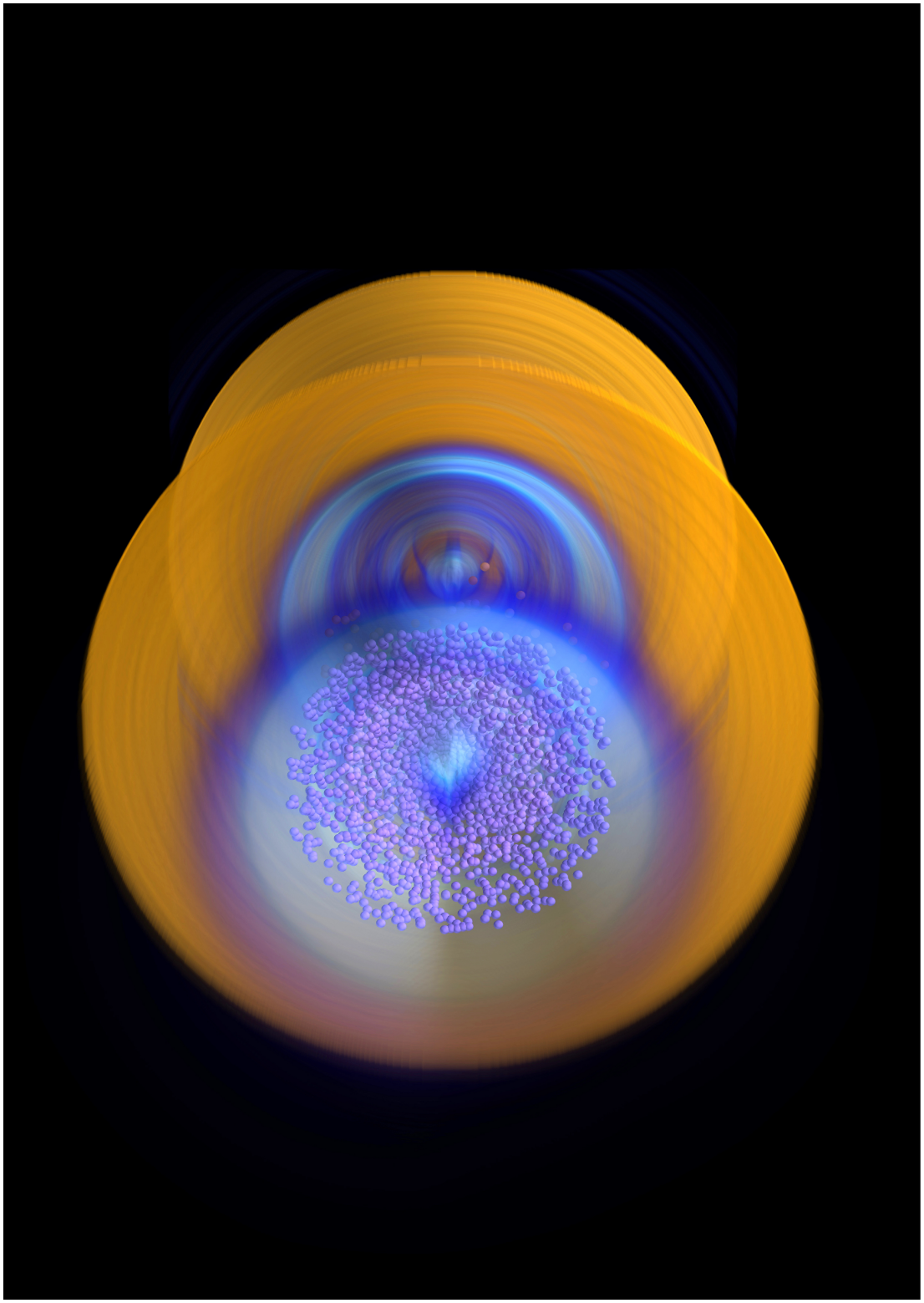

FIGURE 2.18: 3D Rendering of the quasiparticle emitting two cones of Cherenkov emission in a laser wakefield accelerator. In blue we observe the plasma wave. In yellow we observe the light emitted off-axis and in purple dots we see the electrons.

CHAPTER 3

IMPLEMENTATION OF SPACE-TIME WAVEPACKETS IN OSIRIS

3.1 INTRODUCTION

In Chapter 2, we developed the theory on radiation emitted by quasiparticles. One of the main examples was the superluminal quasiparticle, as it could travel faster than the speed of light even though the constituents were all subluminal electrons. One can ask if a group of photons in a laser could replicate the same concept, by forming a focus (region where electromagnetic fields are higher) that would travel with an arbitrary speed. Interestingly, experimental work was done to demonstrate such pulses [78, 79].

These pulses are interesting on their own, and one can envision several applications if they could be reliably produced in a lab. One of such applications has precisely to do with the quasiparticle concept. In Chapter 2 we used both particle beams and laser pulses travelling at c to generate plasma waves. By changing the plasma density along the propagation direction, we showed how some single-particle effects could be replicated by these plasma waves, such as the emission of Cherenkov-like radiation if the quasiparticle was superluminal, or the generation of quasiparticle undulator radiation.

A superluminal focus could replace the Gaussian laser driver in the setup and therefore eliminate the need to shape the plasma density profile to control the quasiparticle trajectory. In combination with tailored plasma density profiles, these new drivers could expand the controlability on the quasiparticle trajectories accessible in experiments. The goal of this Chapter is to show how we implemented this kind of pulses into our particle-in-cell code OSIRIS [35].

Space-time wavepackets are optical wave packets with spatio-temporal correlations. Essentially, this means that a certain frequency ω that is present in the packet is associated with a wavevector $\mathbf{k}$, such that one can write ω as a function of $\mathbf{k}$. By increasing the bandwidth of these wavepackets, more available wavevectors become available, enabling the apparent group speed of the wavepacket focus to be both smaller or larger than the speed of light c [78].

One of the first implementations of pulses with a moving focus was thought by Froula et al [71, 72]. This was based on a chirped pulse (where the central frequency changes along the beam) that was focused with a diffractive lens. This lens focus different frequencies at different positions and therefore the work proved you could have speeds from $-8c$ up to $39c$. Because of the chirp effect, the exact profile at focus varies.

Here we focus on nonspreading wave packets, meaning that the profile at focus does not change with time [89] because these pulses promise to excite shape preserving plasma waves, of interest for high quality plasma acceleration and light sources. Recently, scientists have found ways to create such pulses using special optics [71, 78, 73, 80]. These pulses are a focus of much attention because they provide an additional degree of freedom in something as fundamental as the speed of a laser pulse, which is a limitation for plasma acceleration: if electrons are accelerated to the group speed of the laser in plasma (which is smaller than c) they start overtaking the accelerating structure (called dephasing) which limits the plasma density in experimental setups. These wave packets could also add new capabilities to existing plasma-based acceleration. For example, wave packets with orbital angular momentum (OAM) can transmit it to accelerated particles in plasma [77]. These pulses could provide new properties for plasma acceleration and radiation as well. The first step to study these properties is to have these wave packets available on PIC codes, which is what we aim to do in the remainder of the chapter.

This chapter is organized as follows: In section 3.2 we revisit the theoretical work first proposed by Abouraddy et al [78, 79]. In section 3.3 we show how to implement these pulses in OSIRIS. In section 3.6 we show how the predicted pulses behave in vacuum and in plasma. In section 3.7 we showcase our 3D implementation of these pulses.

3.2 THEORY

We based this theoretical treatment of these pulses in the work of Kondakci and Abouraddy [78]. In that work they were able not only to introduce the space-time wave packet concept but also to create space-time wave packets experimentally in 2D light-sheets. It is important to refer that in that work z is the longitudinal direction and x is the

transverse direction, while for continuity reasons we take x as longitudinal direction and y as transverse.

3.2.1 PLANE WAVES

The simplest case is a two-dimensional space-time wave packet. Let us take x to be the longitudinal direction and y to be the transverse direction. By taking the Fourier transform of the electromagnetic fields, it is possible to write any wave packet in terms of plane waves, where both the electric and magnetic fields are written as $\sum_{k_x,k_y} A_{k_x,k_y} e^{i(k_y x_y + k_x x - \omega t)}$, where A_{k_x,k_y} is the amplitude of the plane wave, ω is the frequency, t is time, and k_x and k_y are the wavevectors in the x and y directions, respectively. Our goal is to determine how to choose the triplet (k_x, k_y, ω) to obatin a space-time wave packet. Using the dispersion relation in a vacuum, $k^2 = \omega^2/c^2$, we can write

$$k_x^2 + k_y^2 = (\omega/c)^2, \tag{3.1}$$

which is the equation for a cone in the (k_x, k_y, ω) space. All plane waves have to abide by this rule, which restricts the whole three-dimensional space to a two-dimensional surface (the cone). As said in section 3.1, we are interested in pulses where the focus travels with a certain group velocity $\tilde{v} \neq c$. To accomplish this, one can write a relationship between ω and k_x, as

$$\omega/c = k_0 + (k_x - k_0)\tilde{v}/c, \tag{3.2}$$

where $k_0 = \omega_0/c$, ω_0 are the wavevector and frequency of the solution of the equation for a plane wave pointing longitudinally ($k_y = 0$) [78], and $\tilde{v}$ the speed of the focus. To get the group speed in the longitudinal direction, we need to take $\partial\omega/\partial k_x$ which gives $\tilde{v}$ (for any value of k_0). Equation (3.2) can also be seen as the equation for a plane that makes an angle $\theta = \arctan(\tilde{v})$ with the (k_x, k_y) plane.

Let us explore the relation between k_y, k_x, and ω. By using both Eq. (3.1) and Eq. (3.2), one can write

$$\omega = c\sqrt{k_y^2 + k_x^2} = \omega_0 + (k_x - \omega_0/c)\tilde{v} \tag{3.3}$$

Equation (3.3) gives the intersection beween the code given by Eq. (3.1) and the tilted plane given by Eq. (3.2). By taking the square on each side of the equation and solving for ω_0 we get

$$\begin{aligned} 0 &= \omega_0^2\left(1 - \frac{\tilde{v}}{c}\right)^2 + \omega_0\left[2k_x\frac{\tilde{v}}{c}\left(1 - \frac{\tilde{v}}{c}\right)\right] + \left[k_x^2\left(\frac{\tilde{v}^2}{c^2} - 1\right) - k_y^2\right] \Leftrightarrow \\ \Leftrightarrow \omega_0 &= \frac{-k_x\frac{\tilde{v}}{c} \pm \sqrt{k_x^2 + k_y^2}}{1 - \frac{\tilde{v}}{c}} \end{aligned} \tag{3.4}$$

Solving Eq. (3.4) for k_y gives:

$$k_y = \pm\sqrt{([1-\tilde{v}/c]\omega_0 + k_x\tilde{v}/c)^2 - k_x^2} \tag{3.5}$$

Let us discuss the significance of Eq. (3.5): every plane wave that satisfies Eq. (3.5) abides by the vacuum dispersion relation, and so it is a solution of Maxwell's equations. It must also satisfy Eq. (3.2), designed to imprint an arbitrary longitudinal group velocity to our system. This does not mean that each plane wave has a longitudinal group velocity $\tilde{v}$, as the group velocity comes from the superposition of multiple waves. However, when multiple different plane waves satisfy 3.5, we will observe that the intensity peak of the envelope resulting from plane-wave superposition travels at $\tilde{v}$, even though each wave travels at the speed of light c.

Equation (3.5) determines the possible wavevectors and frequencies in these space-time wave packets. To get the range of possible k_x, one can immediately see that what is inside the square root must be positive or zero. Hence,

$$[(1-\tilde{v}/c)\omega_0 + k_x\tilde{v}/c]^2 \geq k_x^2 \tag{3.6}$$

Because of the inequality between two squares of the type $a^2 > b^2$, the solution is $|a| > |b|$. The resulting relation between ω, k_x and $\tilde{v}$ depends on the sign of both a and b. Let us consider that the pulse is moving forward ($k_x > 0$). This just means that there are only forward-travelling plane waves. This does not imply that the speed of the focus $\tilde{v}$ is positive, as both features are not correlated anymore. Assuming both squared quantities to have the same sign, we obtain

$$(1-\tilde{v}/c)\omega_0 \geq (1-\tilde{v}/c)k_x. \tag{3.7}$$

The solution depends on the sign of $(1-\tilde{v}/c)$. If this is positive (meaning that the peak of the envelope travels subluminally), then $k_x \leq \omega_0/c$. For superluminal motion, however, we obtain $k_x \geq \omega_0/c$. From Eq. (3.2) , we get that for subluminal pulses $\omega < \omega_0$ and for superluminal pulses $\omega > \omega_0$. This suggests that not all wavevectors (or frequencies) may be present in our space-time wave packets.

3.2.2 Electromagnetic wave packets

Now that we have proper understanding of the plane waves that may go into space-time wave packets, one can now establish how to create pulses from the superposition of plane waves. From here on, we are no longer reviewing Refs. [78, 79] but rather presenting a more detailed and in-depth analysis about the properties of these wave packet solutions.

WAVE PACKET WITH PRECRIBED TRANSVERSE ENVELOPE PROFILE

Let us consider that we are looking for a electric field with a transverse envelope profile at focus (we will clarify what the focus is afterwards) given by $\Psi(y)$. The magnetic field can be retrieved from the electric field by using Maxwell's equations, and that calculation will be done afterwards.

Our electric field could be written as

$$\boldsymbol{E}(x,y,t) = \int \mathrm{d}k_y \tilde{\Psi}(k_y) e^{i(k_y y + k_x(k_y)x - \omega(k_y)t} \boldsymbol{e_p} \tag{3.8}$$

where E is the electric field in the polarization direction, $\tilde{\Psi}$ is the Fourier transform of $\Psi(y)$, and we explicitly included the dependency of k_x and ω on k_y. Because all the plane waves must satisfy Eq. (3.5), one can substitute ω by the right hand side of Eq. (3.2) and by proper manipulation we obtain

$$E(x,y,t) = e^{i(k_0 x - \omega_0 t)} \int \mathrm{d}k_y \tilde{\Psi}(k_y) e^{i(k_y y + [k_x(k_y) - k_0][x - t\tilde{v}])} \tag{3.9}$$

It is clear that taking $x - t\tilde{v} = 0$, we get

$$E(x,y,t) = e^{i(k_0 x - \omega_0 t)} \Psi(y) \tag{3.10}$$

which coincides with the definition of an envelope profile at focus (considering that the focus exists at $x(t) = t\tilde{v}$). For values of $x - t\tilde{v}$ equal to a constant $c_1 \neq 0$ we get

$$E(x,y,t) = e^{i(k_0[x - c_1] - \omega_0 t)} \int \mathrm{d}k_y \tilde{\Psi}(k_y) e^{i(k_y y + c_1 k_x(k_y))} \tag{3.11}$$

which is still the oscillating profile from Eq. (3.10) (apart from a phase factor) times a function that does not depend on t or x. This means that the resulting eletric field is envelope-invariant along the coordinate $x - \tilde{v}t$. However, the precise envelope can only be calculated with knowledge of $k_x(k_y)$, which is set by ω_0[1] and $\tilde{v}$. Because of this invariance, Eq. (3.9) is normally presented as

$$E(x,y,t) = e^{i(k_0 x - \omega_0 t)} F(y, x - \tilde{v}t) \tag{3.12}$$

where F contains all the properties described above. However, using this formulation F is itself dependent on ω_0 and $\tilde{v}$, and has no immediate connection with Ψ, except at $x - \tilde{v}t$, where $F(y,0) = \Psi(y)$. The function Ψ will now be considered arbitrary but some restrictions will apply, as one can find later in subsection 3.3.3.

[1] which right now appears to be the oscillating part of the electric field, even though this will be discussed further in section 3.3.3

WAVE PACKET WITH PRESCRIBED LONGITUDINAL PROFILE

In Eq. (3.9) the profile was imposed in the transverse direction, by $\Psi(y)$. It is also possible to impose a profile in the parallel direction by setting Ψ to be a function of x. Let us now state that for $y = 0$ the electric field envelope shall be $\Psi(x - \tilde{v}t)$. Inverting Eq. 3.5 our electric field can be written as:

$$E(x, y, t) = e^{i(k_0 x - \omega_0 t)} \int \mathrm{d}k_x \tilde{\Psi}(k_x - k_0) e^{i[k_y(k_x)y + (k_x - k_0)(x - t\tilde{v})]} \tag{3.13}$$

where it is now k_y which is dependent on k_x. For $y = 0$ Eq. (3.13) returns the exact profile given by $\Psi(x - \tilde{v}t)$. For $y = c_2$ (where c_2 is a constant), the profile still depends only on $x - \tilde{v}t$, and therefore we can write

$$E(x, y, t) = e^{i(k_0 x - \omega_0 t)} F(y, x - \tilde{v}t), \tag{3.14}$$

where F is itself dependent on ω_0 and $\tilde{v}$ and $\Psi(x) = F(0, x)$.

3.3 IMPLEMENTATION IN 2D PIC

Our goal is to study the interaction between these pulses and matter in regimes where kinetic effects are important, such as plasma-based acceleration and light source, to name a few. This physics can only be properly simulated by fully kinetic codes, from which particle-in-cell codes are a efficient implementation. We start with a description of the implementation of these pulses into the two-dimensional PIC code OSIRIS. In this geometry (2D), only two spatial dimensions are simulated, but momenta and fields are still calculated in all three dimensions.

We defined the plane waves that could be part of the pulse and we can use Eq. (3.9) to build the electromagnetic field along the polarization direction. One still needs to calculate the remaining electric and magnetic field components, using Maxwell's equations in vacuum.

Let us start with a polarization outside of the plane (in z), which means that the electric field in Eq. (3.9) is E_z. We will assume that E_z is composed only of a single plane waves, since we know that we have to combine multiple plane waves to get a certain shape. We assume that $E_y = 0$ and $B_z = 0$ (to satisfy Maxell's Equations).

By using $\nabla \cdot \mathbf{E} = \mathbf{k} \cdot \mathbf{E} = 0$ we get that $E_x = 0$, meaning there are no other electric field components. From $\nabla \cdot \mathbf{B} = \mathbf{k} \cdot \mathbf{B} = 0$ we find:

$$k_y B_y + k_x B_x = 0 \tag{3.15}$$

and from $\nabla \times \mathbf{E} = -\partial \mathbf{B}/\partial t$ (using normalized units where $c = 1$) we can derive

both components of the magnetic field.

$$\begin{aligned} B_y &= +\frac{k_x}{\omega} E_z \\ B_x &= -\frac{k_y}{\omega} E_z \end{aligned} \tag{3.16}$$

This assures that both electric and magnetic fields respect Maxwell's equations in vacuum at $t = 0$, while the PIC algorithm assures they will respect Maxwell's equations at later times.

If the polarization is inside the plane (in y), we now assume $E_z = 0$ and $B_y = 0$. By using $\mathbf{k} \cdot \mathbf{E} = 0$ we get

$$E_x = -\frac{k_y}{k_x} E_y \tag{3.17}$$

We note that when the electric field is polarized inside the plane there is a longitudinal contribution $E_x \neq 0$, which comes solely from transverse wavevector components that are not along x, and therefore should not be confused with an electrostatic mode (which is not). Using $\mathbf{k} \times \mathbf{E} = \omega \mathbf{B}$ we obtain

$$\begin{aligned} -k_y E_x + k_x E_y &= \omega B_z \Leftrightarrow \\ \Leftrightarrow B_z &= \frac{E_y}{\omega}(k_x + k_y^2/k_x) \end{aligned} \tag{3.18}$$

From $\mathbf{k} \times \mathbf{B} = 0$ one takes that $B_x = 0$.

3.3.1 Energy Flow

We described how to design a pulse where the focus travels at any speed, but at the same time the flow of energy cannot go faster than light, according to relativity. In Fig. 3.1a) we can see a spatiotemporal pulse where a longitudinal profile at $y = 0$ was imposed (meaning that the function Ψ depended on k_x). In Fig. 3.1b we show a spatiotemporal pulse where a transverse profile was imposed at $y = 0$. We observe that these pulses are composed of the focus, which has the largest intensities, and off-axis wings, which are the non-focused part of the pulse. In the pulses that are faster than the speed of light, the wings in front of the focus are focusing, ensuring that the group speed of the envelope is faster than the speed of light. On the contrary, in the subluminal foci, the wings on the back of the focus are focusing. To prove this statement, we plot the Poynting vector ($\mathbf{S} = \mathbf{E} \times \mathbf{B}$) for one superluminal (Fig.3.2a) and one subluminal (Fig.3.2b) pulse. The Poynting vector indicates the flow of electromagnetic energy: in the superluminal case, the energy at the front of the focus is traveling towards the axis (focusing) whereas the back of the focus is traveling away from the axis (defocusing). The contrary is seen for the subluminal pulse. The flux of energy still travels at the speed of light, but this focusing/defocusing effect gives the illusion that the focus is itself a real entity that travels at a speed different from c.

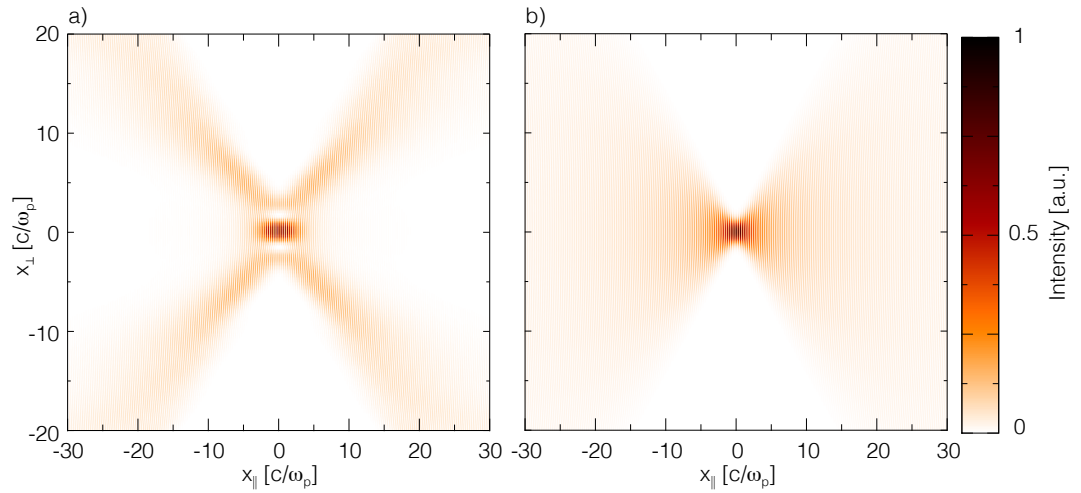

FIGURE 3.1: Intensity for a laser pulse traveling at $\tilde{v} = 1.05c$: a) Pulse with an imposed longitudinal envelope profile of $E_y = a_0 \exp(-x^2/\sigma_x^2)$ for $x_y = 0$ and b) Pulse with an imposed transverse profile of $E_y = a_0 \exp(-y^2/W_0^2)$.

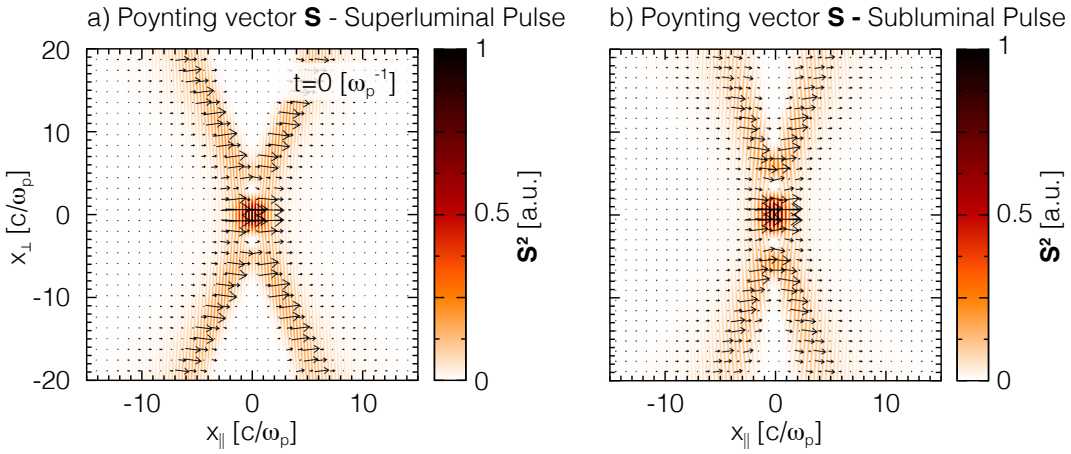

FIGURE 3.2: Poynting vector and its magnitude both for a) superluminal ($\tilde{v} = 1.05c$) and b) subluminal ($\tilde{v} = 0.95c$) pulses with an imposed longitudinal envelope profile.

3.3.2 OFF-AXIS WINGS

On both Figures 3.1 a-b we observe that a lot of electromagnetic energy is away from the propagation axis. One can show that these off-axis wings of the pulse are an intrinsic property of these pulses. Let us suppose that a focus is superluminal and at a certain time t_0 the focus is at x_0. At some other time $t_1 > t_0$ the focus is at $x_1 = x_0 + (t_1 - t_0)\tilde{v}$. The photons that composed the focus at $t = t_0$ cannot be the same photons that are part of the focus at $t = t_1$, because photons travel at c. Thus,

the photons have to be travelling with transverse momentum. The higher the $|\tilde{v} - c|$, the larger is the transverse momentum required.

The shape invariance of these pulses cannot hold for all times. In that case the amount of electromagnetic energy in the pulse is infinite. One of the properties that is of interest is the time (or length) along which we can assure the shape is invariant. Since the most the photons could have traveled in the x direction is if they were traveling along x (with no transverse component), identifying $x_{ph,1}(t)$ as the position of the photon that is part of the focus at t_1 at time t, we can write:

$$\begin{aligned} x_1 &< x_{ph,1}(t_0) + (t_1 - t_0)c \Leftrightarrow \\ \Leftrightarrow x_{ph,1}(t_0) &> x_0 + (t_1 - t_0)(\tilde{v} - c) \end{aligned} \tag{3.19}$$

In these pulses, it is important to distinguish the duration of the focus from the total pulse duration. In a gaussian pulse, the duration of the focus is the duration of the pulse, since there are no off-axis wings. However, in space-time wave packets, the duration of the pulse is completely disconnected from the duration of the focus. Hence, to have a pulse that travels at a certain speed $\tilde{v}$ over a certain propagation range Δx, it is necessary for the total duration of the pulse Δt to obey:

$$\Delta t > |\Delta x(\tilde{v} - c)| \tag{3.20}$$

This result allows us to associate a time duration of the pulse itself to the focal range that it might have. With this result we can stray away from infinite pulses with infinite energy that the theory assumes and get correct scalings. Equation (3.20) also means that the energy in the pulse grows linearly with duration. We observe that to maintain the envelope shape, every temporal slice of the beam must carry the same amount of energy. Therefore, both duration and energy increase linearly with the propagation range. By the same logic, energy increases with $(\tilde{v} - c)$. What Eq. (3.20) tells us is that the duration must be larger than the distance in the $x - ct$ reference.

3.3.3 The function Ψ

In Eq. (3.8) we said that the function Ψ could be arbitrary. In general, we can build any profile in one direction if we have every wavevector in that same direction, as we can Fourier expand any arbitrary profile $\Psi(x)$ such that

$$\Psi(x) = \int_{k_x=-\infty}^{\infty} \tilde{\Psi}(k_x) e^{-izk_x} \mathrm{d}k_x \tag{3.21}$$

However, the range of wavevectors for spatiotemporal pulses is sometimes finite. The case of $\tilde{v} = c$ exemplifies this. Immediately one sees that $k_y = 0$, for all k_x. Therefore, the pulse envelope function cannot depend on y (the conjugate of k_y) and

thus it is impossible to set the transverse envelope profile and one cannot impose any transverse profile. Generally speaking, the effects are not that extreme when $\tilde{v} \neq c$, but they still affect how the pulses might look when setting a longitudinal profile. Ultimately these constraints on Ψ arise because any electromagnetic plane wave frequency and wave vector need to be on top of the cone defined by Eq. (3.1), i.e. $\boldsymbol{k}$ and ω are related to each other through the dispersion relation.

For example, we can only set $k_x > k_0$ for superluminal pulses. However, if we take the Fourier Transform of a Gaussian function times an oscillation at k_0 you also get wavevectors $k_x < k_0$. This means that you cannot exactly reconstruct that profile, only the part that is larger than k_0. This is shown in Fig. 3.3.

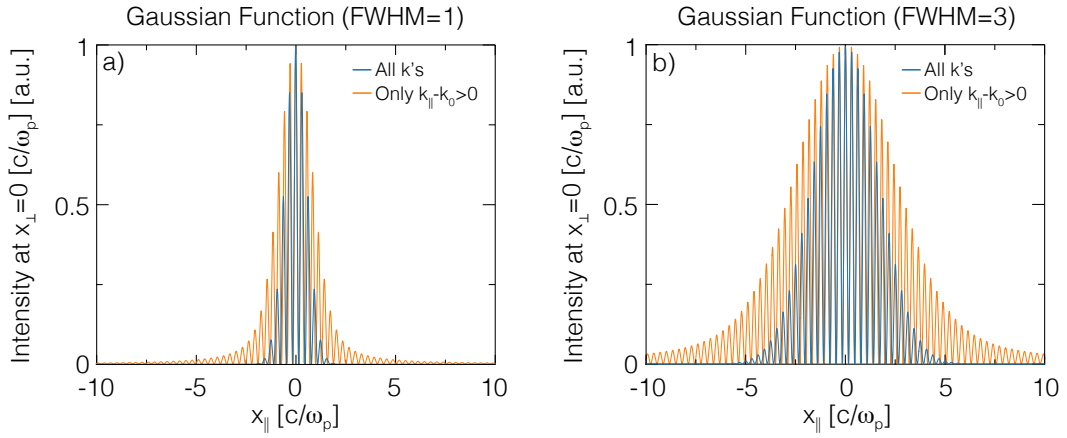

FIGURE 3.3: Effect of only using certain wavevectors on the longitudinal intensity profile at focus. Square of the Gaussian function where in blue we use all wavevectors and in orange where only $k_x - k_0 > 0$ for a) FWHM=1 [c/ω_p] and b) FWHM=3 [c/ω_p].

From Eq. (3.8) we observe that the Fourier transform was taken in the longitudinal direction, meaning that we had control over the shape of the pulse in the longitudinal axis [from which we get $\Psi(k_x)$]. It is clear from the previous analysis that if both the group velocity $\tilde{v}$ and the temporal profile on-axis are chosen, the transverse profile is immediately set. However, it is possible to perform the same analysis by controlling the transverse shape [thus using $\Psi(k_y)$] and thus letting the temporal profile be set externally.

The simplest case for the profile is a Gaussian profile. By setting a temporal Gaussian profile the transverse profile at focus is shown in Fig. 3.4a) for several temporal FWHM of the pulse. As we plot the lineout of the pulse in Fig. 3.4, one can see that they compare very well to the orange plots in Fig. 3.3 (both look like Gaussians but have much larger tails), as we lack part of the wave vectors necessary to build a full Gaussian profile. We observe that the pulse is transversely localized (Fig. 3.4c) with a sinc-like shape. When setting the transverse profile to a Gaussian, however, the

limited range of k_x means it is more complicated to contain, as seen in Fig. 3.5.

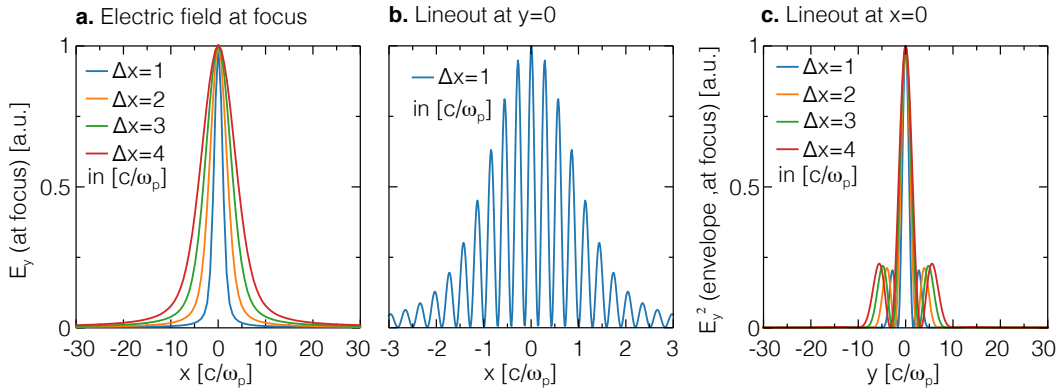

FIGURE 3.4: Electric field of spatiotemporal pulses with $\tilde{v} = 1.05c$ and $\omega_0 = 10\ [\omega_p]$, where a longitudinal envelope profile at focus of $E = \exp(-x^2/\sigma_x^2)$ was imposed, where σ_x/c is the duration. a) Imposed longitudinal profile at the focus. b) Electric field along the longitudinal direction for $\sigma_x = 1\ [c/\omega_p^{-1}]$. c) Envelope of the electric field squared along the transverse direction for four different temporal profiles.

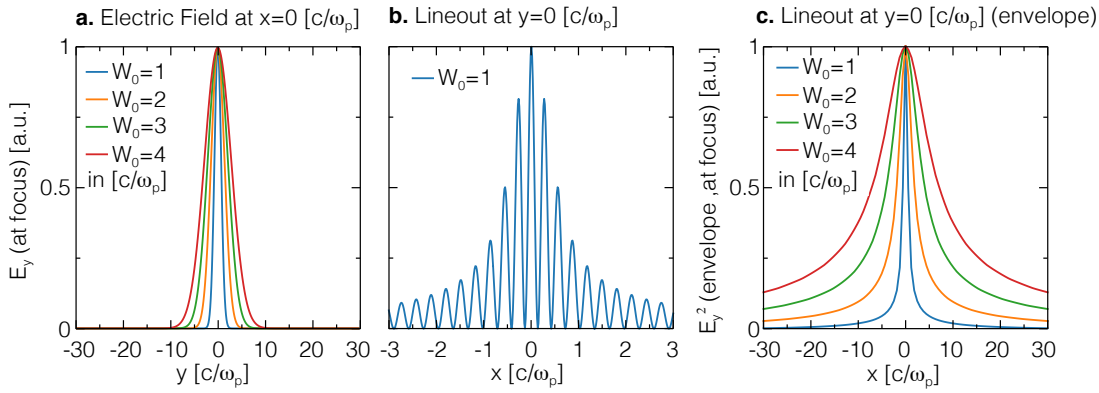

FIGURE 3.5: Electric field of spatiotemporal pulses with $\tilde{v} = 1.05c$ and $\omega_0 = 10\ [\omega_p]$, where a transverse profile at focus of $E = \exp(-y^2/W_0^2)$ was imposed, where W_0 is the spotsize. a) Imposed transverse profile at the focus. b) Electric field along the longitudinal direction for $W_0 = 1\ [c/\omega_p]$. c) Envelope of the electric field squared along the longitudinal direction for four different transverse profiles.

3.3.4 DESIGNING EXACTLY LONGITUDINALLY GAUSSIAN PROFILES

Let us assume that we want to create a true longitudinal Gaussian pulse with a certain wave vector k_{osc}. Until now, we assumed that k_0 is the oscillation frequency in the longitudinal direction, which leads us to assume $k_{osc} = k_0$. However, we saw that

$k_x > k_0$ always holds for superluminal pulses, which prevents a Gaussian pulse with an oscillation frequency $k_{osc} = k_0$, because gaussian pulses require both $k_x - k_{osc} > 0$ and $k_x - k_{osc} < 0$ (shown in Fig. 3.3). However, if we want the oscillation frequency to be $k_{osc} > k_0$, we can define our envelope function to be an oscillation at $k - k_0$. If we now take the Fourier Transform of the envelope profile $\tilde{\Psi}(k_x - k_0)$ in Eq. (3.13) and multiply by $e^{ix(k_{osc}-k_0)}$, now there are available k_x such that $k_x > k_{osc}$ and $k_x < k_{osc}$, allowing for the generation of true Gaussian profiles, as seen in Fig. 3.6. This being true, the transverse profile will be changed as we increase the value of k_{osc}. This result suggests that k_0 is somewhat arbitrary, with some influence in the transverse profile.

The arbitrariness of k_0 is readily observed in Eq. 3.2, where this plane can be translated along the ω axis while still maintaining the group speed. We can use this freedom to construct an exactly longitudinally Gaussian envelope profile. In Fig. 3.6 we show how by separating k_0 from the oscillating frequency we are able to create longitudinal Gaussian profiles. In Fig. 3.6a we show the theoretical envelope and the real profile (which is just the envelope times a cosine of $10x$. In Fig. 3.6b-c we show the transverse profile of such a pulse. While we observe that for an oscillation at k_0 the pulse is elongated in the longitudinal direction, whereas now with an oscillation at $k \neq k_0$ we observe an elongation in the transverse direction. While in Fig. 3.4c almost all the pulse energy is concentrated around $y = 0$ $[c/\omega_p]$, in Fig. 3.6c we see that the pulse has more subpeaks.

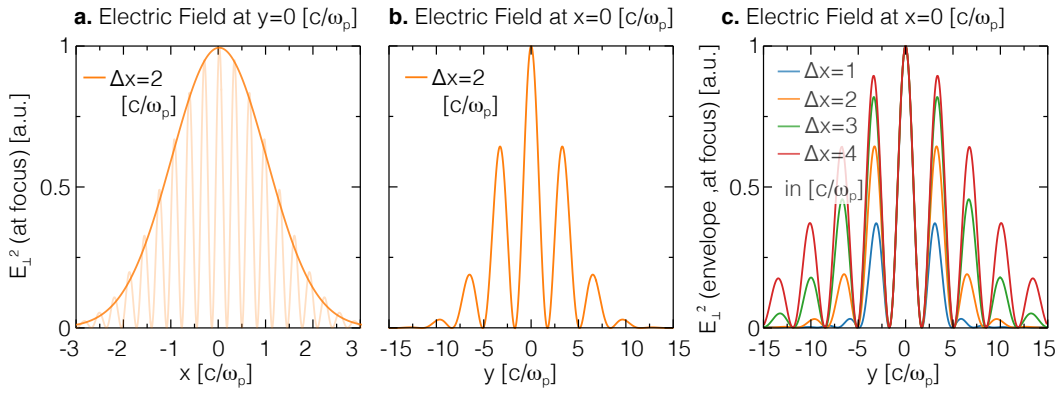

FIGURE 3.6: Electric field of spatiotemporal pulses with $\tilde{v} = 1.05c$ and $k_0 = 8$ $[\omega_p/c]$ and $\bar{k} = 10$ $[\omega_p/c]$, where a longitudinal profile at $y = 0$ of $E = \exp(-x^2/\Delta x^2)$ was imposed, where $\Delta x/c$ is the focus duration. a) Imposed longitudinal profile at the focus and comparison with theory ($\Delta x = 2$ $[c/\omega_p]$). b) Transverse profile of the pulse c) Envelope of the electric field squared along the transverse direction for four different longitudinal profiles.

3.3.5 Combining several space-time wave packets

Since the selection of k_0 seems arbitrary, one could think about combining several pulses with the same v_g but different k_0 (while keeping $\tilde{v}$), which allows to determine both the transverse and the longitudinal envelope. However, selecting a single k_0 forces $\partial\omega/\partial k_x$ to be constant, according to Eq. (3.2). When using different k_0, $\partial\omega/\partial k_x$ cannot be evaluated to a single value. When several pulses are imposed, the final result is that the whole structure does not travel at the predetermined speed, but it partly emerges from a background, as shown in Fig. 3.7. We observe that space time wave packets are constantly balancing three properties: transverse dimension, longitudinal dimension and contrast against the background. We saw that using a single k_0 can give a good contrast (meaning there is no background from which the focus emerge) but at the expense of large pulse dimensions. Adding more pulses helps constraining the dimensions but the focus is not well defined.

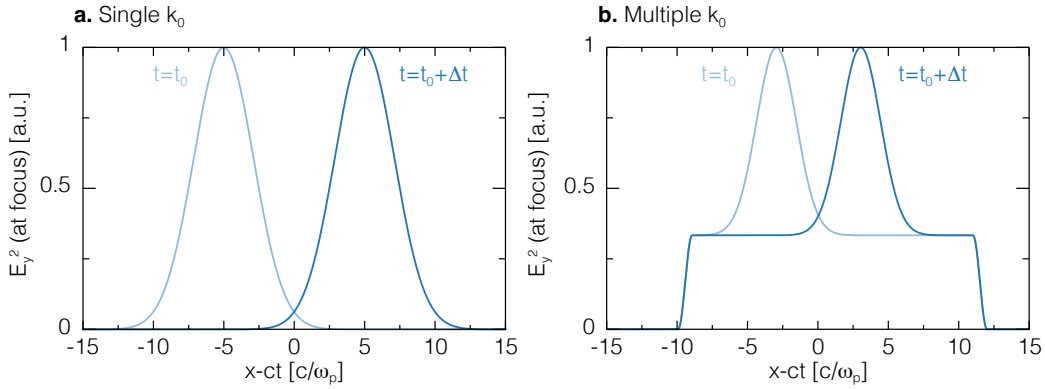

FIGURE 3.7: Different contrasts when adding different k_0. a) Pulse at $t = t_0$ (light blue) and at $t = t_0 + \Delta t$ (dark blue) for a longitudinal gaussian envelope for a pulse with a single k_0. b) Pulse at $t = t_0$ (light blue) and at $t = t_0 + \Delta t$ (dark blue) for a longitudinal Gaussian envelope composed with multiple k_0.

3.4 Physical picture

As we have seen, the work from Kondakci develops the concept of space-time wave packets with an integration over all possible modes (k_x, k_y, ω). To properly get the physical understanding of these pulses, one can look at the beat-wave that results from the superposition of only 4 modes with different frequencies/wavenumbers allowed by the pulse bandwidth.

Let us consider the following mode superposition

$$\begin{aligned} E(z,t) \propto \quad & \cos \quad [k_y x_y + (k_0 + \Omega/\tilde{v})x_x) - (\omega_0 + \Omega)t] + \\ & \cos \quad [k_y x_y + (k_0 - \Omega/\tilde{v})x_x) - (\omega_0 - \Omega)t] + \\ & \cos \quad [-k_y x_y + (k_0 + \Omega/\tilde{v})x_x) - (\omega_0 + \Omega)t] + \\ & \cos \quad [-k_y x_y + (k_0 - \Omega/\tilde{v})x_x) - (\omega_0 - \Omega)t], \end{aligned} \tag{3.22}$$

where x_y refers to the transverse coordinate, x_x to the longitudinal coordinate, and (ω_0,k_0) to the central frequency/wavenumber pair of the electric field. The variable Ω is introduced as a change to the central frequency (hence the increased bandwidth) and $\tilde{v}$ is the pulse group velocity. In the work of Abouraddy, k_y depends on Ω, but we keep that dependence hidden for simplicity. The result above can be seen as a crude approximation of the integral presented in the same work:

$$\begin{aligned} E(z,t) &= \int \mathrm{d}\Omega \tilde{\Psi}(\Omega) \exp\{i[k_y x_y - \Omega(t - z/\tilde{v})] + ik_0 x_x - i\omega_0 t\} \\ &= \int \mathrm{d}\Omega \tilde{\Psi}(\Omega) \exp\{i[k_y x_y + x_x(k_0 + \Omega/\tilde{v}) - t(\omega_0 + \Omega)\}, \end{aligned} \tag{3.23}$$

where $\tilde{\Psi}(\Omega)$ is the Fourier transform of the pulse temporal envelope at $t = 0$, and where

$$k_y = \pm \frac{1}{c}\sqrt{2\omega_0\Omega(1 - c/\tilde{v})}. \tag{3.24}$$

Using standard trigonometric identities, it follows from Eq. (3.22) that:

$$\begin{aligned} E(z,t) \quad \propto \quad & \cos[k_y x_y] \cos[(k_0 + \Omega/\tilde{v})x_x) - (\omega_0 + \Omega)t] + \\ + \quad & \cos[k_y x_y] \cos[(k_0 - \Omega/\tilde{v})x_x) - (\omega_0 - \Omega)t] = \\ = \quad & \cos[k_y x_y] \left\{ \cos\left[\left(k_0 + \frac{\Omega}{\tilde{v}}\right) x_x - (\omega_0 + \Omega)t\right] + \cos\left[\left(k_0 - \frac{\Omega}{\tilde{v}}\right) x_x - (\omega_0 - \Omega)t\right] \right\} \\ = \quad & \cos[k_y x_y] \cos[k_0 x_x - \omega_0 t] \cos\left[\frac{\Omega}{\tilde{v}} x_x - \Omega t\right] \end{aligned} \tag{3.25}$$

In Eq. (3.25), it is possible to see the different roles of the three cosines:

1. $\cos[k_y x_y]$ plays the role of the transverse laser profile
2. $\cos[k_0 z - \omega_0 t]$ is the fast varying phase
3. $\cos\left[\frac{\Omega}{\tilde{v}} - \Omega t\right]$ plays the role of the longitudinal pulse profile envelope

One finds that the group velocity of the pulse must come from the phase velocity of the envelope, which is simply given by

$$\tilde{v} = \frac{\Omega}{\Omega/\tilde{v}} = \tilde{v} \tag{3.26}$$

From the transverse profile, we see that the pulse must be centered at $x = 0$, as determined by $\cos[k_y x_y]$ is maximum at $x_y = 0$. To displace the pulse in a transverse direction by a certain offset x_{off}, one can immediately add a phase x_{off}/k_y. The freedom to adjust the transverse direction enables the centroid of the pulse to, for instance, execute a sinusoidal trajectory if the phase is dependent on z:

$$\cos[k_y(x_y + \phi(z))], \phi(x_x) = \alpha \sin(k_m x_x), \tag{3.27}$$

where α is an amplitude and k_m is the modulation wavenumber in the laser frame. In principle, any trajectory is obtainable from the additional phase ϕ. Note that the pulse profile is periodic in the transverse x direction, which is not the case for the original Abouraddy's work. This is a consequence of approximating the integral of Eq. (3.23) to only 4 points.

3.5 Implementation in OSIRIS

For the implementation in OSIRIS, we did the numerical integral of Eq. (3.8). As we noted before, the intersections between a cone and a plane can be multiple. When the intersection between the cone and the plane is an ellipsis or a circle, the bandwidth (possible frequencies ω) is finite, and therefore the user may only provide the number of points that they wish to use for the numerical integration. However, if the intersection is a parabola or a hyperbola, the bandwidth becomes infinite (in experiments the bandwidth is set by the initial pulse before being shaped into a space-time wave packet), and it is up to the user to select the maximum and minimum k for the integration. Therefore, the user should supply the number of integration points n_k, the group speed of the pulse $\tilde{v}$ (which may or may not set the total bandwidth), and the bandwidth that the user will integrate on.

The initialization of the pulse is done inside the box. The pulse will be a combination of several plane waves. Therefore, we start by taking the smallest available ω. From Eq. (3.2), one can get the k_x of the plane wave and from Eq. (3.5) one gets k_y. The code populates the grid with the plane wave and does this n_k times. As we showed in Eq. (3.16), it is necessary to calculate other electric and magnetic fields to ensure that the pulse obeys Maxwell's equations in vacuum.

The most important feature of these spatiotemporal pulses is the focal speed, which can be controlled, unlike regular pulses. In Fig.3.8a we see the initial laser pulse

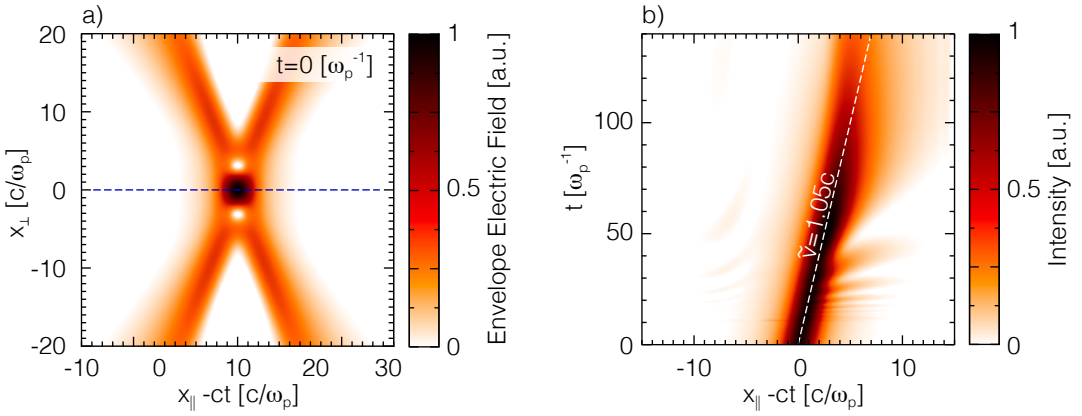

FIGURE 3.8: Evolution of a spatiotemporal pulse in vacuum. a) Spatiotemporal pulse with $\Delta t = 1\ [\omega_p^{-1}]$ and $\tilde{v} = 1.05c$. The lineout is taken at $y = 0\ [c/\omega_p]$. b) Waterfall plot of the pulse, taking a lineout of the pulse for every timestep and plotting it in every horizontal line. The white dashed line shows a regular propagation at $\tilde{v} = 1.05c$.

envelope that travels at 1.05c. For each time, one takes the lineout along $y = 0$, shown in the dashed blue line.

To validate our implementation, one of the most important things is to ensure that Maxwell's equations are respected at t_0. Both the divergence of the electric field and the divergence of the magnetic field for a 2D pulse are shown in Fig. 3.9. As we have seen before, if the polarization is out-of-plane the divergence of the electric field is automatically 0, as in two dimensions $\partial/\partial z = 0$ and both E_x and E_y are zero. The same argument holds for the divergence of the magnetic field in the polarization along y.

3.6 PROPAGATION PROPERTIES OF SPACE-TIME WAVE PACKETS

3.6.1 NON-DIFFRACTING

One of the clear properties of these pulses is that the envelope stays roughly constant within a certain propagation range that typically exceeds the Rayleigh length of an equivalent Gaussian pulse. It is important to remember that the total energy of the pulse scales linearly with the propagation distance, as seen with Eq. (3.20).

In Figure 3.10 it is clear that even though the focus has moved with a speed that is larger than the speed of light, the shape on-axis is still the same.

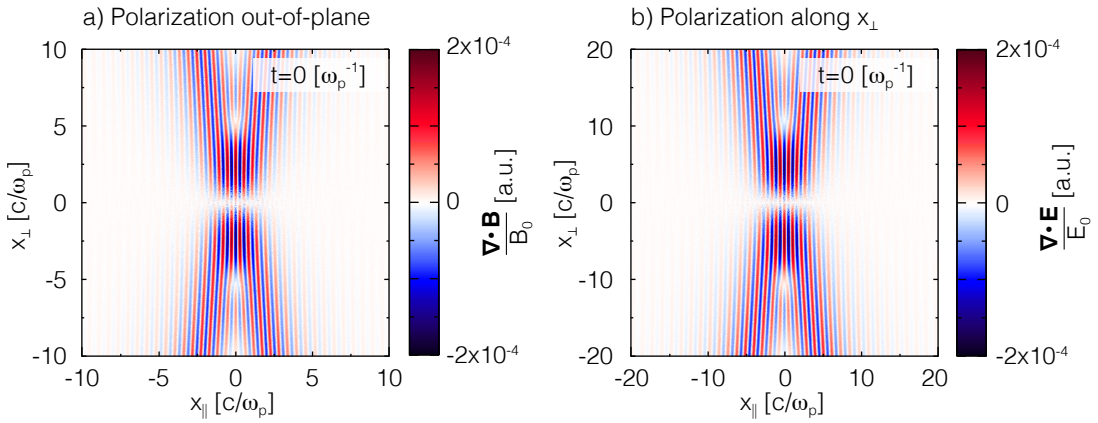

FIGURE 3.9: Validation of the OSIRIS implementation: a) Divergence of the magnetic field for an out-of-plane polarization (on z) and b) divergence of the electric field for a polarization along y. Both the divergence of the electric field for a) and the divergence of the magnetic field for b) are automatically satisfied.

3.6.2 SELF-HEALING

One of the interesting properties of the spatiotemporal pulses has to do with how the photons that are part of the focus at a certain propagation distance are not the photons that compose the focus at later times. Therefore, if we make the pulse interact with an overdense plasma, thereby stopping the propagation of the photons that compose the focus at some particular time, the focus will still reappear at a later time, which can be seen from Fig. 3.11. On panel a), we observe the spatiotemporal pulse and the position of a plasma sphere with a peak density of $2n_c$, where n_c is the critical frequency, meaning the laser cannot propagate through the plasma. After some time, on panel b) we see that the focus of the pulse is interacting directly with the plasma and one notices how the focus was destroyed, as the flux of energy was disrupted. We note that the plasma is still. However, in the $z - ct$ axis this means that it is traveling backward at the speed of light. On panel c), a long time after the interaction, we observe that the pulse focus has now recovered. There are however some differences. The first one concerns the fact that at the left of the focus, we see an interruption of the normal structure. This is because the electromagnetic fields that would be there (at the left of the focus) were reflected by the plasma at $t = 15\ c/\omega_p$. The part of the pulse that was the focus at $t = 15c/\omega_p$ gained transverse momentum as it deviated from the plasma. However, part of the pulse (with transverse $\mathbf{k}$) may have lost transverse momentum as it collided on the side of the plasma, rather than upfront. This resulted in some light traveling longitudinally around $z - ct = 2\ c/\omega_p$.

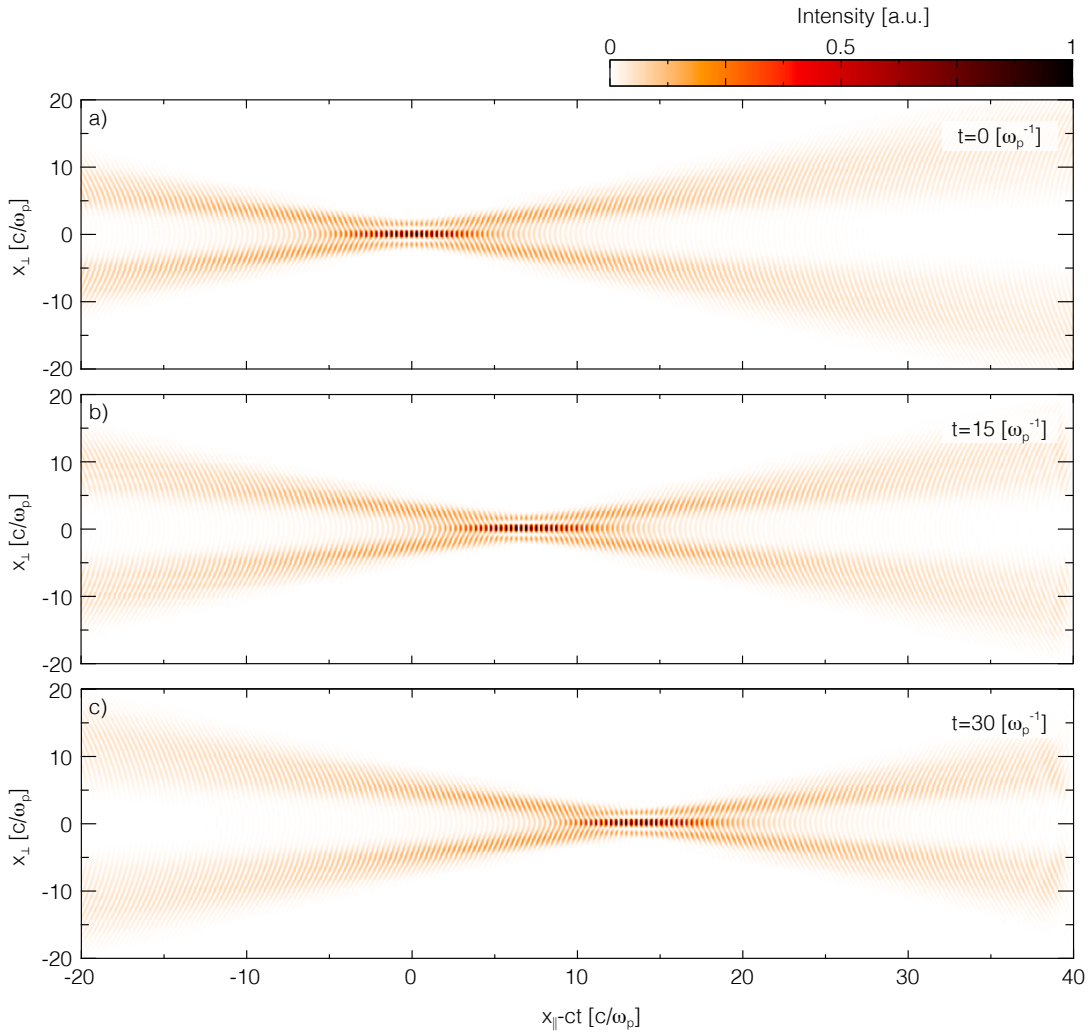

FIGURE 3.10: Spatiotemporal pulse traveling with $\tilde{v} = 1.5c$ while maintaining its shape. The pulse is shown in orange colors. a) Simulation at $t = 0$ $[c/\omega_p]$ b) Simulation at $t = 15$ $[c/\omega_p]]$ c) Simulation at $t = 30$ $[c/\omega_p]$

3.6.3 INJECTION AT AN ANGLE

To make the pulse travel inside the box at a particular angle it is only necessary to rotate the wavevector $\mathbf{k}$ by an angle θ. We note that the the cell dimensions Δx, Δy should be adjusted in the PIC simulation for proper propagation. Propagation of a pulse injected at 45 degrees can be seen in Fig. 3.12.

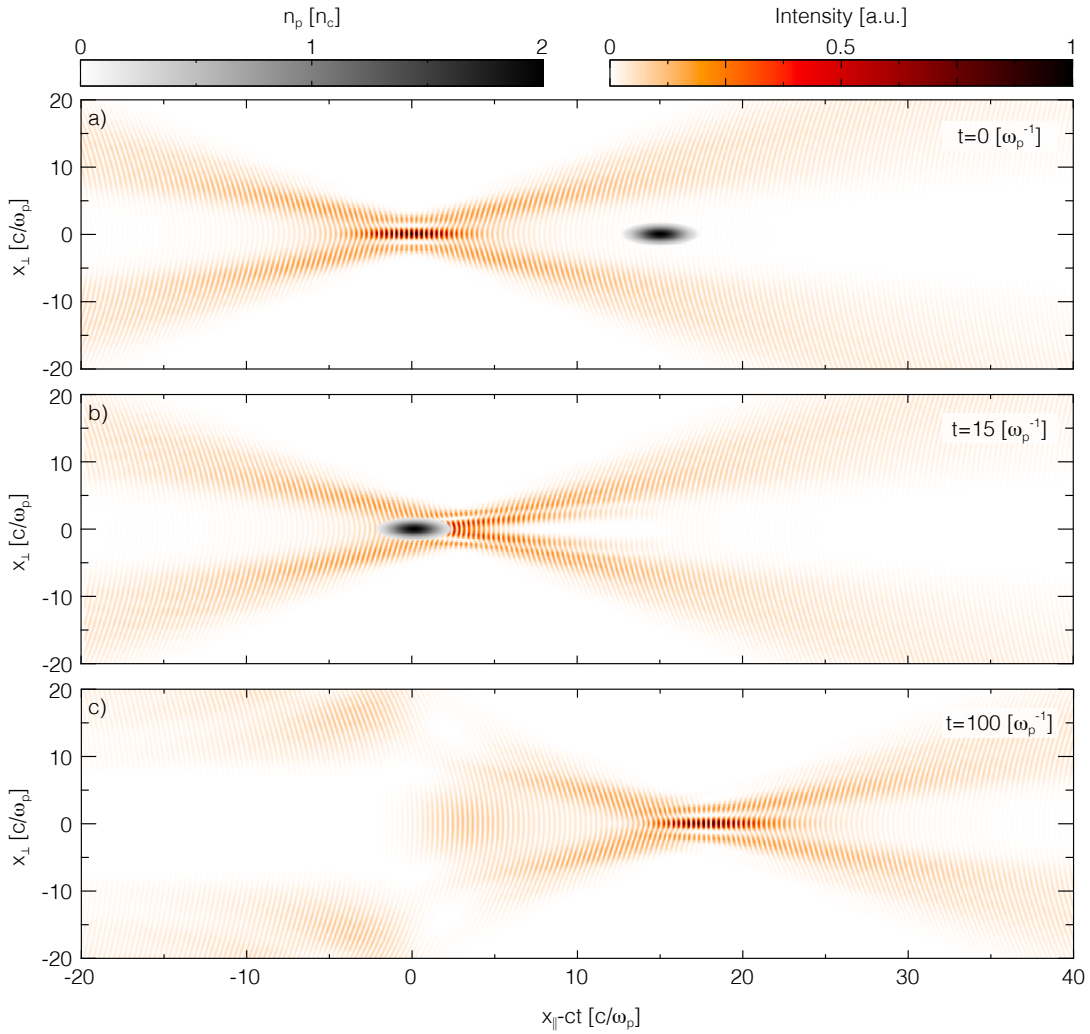

FIGURE 3.11: Spatiotemporal pulse traveling with $\tilde{v} = 1.2c$ self-healing after interaction with an overdense plasma. Plasma is shown in orange colors and plasma is shown in black and white. OSIRIS simulation a) at $t = 0$ $[c/\omega_p]$ b) at $t = 15$ $[c/\omega_p]]$ (during interaction between laser and plasma) and c) at $t = 100$ $[c/\omega_p]$ (after interaction)

3.6.4 TRANSVERSE OSCILLATION TRAJECTORY

To have a pulse oscillate transversely, one may use Eq. (3.27). However, indeed the pulse is no longer described by Eq. (3.23), as the phase modulation requires an extra integration variable that is related to the phase of every single plane wave that is in the system. This oscillation can be seen in Fig. 3.13.

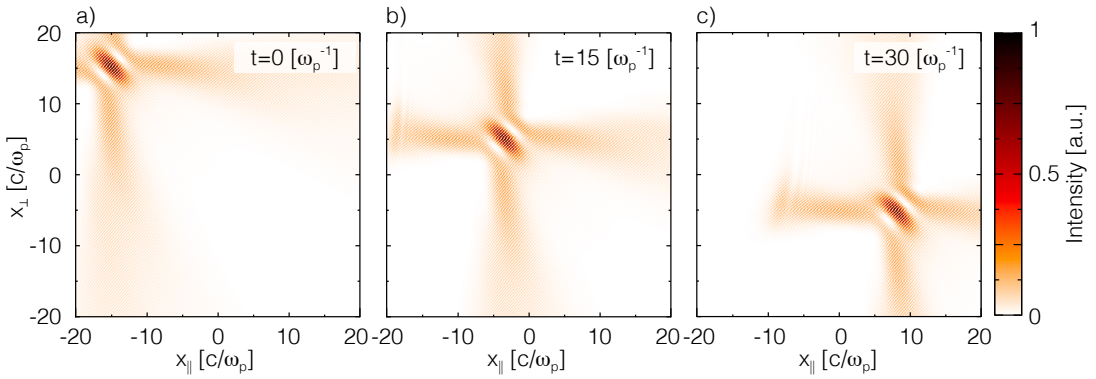

FIGURE 3.12: Spatiotemporal pulse traveling with $\tilde{v} = 1.1c$ and injected at an angle $\theta = \pi/4$. OSIRIS simulation a) at $t = 0[\omega_p^{-1}]$ b) at $t = 15[\omega_p^{-1}]$ and c) at $t = 30[\omega_p^{-1}]$. Note that the longitudinal axis is not moving at c, contrary to the remaining simulations in this chapter.

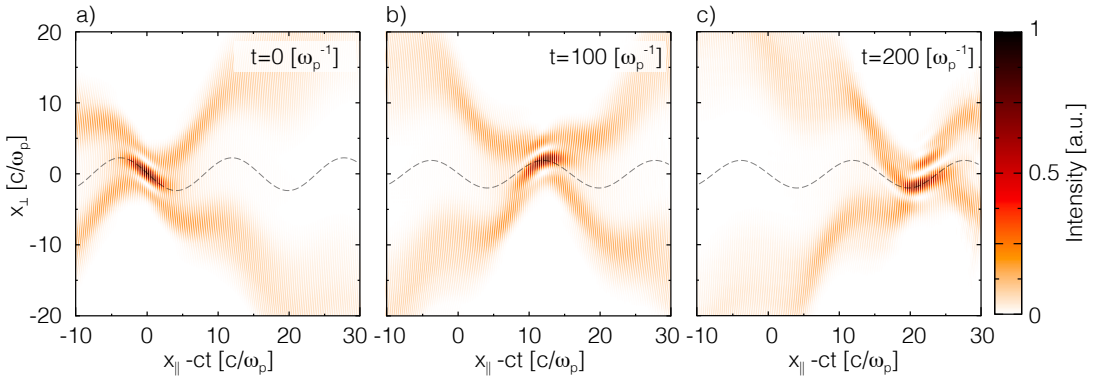

FIGURE 3.13: Spatiotemporal pulse traveling with $\tilde{v} = 1.1c$ and oscillating transversely during propagation with $\alpha = 2$ and $k_m = \pi/8$ (see Eq. (3.27)). The predicted trajectory for the center of the focus is in a dashed gray line. Simulation a) at $t = 0[\omega_p^{-1}]$ b) at $t = 100[\omega_p^{-1}]$ and c) at $t = 200[\omega_p^{-1}]$.

3.7 MOVING TO 3D

Up to now, all pulses were considered two-dimensional. There are multiple ways [87, 91, 92] of designing these pulses in a three-dimensional space. Here we considered pulses that are axisymmetric (both transverse components are the same). In 2D, we divided $\mathbf{k}$ into the parallel and transverse components k_x and k_y, respectively. Equation (3.1) now reads

$$k_x^2 + k_y^2 + k_z^2 = (\omega/c)^2. \tag{3.28}$$

This is now the equation of a four-dimensional cone. However, we must recall Eq. (3.5) and notice that Eq. (3.2) does not depend on k_y. Therefore, we can easily return

to the two-dimensional case by stating

$$\sqrt{k_y^2 + k_z^2} = k_y^{(2D)}, \tag{3.29}$$

where $k_y^{(2D)}$ is the transverse component in the 2D case, from which we already know the solution for via Eq. (3.5). To build the 3D pulse we must integrate in the three dimensions, but the transverse components are integrable using polar coordinates $(k_y^{(2D)}, \theta) = (k_y^2 + k_z^2, \arctan(k_y/k_z))$, and therefore we can rewrite Eq. (3.9) in 3D as:

$$\begin{aligned} E(x,z,t) &= e^{i(k_0 x - \omega_0 t)} \int \mathrm{d}k_y^{(2D)} \int \sin\theta \mathrm{d}\theta \tilde{\Psi}(k_y^{(2D)}) e^{i(k_y[sin(\theta)y + \cos(\theta)z] + [k_x - k_0][z - ct\tilde{v}])} \\ E(x,z,t) &= e^{i(k_0 x - \omega_0 t)} \Psi(\sqrt{y^2 + z^2}, x - \tilde{v}t), \end{aligned} \tag{3.30}$$

where it is clear that the pulse must be axisymmetric as the Ψ function may only depend on the distance to the longitudinal axis. To calculate the numerical integral we split the integral on the angle θ which is equivalent to injecting several 2D-like pulses at different k_y. We show how this integral gives rise to a full 3D pulse in Fig. 3.14, where we start by showing a single 2D-like pulse in the 3D box and show how injecting more of those eventually creates an axisymmetric 3D pulse with the same characteristics of the 2D pulses. We find that injecting 32 pulses is already enough to create a 3D structure that behaves as a whole unit.

The idea behind this construction is the fact that if the 2D pulses work as intended, they can also exist in the 3D space by infinitely extending in the other dimension (which is the same as $k_{y,2}$ being 0). These 2D pulses will also travel with a certain velocity and be diffraction-free, so a sum of a lot of 2D pulses will have the same characteristics. We validated the approach by confirming they were non-diffracting and had the correct velocity, as we see in Fig. 3.15b-c.

3.8 Conclusions and Future Work

To understand the effects of spatiotemporal pulses in plasma, we implemented these pulses in OSIRIS. The main feature of the class of pulses we implemented is the possibility of selecting the group velocity along the longitudinal direction, enabling faster-than-light focus propagation. We were able to validate the implementation for both subluminal and superluminal foci, showing that these pulses are diffraction-free, can self-heal when disrupted, and follow certain trajectories. We also showed our original implementation of a 3D variation of the injection, which allows for the study of the interaction between these pulses and plasma, which will be done in the next chapter.

There have been several works surrounding these ideas so future work would always involve starting from a 3D implementation from first principles. It is also possible to have a combination of different ω_0 in the same pulse, which is equivalent

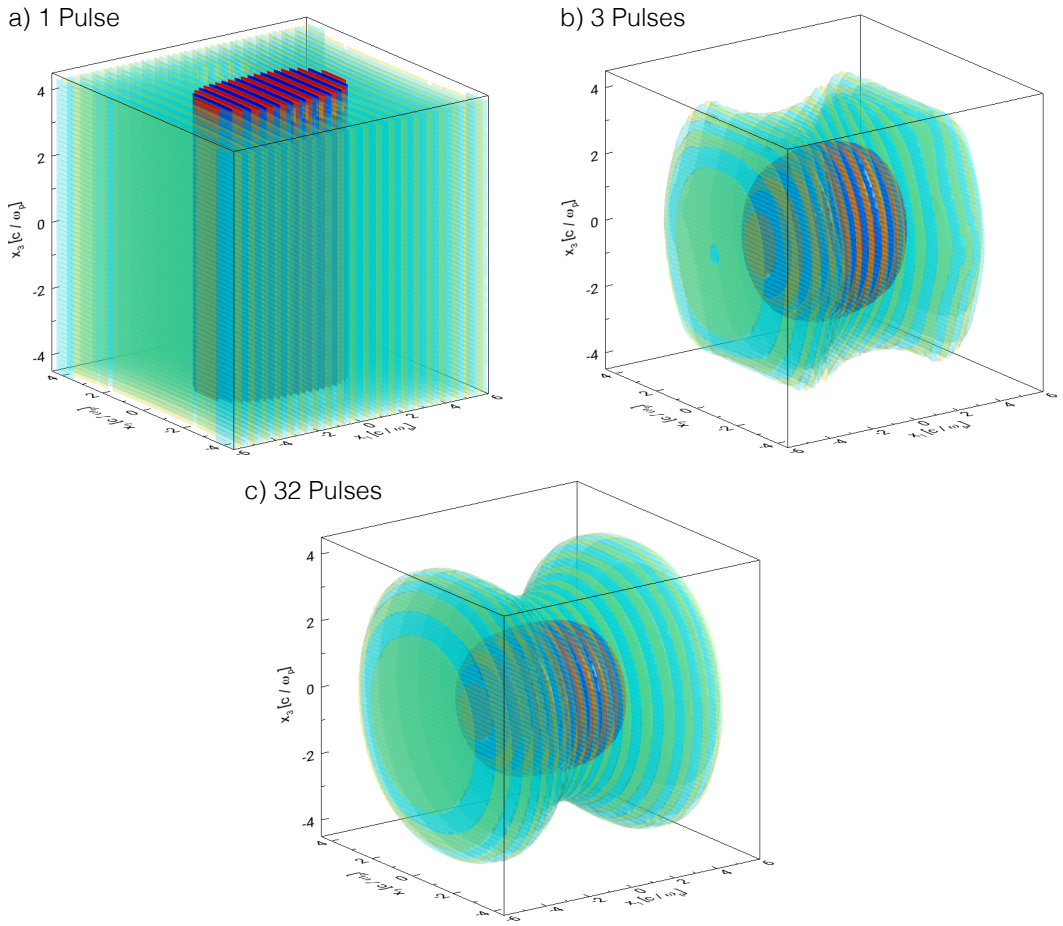

FIGURE 3.14: Creating 3D pulses from a superposition of 2D pulses around an axis. Red and blue show the most intense fields and yellow and green show less intense fields for a) 1 pulse b) 3 Pulses and c) 32 Pulses. It is clear that at 3 pulses we do not get a perfect symmetry, but for 32 the beam is symmetric and behaves as expected.

to having several planes intersecting the cone equation. This allows for setting both transverse and longitudinal profiles but at the cost of an increase in local bandwidth everywhere in the pulse.

These pulses may be extremely large, and since the computational time scales with the box size, it is imperative to use different injection techniques that enable using smaller boxes via injection from the walls (instead of just injecting in the whole simulation box).

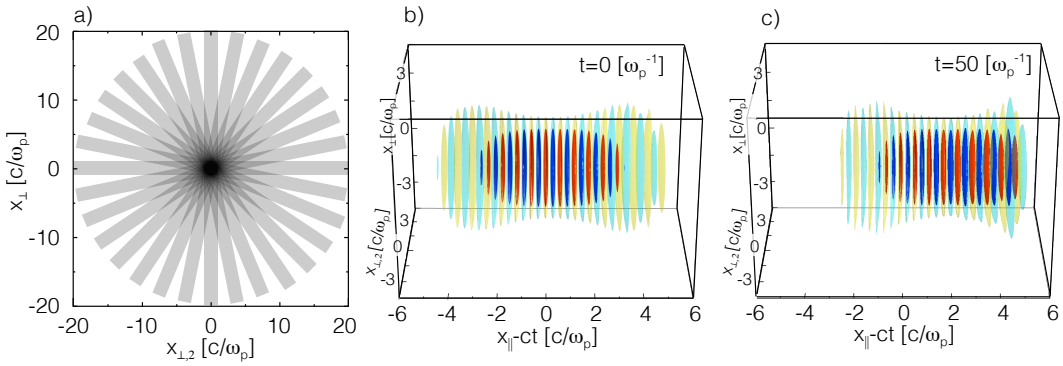

FIGURE 3.15: Three-dimensional spatiotemporal pulses: a) Combination of several 2D pulses to create a 3D pulse, 2D pulses in traveling with $\tilde{v} = 1.05c$. OSIRIS simulation of a three-dimensional pulse propagating in vacuum b) at $t = 0[\omega_p^{-1}]$ and c) at $t = 50[\omega_p^{-1}]]$.

3.9 Contributed Talks

B. Malaca, J.R.Pierce, M. Pardal, R.A.Fonseca W.B.Mori, J.P. Palastro, D. Froula,D. Ramsey, J.Vieira, *Nonlinear laser-driven wakefields with arbitrary phase velocity*, 62^{nd} Annual Meeting of the APS Division of Plasma Physics, remote (November 2020)

B. Malaca, J.R.Pierce, M. Pardal, R.A.Fonseca W.B.Mori, J.P. Palastro, D. Froula,D. Ramsey, J.Vieira, *Self-consistent laser-plasma interactions using structured lasers with arbitrary group velocity*, 47^{th} Annual Meeting of the EPS Division of Plasma Physics, remote (June 2021)

3.10 Papers in refereed journals

D. Ramsey, A. Di Piazza, M. Formanek, P. Franke, D.H. Froula, B. Malaca, W. B. Mori, J. R. Pierce, T. T. Simpson, J. Vieira, M. Vranic, K. Weichman, and J.P. Palastro, *Exact solutions for the electromagnetic fields of a flying focus*, Physics Review A, **107**, 1-013513 (2023) https://link.aps.org/doi/10.1103/PhysRevA.107.013513

Jacob R. Pierce and John P. Palastro and Fei Li and Bernardo Malaca and Dillon Ramsey and Jorge Vieira and Kate Weichman and Warren B Mori; Arbitrarily structured laser pulses; Physical Review Research **5** (1): 013085 (2023). https://doi.org/10.1103/PhysRevResearch.5.013085

CHAPTER 4

APPLICATIONS OF SPACE-TIME WAVE PACKETS

4.1 INTRODUCTION

The impact of space-time wave packets on science is still in the early stages, but has already led to an explosion of research activities devoted to understand how these pulses could be used for a multitude of concepts, such as plasma wave shaping, acceleration of heavier particles, and others. Chapter 2 showed that controlling the shape and trajectory of plasma waves may be useful for radiation production. Even though there has been put considerable effort in creating such pulses, they have not been generated at high power. To guide future experiments, simulations must indicate what are the possible paths forward for future high-power space-time wave packets. Until technology is able to generate high-power pulses, low-power applications of these pulses are an open field that needs to be explored, and it could fund the extra development needed for high-power applications. We will investigate this path in Chapter 5.

The goal of this chapter is to illustrate some applications of these space-time wave packets, including plasma acceleration and radiation production. Even though it is possible to simulate these pulses (as in Chapter 3), it is often very computationally expensive to simulate them in 3D and for propagation distances that could be interesting for experiments. Simulations of these pulses sometimes need to use simplified models that can capture the most relevant effects of these pulses on plasma. This chapter mainly consists of simulations results using reduced dimensionalities (1D or 2D).

The chapter is organized as follows: In subsection 4.2 we inspect the plasma

waves generated by these pulses and how they can be used for acceleration. In subsection 4.3 we research how these pulses can be used for radiation production, both with direct laser-particle interaction and via quasiparticle generation.

4.2 SPACE-TIME WAVE PACKETS AS DRIVERS OF PLASMA WAVES

In Chapter 2 we defined a quasiparticle as a localized current profile that travels in space and time. In section 1.2, we reminded that in typical laser wakefield acceleration the laser generates a blowout. This blowout is characterized by a very localized current profile quasiparticles that travel with the group speed of a laser in plasma, which in the linear regime is given by $v_g = \sqrt{1 - \frac{\omega_p^2}{\omega_0^2}}$. In Chapter 2, to have the quasiparticle move at superluminal speeds and emit coherent radiation, a special density profile had to be designed such that the quasiparticle created by the laser could travel superluminally.

Space-time wave packets, on the other hand, can travel at predetermined velocities, which may excite plasma waves moving at those speeds, and therefore avoid using special density profiles altogether.

To understand the plasma response to these pulses, we first designed 1D simulations to see the properties of the plasma waves excited by a laser, using a very similar setup to any LWFA experiment. Spatiotemporal lasers, as we showed in Chapter 3, have transverse wavevectors, which cannot be adequately simulated in 1D simulations. Therefore, to simulate such a pulse, we created a transverse electric field given by

$$E(z,t) = \omega_0 a_0 f(z - \beta_p t)\sin(kz - \omega_0 t), \tag{4.1}$$

where ω_0 is the laser frequency, a_0 is the laser normalized vector potential, β_p is the laser group velocity, $z \equiv x_{\parallel}$ and t is propagation time.

We prepared two simulations, using $\beta_p = 1.01$ (superluminal(and $\beta_p = 0.99$ (subluminal), at $a_0 = 15$, meaning the wave the laser generates is extremely nonlinear. The results are shown in Fig. 4.1. On both top panels a) and b) we show the pulse envelope in black and the electric field of the plasma wave in green. It is clear that the plasma wave stems from the laser pulse in both cases, even though the maximum amplitude is larger for the superluminal case. This fact is enough to prove that the plasma response travels at the same speed as the laser envelope, meaning that one can excite superluminal plasma waves.

Even though one-dimensional simulations and simplified models help us understand the phenomenon, it is only when full 3D models are used that we can be sure that these plasma waves can be excited. We designed very similar simulations to the 1D ones but in three dimensions. A plot of the spatiotemporal pulse flowing into

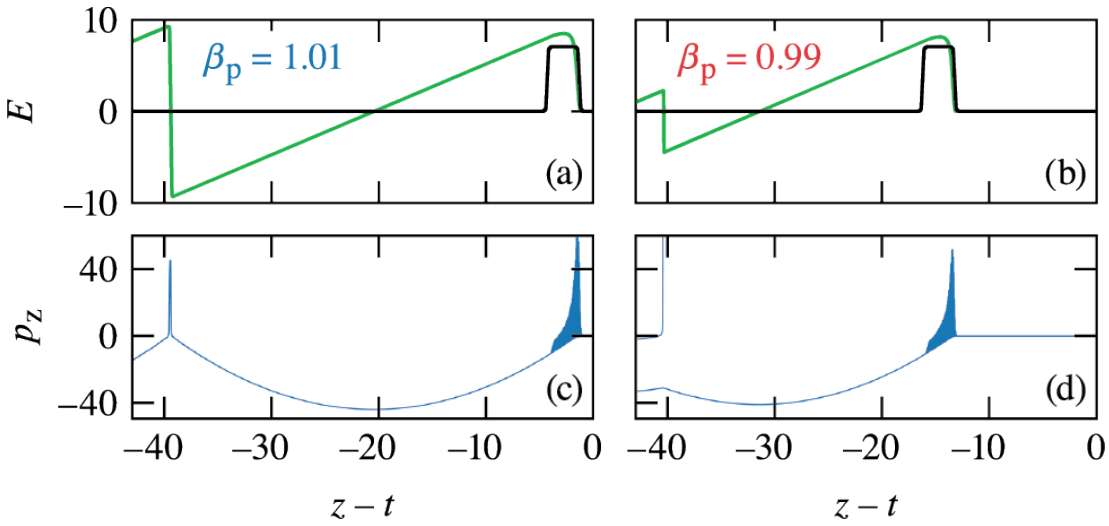

FIGURE 4.1: A comparison of the electric field of the wake and electron phase space for a superluminal, (a) and (c), and subluminal, (b) and (d), wake with $\beta_p = 1.01$ and $\beta_p = 0.9$), respectively. The phase velocities were chosen to make clear the distinction between the two cases. The driver intensity, shown in black for reference, has $a_0 = 15$ and a square pulse shape with duration $\tau = \pi$ for both cases. The superluminal wake maintains its structure and maximum electric field. Wave breaking of the subluminal wake leads to the injection and trapping of a large population of electrons, which load the wake, diminish its maximum field, and result in large energy spreads of any accelerated electron beam. Taken from [67]

plasma is found in Fig. 4.2. As we see from Fig.4.2a-c, the spatiotemporal focus travels superluminally, originating a plasma wave moving superluminally as well. There are however differences in the plasma wave originating from a spatiotemporal pulse with respect to a regular pulse driver, shown in Fig. 4.3. The most obvious difference is that in the conventional case some electrons entered the ion bubble and are accelerating, whereas no electron entered the ion bubble in the superluminal case. The differences that arise from both cases form enough ground to seek better understanding of the acceleration properties of these superluminal plasma waves.

4.2.1 LASER WAKEFIELD ACCELERATION WITH SUPERLUMINAL FOCI

The main difference that we observed from the conventional to the superluminal case - presence (or not) of self-accelerated electrons - is explained through wavebreaking. Wavebreaking occurs when accelerated electrons are able to overtake the phase speed of the driver and therefore are injected into the acceleration bubble. This takes place at large driver intensities. One of the limitations of laser wakefield accelerators is that the accelerated electrons start travelling faster than the laser field and will dephase with relation to the plasma wave, stopping the acceleration (the acceleration fields decrease

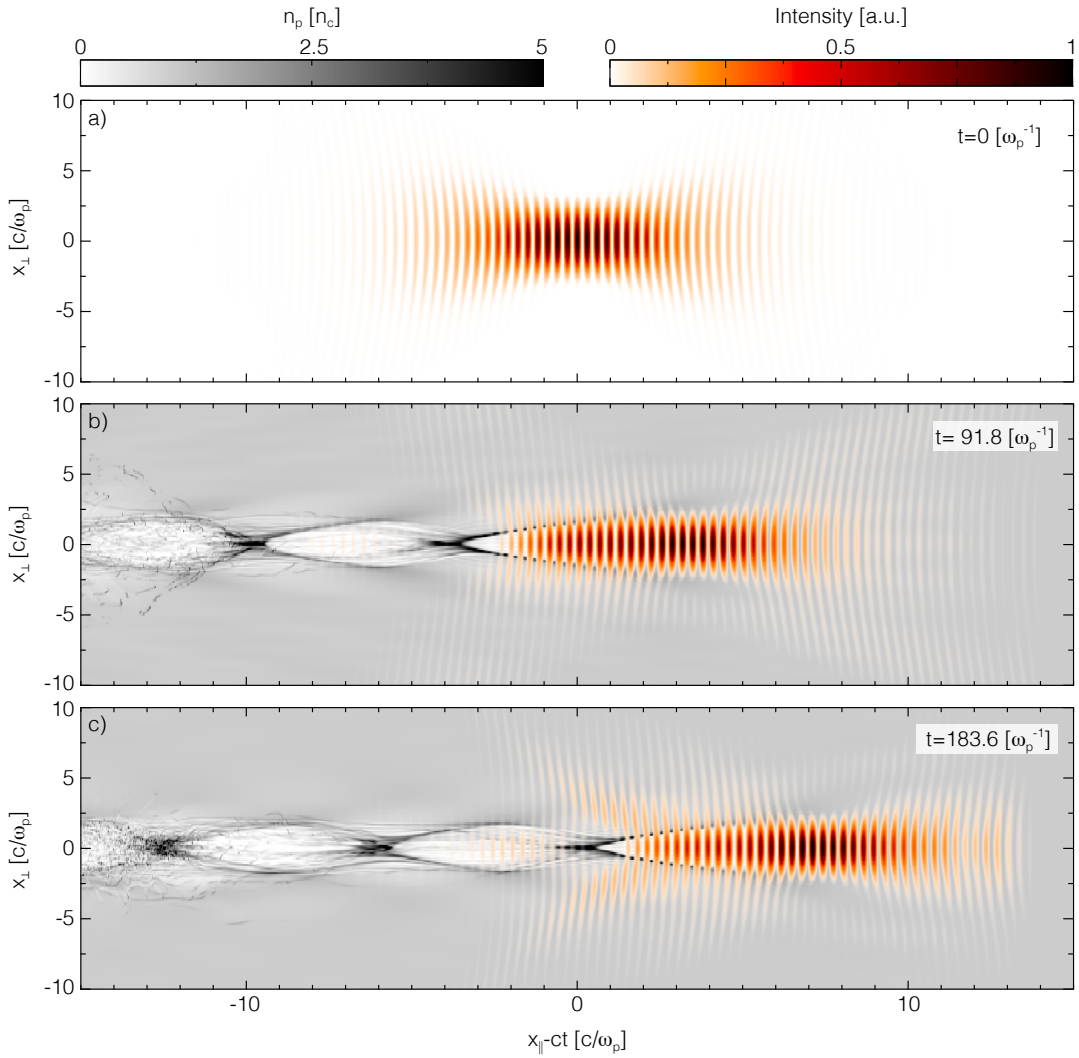

FIGURE 4.2: Spatiotemporal pulse interacting with plasma in 3D at a) $t = 0$ $[\omega_p^{-1}]$ b) $t = 91.8$ $[\omega_p^{-1}]$ and c) $t = 183.6$ $[\omega_p^{-1}]$. Speed of the pulse $v_g = 1.05c$, normalized vector potential $a_0 = 2.0$

as the electron beam travels through the ion bubble). As a large number of electrons are injected, they also tend to contaminate the original electron beam and reduce the accelerating fields.

On both Fig. 4.4c-d we can look at the plasma electrons phase-space, showing that the waves are very much alike, except for wave breaking occurring in the subluminal case.

It is clear that this acceleration cannot take forever, as the accelerated electrons will in this case be overtaken by the superluminal driver and be subject to both de-

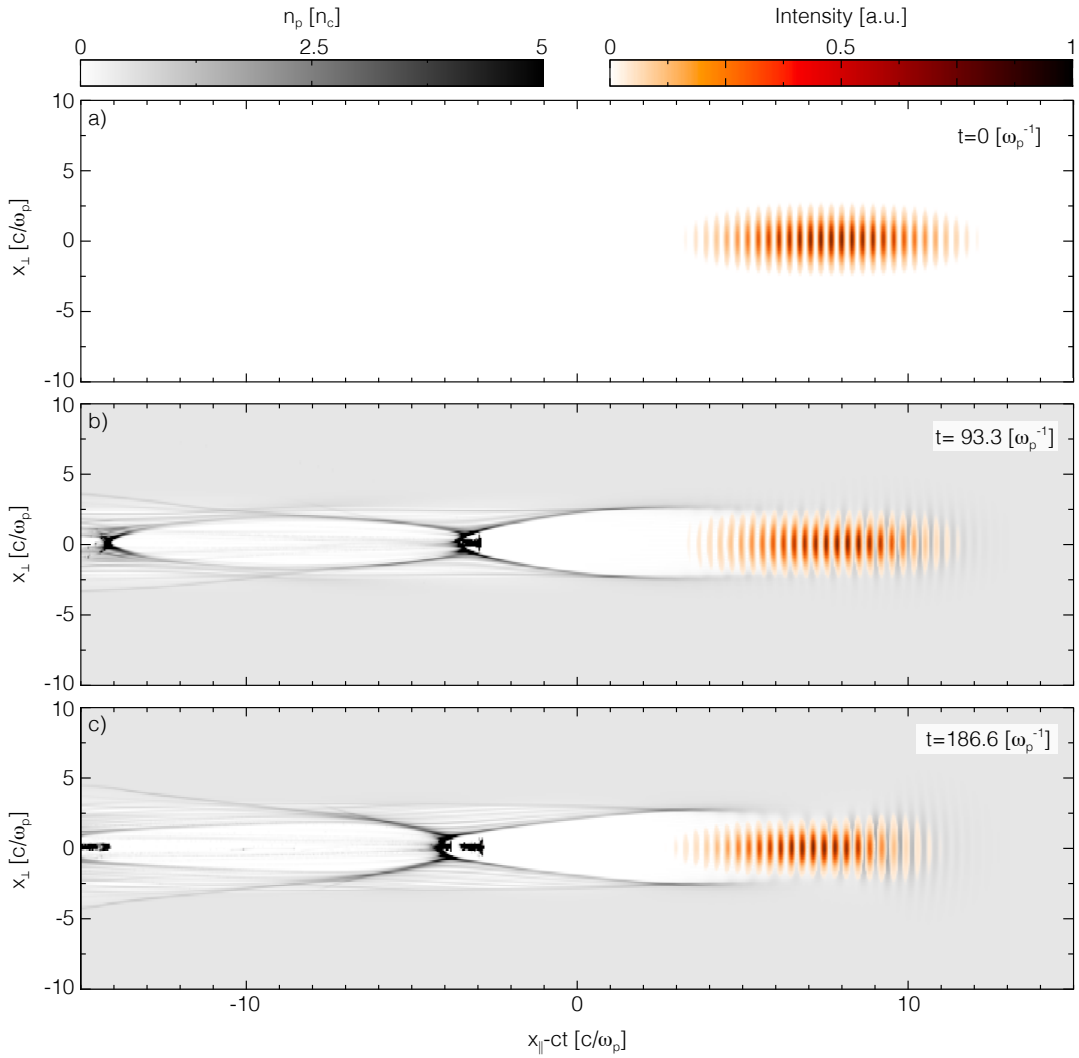

FIGURE 4.3: Conventional pulse interacting with plasma in 3D at a) $t = 0$ $[\omega_p^{-1}]$ b) $t = 91.8$ $[\omega_p^{-1}]$ and c) $t = 183.6$ $[\omega_p^{-1}]$. Speed of the pulse $v_g = 1.05c$, normalized vector potential $a_0 = 2.0$

celerating and defocusing forces. It is possible to have a laser going at velocities that are just barely superluminal, increasing the overall acceleration distance. The main benefit, however, is the greater accelerating field that the plasma can sustain at superluminal speeds, suggesting that the total acceleration length may decrease for the same electron energy.

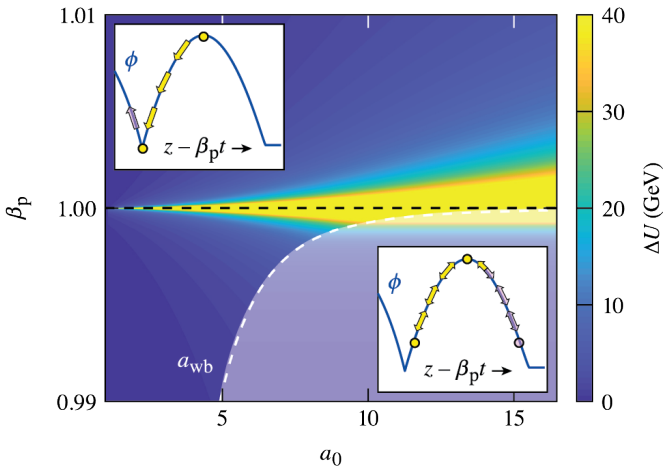

FIGURE 4.4: The design space for superluminal ($\beta_p > 1$) and subluminal ($\beta_p < 1$) LWFA. Wave breaking limits the design space for subluminal LWFA when the amplitude of the driving laser pulse exceeds a threshold value ($a_0 > a_{wb}$). A superluminal LWFA can take advantage of an arbitrarily large a_0, preserving the structure of the wakefield and its peak accelerating field while avoiding the deleterious effects of trapping. The top and bottom insets contrast in the dynamics of an electron that achieves the maximum energy gain injected at rest into the potential of a super and subluminal wake, respectively. The solid(yellow) arrows mark the path over which the electron gains energy. Taken from [67]

4.3 RADIATION PRODUCTION

4.3.1 QUASIPARTICLE RADIATION

As we discussed in Chapter 2, by creating current structures with a certain size we are able to coherently radiate for wavelengths equal to or larger than that size. In the same chapter, we used a plasma density ramp and a regular laser driver to show that the back of the bubble travels superluminally and therefore radiates at the Cherenkov angle of the perturbation. By using spatiotemporal pulses, and by looking at Fig. 4.2, we observe a very similar effect. To know the typical wavelengths of the emitted radiation, we must know the dimensions of the current profiles at the back of the bubble.

There are analytical models that predict the bubble size and overall shape when in contact with very intense (gaussian) lasers, but they tend to give erroneous results or even diverge at the back of the bubble. Due to the lack of three-dimensional analytical results for those current profiles at the back of the bubble, the one-dimensional theory can give insight into how the current spike dimensions.

In the 1D regime, the maximum density of a superluminal wake approaches $(\beta_p - 1)^{-1}\beta_p$ as the electrons approach the speed of speed of light. In the superlumi-

nal driver regime, a higher velocity caused a longitudinal broadening of the current spike, meaning that to radiate very small wavelengths the driver should go as close as possible to the speed of light, but always slightly faster. Even though we did not conduct studies on the radiation, we estimate that the brightness and wavelength of the radiation emitted could be on par to the scheme in Chapter 2, section .

Even though the pulses can be employed indirectly to produce radiation, they can also directly interact with electron bunches to radiate, such as in Thomson scattering.

4.3.2 Thomson Scattering

In Nonlinear Thomson scattering (NLTS), an electron beam interacts with a counter-propagating laser pulse, causing the electron beam to oscillate and reemit the photons of the laser pulse at a shifted frequency. Nonlinear Thomson Scattering is able to convert optical light to x-rays and beyond, meaning it can produce collimated, high energy radiation [82, 83, 84].

When an electron beam interacts with a laser pulse with normalized vector potential $a > 1$, the typically emitted frequencies are given by

$$\omega_n \approx 8n\gamma_0^2\omega_0/a^2, \tag{4.2}$$

where ω_n are the emitted harmonics and γ_0 is the electron Lorentz factor. Interestingly, the higher a, the smaller harmonic the emitted frequency is (even though this is true, the cutoff frequency also increases with a). This is due to the interaction between the electron and the laser pulse: as the electron enters the laser field, the ponderomotive force decelerates the electron and therefore the emitted frequencies decrease. This has the undesirable side effect of making the amplitude of the electron oscillations grow and therefore widen the emission angle. Spatiotemporal pulse shaping offers additional control of the ponderomotive force [85], which can 1) compensate the ponderomotive force deceleration of NLTS, which we called the *drift-free* regime or 2) accelerate the electrons even further to the laser focal speed, which we called *matched NLTS*. To stay in the same radiating regime, the phase velocity must still counter-propagate with relation to the electron, but the focal speed should now propagate with the electron. This possibility is forbidden to standard gaussian pulses where $\tilde{v}$ and v_ϕ always point to the same direction. The electron oscillations and the laser profile for both the conventional regime and the new regime with ponderomotive control are shown in Fig. 4.5.

The drift-free regime, where the ponderomotive deceleration was fully compensated, means that the longitudinal electron speed does not change throughout the interaction. To accomplish this, the focal speed of the laser should be set to $\beta_p = \beta_0^{-1}$,

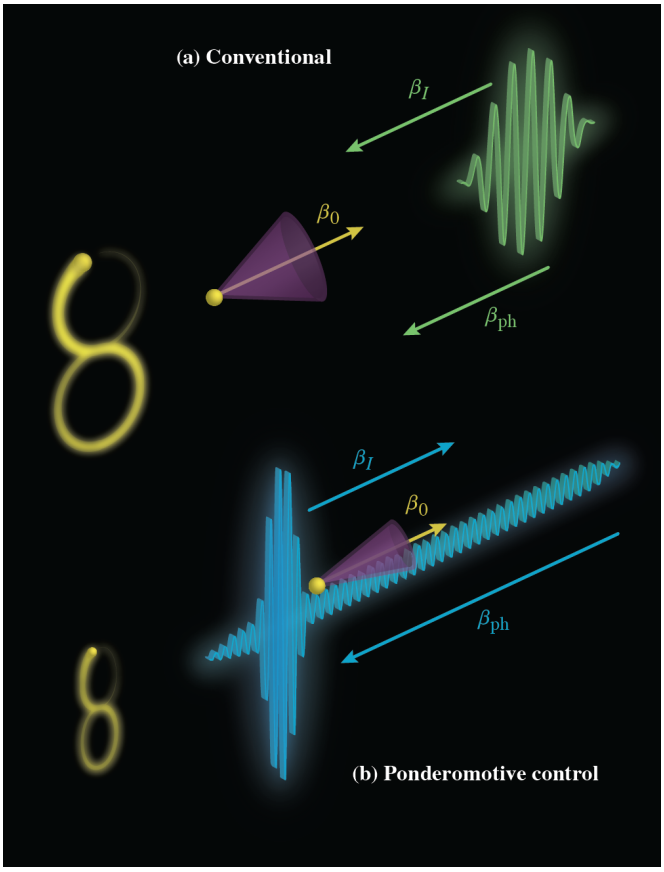

FIGURE 4.5: A conventional NLTS configuration in which the intensity peak and phase fronts of a laser pulse travel in the opposite direction as the electron. At the rising edge of the intensity peak, the ponderomotive force decelerates the electron, redshifting the emitted frequencies and widening their emission angle (purple cone). (b) NLTS with ponderomotive control aligns the velocities of the intensity peak and the electron. Here the ponderomotive force increases or maintains the electron velocity, allowing for higher-frequency emission into a smaller angle. The electron trajectory in its average rest frame (figure eight) is depicted to the left of each case. Taken from [85].

where $c\beta_0$ is the electron speed, meaning we are strictly dealing with superluminal foci. It is possible to show that the harmonics generated are given now by [85]:

$$\omega_n = n\omega_0(1+\beta_0)^2\gamma_0^2, \tag{4.3}$$

which is different from Eq. (4.2) as it does not depend on the laser intensity. Other important properties of radiation emission are the cycle-averaged power, the emission angle, and bandwidth. In comparison to the conventional regime, both the cycle-averaged power and bandwidth are increased by a factor of a, which means that we see most differences when using high-intensity lasers. The emission angle is decreased

from the conventional case by the same factor, which means that we would have a more collimated emission.

Matched NLTS uses a subluminal intensity peak to ponderomotively accelerate the electron. Here the intensity peak intercepts the electron from behind and gradually accelerates it to an asymptotic velocity $\beta_d = \beta_I$. This allows the electron to experience a near-constant vector potential for an extended distance (Fig. 4.6, inset). Setting the ponderomotive velocity $v_I/c = \beta_I$ to satisfy

$$(\beta_I - \beta_0)\gamma_I\gamma_0 = a_0/\sqrt{2} \tag{4.4}$$

ensures that the electron travels with the intensity peak near the maximum vector potential a_0. It is noteworthy to understand that while in the drift-free case, the ponderomotive velocity does not depend on the laser a_0, it is necessary to coordinate between three variables (β_I, β_0, and β_0) to be able to enter the matched regime, which poses a more difficult experimental problem.

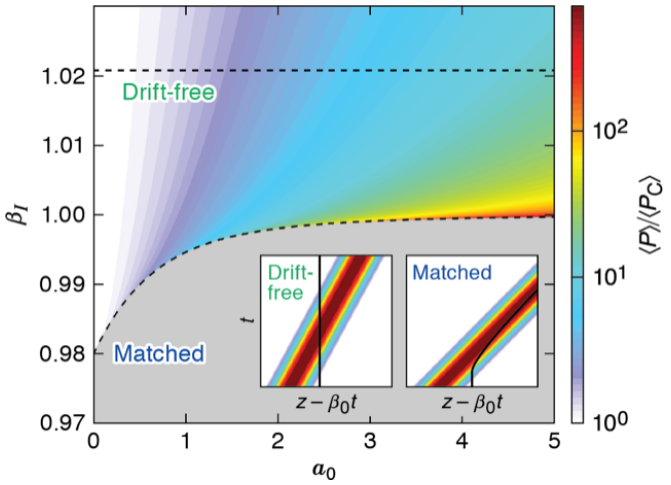

FIGURE 4.6: Cycle-averaged radiated power as a function of the ponderomotive velocity β_I and the vector potential a normalized to power radiated in conventional NLTS $< P_C >$. Here $\gamma_0 = 5$, and for the purpose of calculating $< P_C >$, $\beta_I = -1$. The dashed lines indicate the matched and drift-free conditions. Within the gray region, the ponderomotive force accelerates the electron to a velocity greater than β_I, and the electron outruns the intensity peak. The insets depict the cycle-averaged electron trajectories (black lines) relative to the motion of the intensity peak (contours). Taken from [85].

This new matched regime can enhance the NTLS properties. The harmonics generated are given by

$$\omega_n = n\omega_0(1+\beta_I)^2\gamma_I^2, \tag{4.5}$$

which is almost identical to Eq. (4.3) except that the variables related to the electron speed $c\beta_0$ are now related to the laser focal speed $c\beta_I$. The physical argument

to explain both phenomena goes as follows: in reality, the important features are the electron energy when in contact with the peak laser intensity, and the laser frequency ω_0. In the *drift-free* case the electron stays at energy $m_e\gamma_0$, whereas in the matched case the electron accelerates toward the laser group speed and then stay at that speed for a long time, meaning the energy is $m_e\gamma_I$.

It is necessary to emphasize that slow electrons will not lead to a large harmonic content in the *drift-free* case, as the initial electron energy stays the same. However, at any (small) electron speed $c\beta_0$ it is possible to select an (large) γ_I (which corresponds to a focal speed very close to the speed of light) and laser intensity a_0 such that Eq. (4.4) is satisfied, meaning that very high harmonic content can be generated by an initially slow electron beam.

The ponderomotive force also acts transversally on the electrons, pushing the electrons away from the regions of highest intensities, diminishing the emitted power. To make the electrons stay at the laser focus, the laser must have a transverse profile with a bowl shape, as seen in Fig. 4.7.

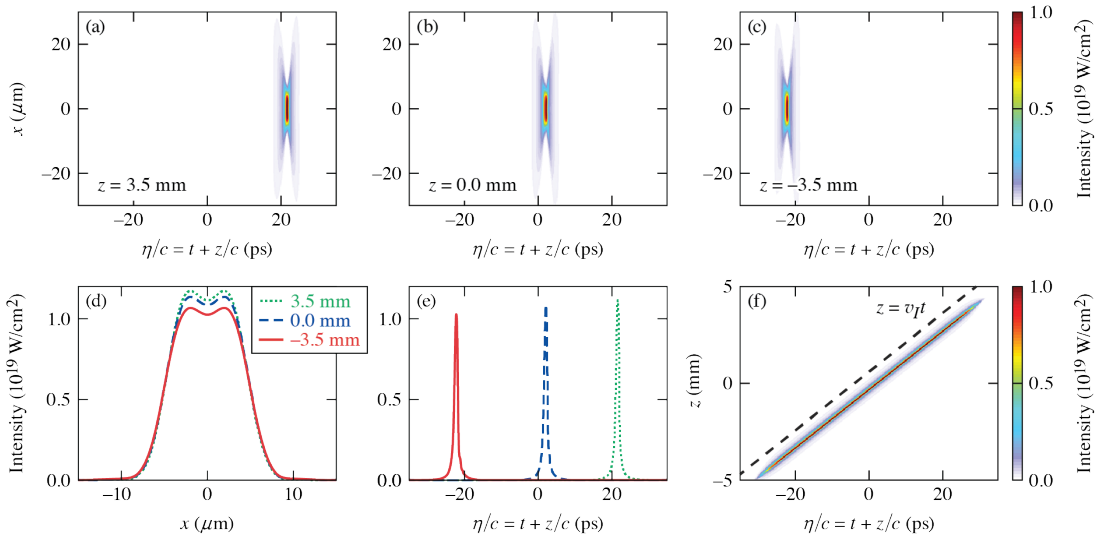

FIGURE 4.7: Example of a practical flying focus design for drift-free NLTS. (a) - (c) Evolution of the propagation invariant intensity profile across the interaction region L. The flying focus pulse travels from right to left, while its intensity peak travels from left to right. The intensity peak counter-propagates with respect to the phase fronts and maintains a stationary profile in the frame $\xi = z - v_I t$. (d) The bowl-shaped transverse intensity profile formed by the orthogonally polarized Laguerre-Gaussian modes. (e) The on-axis ($r = 0$) temporal profile of the intensity peak. (f) On-axis intensity as a function of z and η. The dashed line illustrates the slope of the expected trajectory. Note that the abscissa is $\eta/c = t + z/c$ and that a laboratory frame trajectory $z = v_I t$ is equivalent to $z = v_g v_I \eta/c(v_g - v_I)$. Taken from [85].

To complement the theoretical results, we did 2D particle-in-cell simulations,

which confirmed the theoretical results for the harmonic content in the emitted radiation. The simulations had an electron beam ($\gamma_0 = 5$) interacting with a non-evolving (not self-consistent) laser profile ($a_0 = 3$), which made the electron beam oscillate and radiate. For the drift-free case, the focal speed was given by $\beta_p = \beta_0^{-1} \approx 1.02$. For the matched case, $\gamma_I \approx 22.12$. The radiation was captured using RaDiO [39]. The results are shown in Fig. 4.8. As observed in the second row, for on-axis emission ($\theta = 0$) the harmonics are given by multiples of $4\gamma_0^2\omega_0$, which coincides with the theoretical predictions. For the matched case (third row), the harmonics follow multiples of $4\gamma_I^2\omega_0$, which are approximately $(22/5)^2 = 19.36$ times larger. The simulations were conducted both with a cold beam (right) or with 5% energy spread in the longitudinal direction. With the larger energy spread, we find an almost continuous spectrum both in the matched case and the conventional case, albeit for different reasons. In the conventional regime, the harmonics are so close together that the energy spread immediately blurs out the space between the spectrum lines. In the *matched case* (Fig. 4.8, bottom row), while the spacing is larger, some of the electrons do not get accelerated to (and stay at) γ_I. In fact, any energy change in the electron initial speed means that either the electron overtakes the laser or cannot accelerate to the laser speed, which results in radically different trajectories along time.

In the *drift regime* (Fig. 4.8, middle row), the spectrum lines are still separated at spreads of 5%, which indicates that this regime is less sensitive to variation in the electron speed. In this regime, because the laser is superluminal, it will overtake any electron regardless of their initial energy, which results in similar trajectories for electrons along the interaction.

At the same total laser pulse energy, the amount of energy radiated by the two new schemes is larger than for the conventional scheme.

4.4 Conclusions and Future Work

The new class of lasers described in Chapter 3 was used in two usual setups: electron acceleration (LWFA) and radiation production. We were able to show that in both cases there are situations where the spatiotemporal pulses provide actual benefits over regular laser pulses.

Using pulses with a superluminal focal speed, we are able to create superluminal plasma wakefields, which prevent dark current and enable the acceleration of electrons over larger distances, due to the mitigation of dephasing. Further scientific study is needed to understand how the electromagnetic energy escapes the bubble, as that can increase the emittance of the accelerated beam.

Applying the same pulses to radiation production has two main results. When applying the same theoretical knowledge developed in Chapter 2, Cherenkov-like ra-

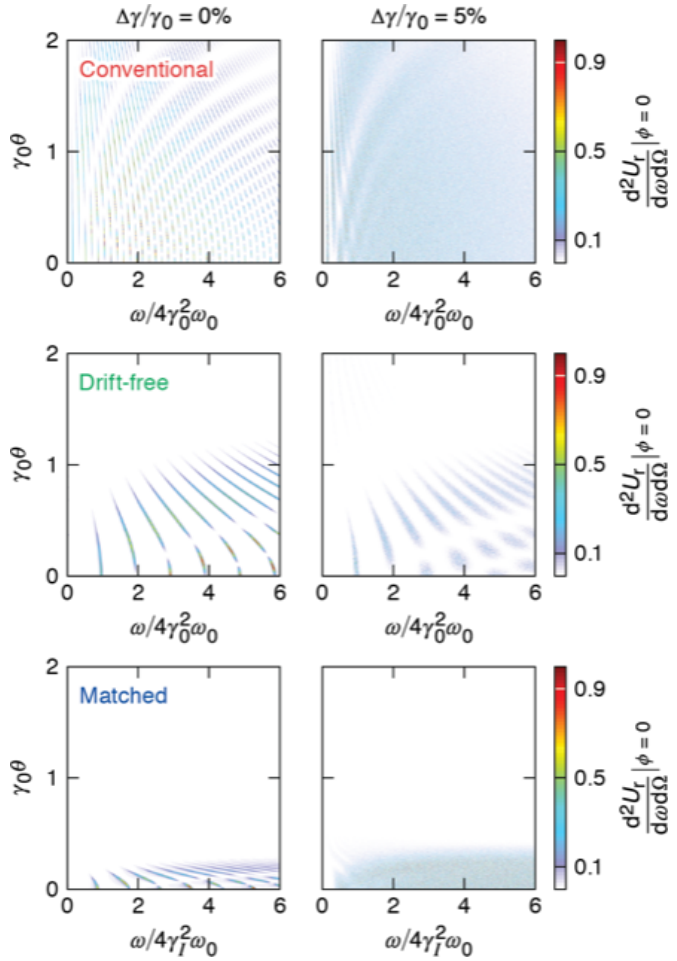

FIGURE 4.8: Spectrum of emitted radiation from a collection of electrons with $\gamma 0 = 5$ and $a_0 = 3$. Left: No energy spread; right: $\gamma/\gamma_0 = 5$ % all in the longitudinal momentum. The quantity U_r has units of energy, and each plot is normalized to its maximum value. For matched NLTS, the horizontal axis is scaled to $4\gamma_I^2\omega_0$, not $4\gamma_0^2\omega_0$, and therefore extends to much higher frequencies. Taken from [85].

diation can be emitted from these superluminal current profiles at the back of the bubble. Further study on the three-dimensional bubble profile created by these superluminal pulses may give more insight into the current profile dimensions, which will in turn predict the bandwidth of the radiation emitted. We showed the possibility of using these pulses to enhance Thomson scattering, by studying the interaction of an electron beam and pulses where the focal speed and phase speed are counter-propagating. These pulses were able to overcome one important shortcoming of the conventional Thomson scattering: the loss of energy by the electron beam as it is decelerated by the laser ponderomotive force. Two regimes were found where the decel-

eration is avoided, such as one where the electron keeps the same longitudinal speed throughout the interaction with the laser pulse and another where the electron is accelerated up to the laser pulse focal speed. The two regimes yielded more energy than the conventional case at the same total laser energy. Full three-dimensional simulations are needed to confirm the feasibility at the laboratory, and new ways of injecting pulses into PIC simulations are being developed to avoid issues with the large transverse dimensions of the spatiotemporal beams[86], which will allow for full 3D simulations of realistic laser pulse profiles.

4.5 Papers in refereed journals

J. P. Palastro, B. Malaca, J. Vieira, D. Ramsey, T. T. Simpson, P. Franke, J. L. Shaw, D. H. Froula; Laser-plasma acceleration beyond wave breaking. Physics of Plasmas **28** (1): 013109. https://doi.org/10.1063/5.0036627

D. Ramsey, B. Malaca, A. Di Piazza, M. Formanek, P. Franke, D. H. Froula, M. Pardal, T. T. Simpson, J. Vieira, K. Weichman, and J. P. Palastro; Nonlinear Thomson scattering with ponderomotive control; Phys. Rev. E **105** (6): 065201 (2022). https://link.aps.org/doi/10.1103/PhysRevE.105.065201

K. Weichman, K.G. Miller, B. Malaca, W.B. Mori, J.R. Pierce, D. Ramsey, J. Vieira, M. Vranic, J.P. Palastro, Analytic pulse technique for computational electromagnetics, Computer Physics Communications **298** 109096 (2024) https://doi.org/10.1016/j.cpc.2024.109096.

CHAPTER 5

COHERENT BETATRON EMISSION FROM FLYING FOCI SETUPS

5.1 INTRODUCTION

Betatron emission refers to radiation from electron beams oscillating transversally in the ion bubble of wakefield accelerators. Typical electron beams in this configuration can emit X-rays [1], albeit incoherently. By taking into account the number of electrons in such beams, being able to get coherent radiation out of these oscillations would allow the intensities to get closer to the free electron lasers.

The theoretical background established in Chapter 2 allows us to generate quasi-particles with exotic properties with different experimental setups, many of which use flying focus pulses. We have already shown in Chapter 4 how the interaction with spatiotemporal pulses and plasmas may generate Cherenkov-like radiation, but the small energy of the particles in the bubble sheath (e.g. below 10 MeV) prevents hard x-ray emission.

In a free electron laser, the longitudinal bunching that stems from the FEL instability allows to emit temporally coherent light. To make betatron oscillations emit temporally coherent light, one must get some longitudinal bunching of particles.

Betatron oscillations refer to the electrons path while subject a transverse force (or more precisely, a force $F \propto E_r - B_\theta$, where E_r is the transverse electric field and B_θ is the azimuthal magnetic field in a cylindrically symmetric setup). Betatron radiation refers to the radiation emitted by electrons undergoing betatron oscillations.

In the experiments that aim to produce betatron radiation using plasma acceleration, we observe that electrons have random phases and the energy spread is high

(tens of percent). Any of these two properties will prevent longitudinal bunching.

However, even if electrons have the same phase and travel with the same speed along the propagation axis they will still not bunch up, as seen in Fig. 5.1a). We could imagine a transverse force that acts on the back of the beam first and on the front of the beam later.

$$F/e = \begin{cases} E_r - B_\theta = \alpha r & , x < v_m t - L/2 \\ E_r - B_\theta = 0 & , x \geq v_m t - L/2 \end{cases} \tag{5.1}$$

A transverse force that travels at a superluminal speed $v_m > v_b$ (where v_b is the speed of the beam) immediately starts introducing a longitudinal bunching, as illustrated by Fig.5.1b)-c). As the speed of the front increases, the longitudinal size of the bunching also increases, which suggests that for X-ray emission one must have small $|v_m - v_b|$ (meaning the size of the current profiles goes to 0 as v_m approaches v_b. We show this in Fig. 5.1 b1-3) and c1-3), where in b) the speed of the magnetic field front v_m is $1.02c$ and in c) $v_m = 1.01c$ compared with the beam speed $v_b = c$.

5.2 THEORY

It is now important to define how to create such a transverse force travelling at v_m. We know that an electron beam travelling through a plasma generates a non-linear wakefield and creates an ion bubble, which attracts electrons. However, if an electron beam travels in plasma, the whole bunch is subject to these focusing forces almost immediately (the head of the pulse will feel the force before the tail, think $v_m = 0 \Leftrightarrow v_m - v_b = -c$), creating current structures that radiate at the beam length σ_x (see Fig.5.1 a1-3). Typically, used beams have $\sigma_x > 1$ μm. Therefore, only using an electron beam and plasma will not result in short-wavelength coherent radiation, with wavelength below σ_x To accomplish such an effect, our scheme uses ionization coming from a laser with a superluminal focus.

When an electron beam travels through a gas, it is not affected by focusing forces (except the defocusing self-forces that expand the beam), as the gas is not electrically charged and therefore interacts very little with the electron beam. Let us imagine then an electron beam traveling through a unionized gas. Moving coaxially, an ionizing laser pulse travels superluminally, meaning that it creates a superluminal ionization front, moving from the back of the pulse to the head of the pulse. As the laser travels through the electron beam, the front electrons are still traveling through gas (and therefore do not interact with the medium) whereas the back electrons start moving through plasma. The fraction of the electron beam that travels through plasma (in the back) excites a nonlinear plasma wave, which in turn focuses those electrons at the back. As the laser travels through the pulse, the fraction of the beam that travels

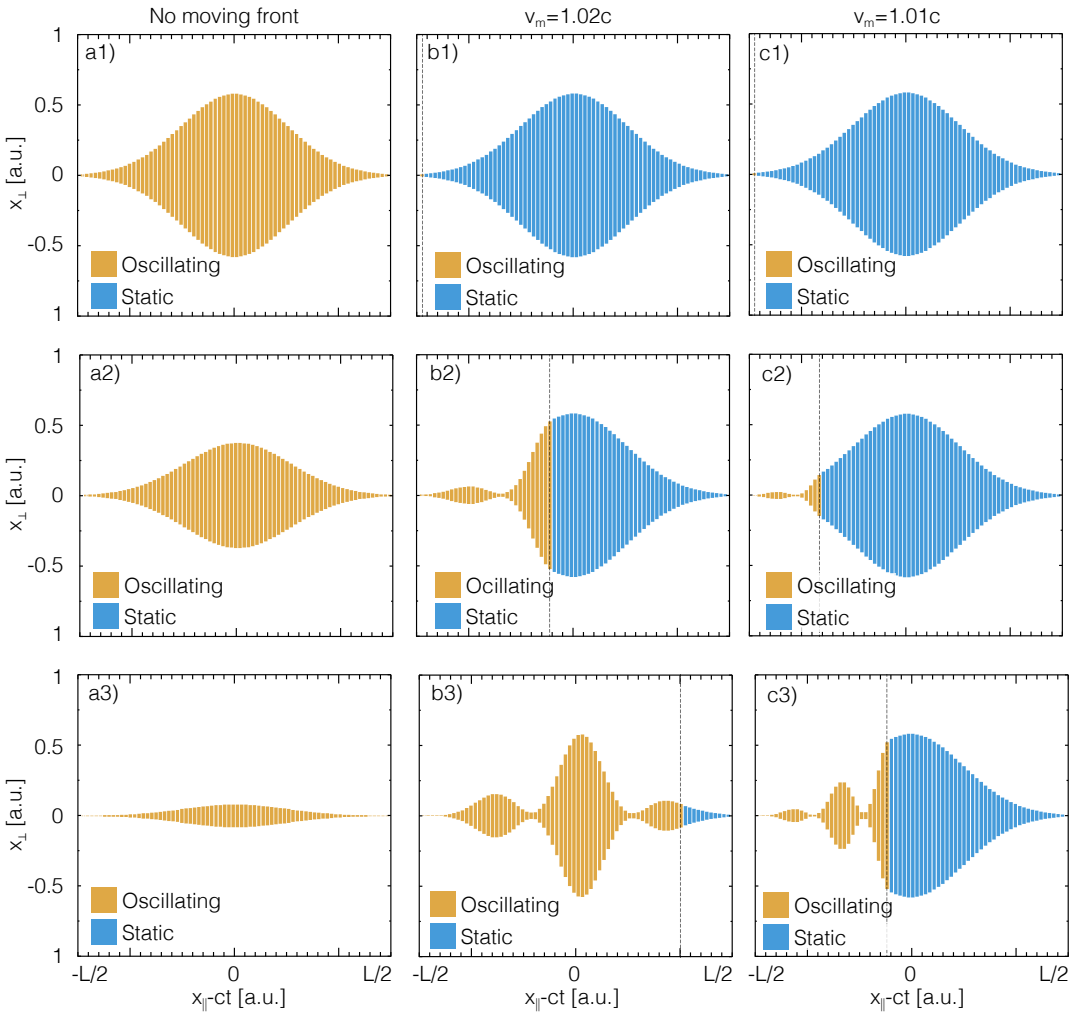

FIGURE 5.1: Formation of longitudinal structures using betatron motion. The electron beam is represented as slices, yellow slices oscillate at the betatron frequency while blue slices do not oscillate. Left column: Three snapshots of the electron beam all oscillating at the same phase. Middle column: A front marked with a dashed line traveling with $v_m = 1.02c$ turns static slices into oscillating slices, forming longitudinal structures. Right column: A front marked with a dashed line traveling with $v_m = 1.01c$ turns static slices into oscillating slices, and the formation of smaller longitudinal structures is observed.

through the plasma increases, but the initial time at which any beam electron starts to oscillate corresponds to the instant the gas around it is ionized. Because the ionization front moves with $v = v_m$, the betatron phase depends on the longitudinal position inside the beam. This is exactly what we show in Fig. 5.1, where v_m is the speed of the ionization front.

This process modulates the electron bunch, as schematized in Fig. 5.1b-c. We

now want to determine what is the typical length associated to the betatron motion as a function of the Lorentz factor of the beam and the v_m. Firstly, we will separate the beam into slices (at very high γ, slices do not interact much with each other) and observe the evolution of each slice along space (we define a slice as the portion of beam electrons between a given $x_{\parallel} - ct$ and $(x_{\parallel} + \delta) - ct$).

5.2.1 SINGLE SLICE EVOLUTION

The behavior of a beam slice in a focusing field is determined by its normalized emittance and the strength of the focusing fields. The normalized emittance in y is a measure of the total phase space the beam takes in that coordinate and it is given by

$$\epsilon_{x,n} = \frac{1}{mc}\left[\langle x^2\rangle \langle p_x^2\rangle - \langle x p_x\rangle^2\right]^{1/2}, \tag{5.2}$$

where $\langle\cdot\rangle$ is the average f in the beam, x is the position and p_x is the momentum in the x direction.

The behavior of the electron beam with normalized emittance ϵ_N in a focusing field is described by the beam-envelope equation [90]:

$$\frac{\mathrm{d}^2\sigma_r(z)}{\mathrm{d}z^2} + \left[K^2 - \frac{\epsilon_N^2}{\gamma^2\sigma_r^4(z)}\right]\sigma_r(z) = 0 \tag{5.3}$$

,

where z is the longitudinal coordinate, $K = \omega_p/(2\gamma)^{1/2}$ is the field strength in an ion channel, γ is the Lorentz factor, σ_r is the beam width and we disregarded all longitudinal forces. This equation describes two effects: the term dependent on K focuses the beam (if we ignore the other term Eq.(5.3) simply yields a harmonic oscillator), and the other term accounts for the beam divergence (as distance z grows the beam grows wider).

The analytical solution for Eq. (5.3) is given by

$$\sigma_r(z) = \sigma_0\left[1 + \left(\frac{2\epsilon_N^2c^2}{\gamma\sigma_0^4\omega_p^2} - 1\right)\sin^2\left(\frac{\omega_p z}{(2\gamma)^{1/2}c}\right)\right]^{1/2} \tag{5.4}$$

The minimum value for $\sigma_r(z)$ is obtained when the sin function yields 1

$$\sigma_{min} = \sigma_0\left(\frac{2\epsilon_N^2c^2}{\gamma\sigma_0^4\omega_p^2}\right)^{1/2} = \frac{\sqrt{2}\epsilon_N c}{\sqrt{\gamma}\sigma_0\omega_p} \tag{5.5}$$

The solution of Eq.(5.4) is shown in Fig.5.2. It is possible to get the maximum

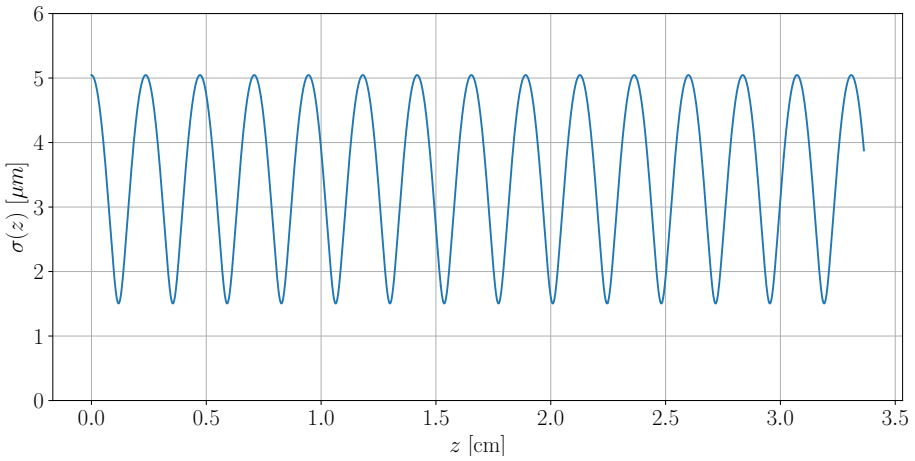

FIGURE 5.2: Evolution of the beam radius of a single slice along the propagation direction. For this plot, $n_e = 10^{17}\text{cm}^{-3}$, $\epsilon_N = 10\ \mu\text{m} \cdot \text{rad}$, and $v_m = 1.001c$.

beam density by assuming cylindrical symmetry. First, we assume that density grows with σ_r^2:

$$\frac{\max(n_b)}{n_{b0}} = \frac{\sigma_0^2}{\sigma_{min}^2} \tag{5.6}$$

This leads us to the expression for the maximum density

$$n_{b,max} = n_{b0} \frac{\gamma^2 \sigma_0^4 \omega_p^2}{\epsilon_N^2 c^2} \tag{5.7}$$

A slice reaches a maximum density periodically, with a period $\Delta t = \pi(2\gamma)^{1/2}\, 1/\omega_p$. The first oscillation takes half as much, as the beam slice must only undergo half the oscillation, as seen from Fig. 5.2. Since the beam is traveling near the speed of light, the distance between those maxima is $\Delta z = \pi(2\gamma)^{1/2}\, c/\omega_p$, which corresponds to half of the betatron wavelength.

5.2.2 ADDING IONIZATION

Now we can introduce the effects of a time-dependent ionization front. As we explained before, this ionization front will come from a spatiotemporally shaped laser pulse. It is hard to model the interaction between a laser, a beam and a gas analytically, and therefore we will assume in this toy model that the ionization front is transversally uniform. We assume that the ionization front is traveling with v_f and starts at the back of the beam, which travels with v_b. The back of the beam starts at $z = 0$,

along with the ionization front. The propagation distance of a slice starting at position z_0 before it gets ionized is given by

$$z_{ion}(z_0) = \frac{z_0 c}{v_f - v_b} \tag{5.8}$$

From Eq. (5.8) one observes that $z_{ion}(0) = 0$, confirming that the ionization starts at the back of the beam. We can now write how σ varies with both the propagation distance z and the initial slice position z_0:

$$\sigma(z, z_0) = \sigma_0 \left\{ 1 + \left(\frac{2\epsilon_N^2 c^2}{\gamma \sigma_0^4 \omega_p^2} - 1 \right) \sin^2 \left[\frac{\omega_p}{(2\gamma)^{1/2} c} (z - z_{ion}(z_0)) \right] \right\}^{:w1/2} \tag{5.9}$$

which gives us

$$\sigma(z, z_0) = \sigma_0 \left\{ 1 + \left(\frac{2\epsilon_N^2 c^2}{\gamma \sigma_0^4 \omega_p^2} - 1 \right) \sin^2 \left[\frac{\omega_p}{(2\gamma)^{1/2} c} \left(z - \frac{z_0 c}{v_f - v_b} \right) \right] \right\}^{1/2} \tag{5.10}$$

Even though the slices are just focusing and defocusing as before, the phase of the oscillation is now dependent of the longitudinal position of the slice in the beam. A waterfall plot showing the variation of σ is shown in Fig. 5.4.

For a $\sigma(z, z_0) = \sigma_{min}$, there is a value Δz_0 such that $\sigma(z, z_0 + \Delta z_0) = \sqrt{2}\sigma_{min}$, which correspond to a length over which the density halves. This Δz_0 will serve as the typical length of each bunch in the current profile, which determines the wavelength down to which there is coherent emission. Of course, Δz_0 would be the HWHM, so the FWHM shall be $2\Delta z_0$.

The equation for Δz_0 is then given by changing the argument of Eq. (5.10):

$$\sigma(z, z_0 + \Delta z_0) = \sigma_0 \left[1 + \left(\frac{2\epsilon_N^2 c^2}{\gamma \sigma_0^4 \omega_p^2} - 1 \right) \sin^2 \left(\frac{\omega_p}{(2\gamma)^{1/2} c} \left(z - \frac{(z_0 + \Delta z_0) c}{v_f - v_b} \right) \right) \right]^{1/2} = \sigma_{min} \sqrt{2} \tag{5.11}$$

Now, it should be clear that if $\Delta z_0 = 0$ we are at the minimum σ and therefore the sin function yields 1. Let us admit the z and z_0 dependent factors inside the sin function yield $\pi/2$ (so the sin yields 1). We now have a simplified expression:

$$\left(\frac{2\epsilon_N^2 c^2}{\gamma \sigma_0^4 \omega_p^2} - 1 \right) \sin^2 \left[\frac{\pi}{2} + \frac{\omega_p}{(2\gamma)^{1/2} c} \left(- \frac{\Delta z_0 c}{v_f - v_b} \right) \right] = 2\sigma_{min}^2 / \sigma_0^2 - 1 \tag{5.12}$$

Identifying $2\epsilon_N^2 c^2 / (\gamma \sigma_0^4 \omega_p^2)$ as $\sigma_{min}^2 / \sigma_0^2$, we can further simplify to

$$\sin^2 \left[\frac{\pi}{2} + \frac{\omega_p}{(2\gamma)^{1/2} c} \left(- \frac{\Delta z_0 c}{v_f - v_b} \right) \right] = \frac{1 - 2\sigma_{min}^2 / \sigma_0^2}{1 - \sigma_{min}^2 / \sigma_0^2} \tag{5.13}$$

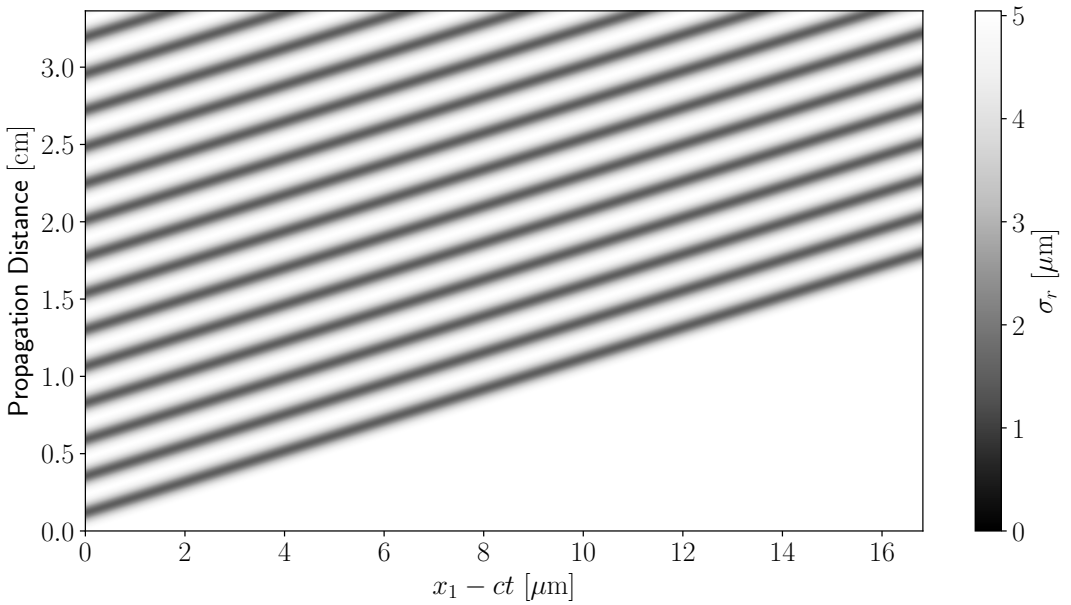

FIGURE 5.3: Waterfall plot showing the formation of longitudinal structures using betatron motion coupled with an z varying ionization. At every propagation distance, the beam radius is plotted along the x-axis. In the beginning, the whole beam stays at $\sigma = 5$ μm. The back of the beam starts to oscillate first, which originates the longitudinal modulation of the beam. For this plot, $n_e = 10^{17}\text{cm}^{-3}$, $\epsilon_N = 10$ $\mu\text{m} \cdot \text{rad}$, and $v_m = 1.001c$.

By using the arcsin function it is possible to solve for Δz_0

$$\Delta z_0 = (v_f - v_b)\frac{(2\gamma)^{1/2}c}{\omega_p}\left(\frac{\pi}{2} - \arcsin\left[\sqrt{\frac{1-2\sigma_{min}^2/\sigma_0^2}{1-\sigma_{min}^2/\sigma_0^2}}\right]\right) \tag{5.14}$$

By taking the Taylor series we can further simplify

$$\Delta z_0 = (v_f - v_b)\frac{(2\gamma)^{1/2}}{\omega_p}\left(\frac{\pi}{2} - \left[\frac{\pi}{2} - \frac{\sigma_{min}}{\sigma_0} - \frac{2}{3}\left(\frac{\sigma_{min}}{\sigma_0}\right)^3 + \mathcal{O}(x^5)\right]\right) \tag{5.15}$$

which finally gives us the FWHM

$$\text{FWHM} = 2\Delta z_0 = 2(v_f - v_b)\frac{(2\gamma)^{1/2}}{\omega_p}\frac{\sqrt{2}\epsilon_N c}{\sqrt{\gamma}\sigma_0^2\omega_p} = 4(\beta_f - \beta_b)\frac{\epsilon_N}{\sigma_0^2}\left(\frac{c}{\omega_p}\right)^2 \tag{5.16}$$

A typical beam modulation is shown in Fig.5.4.

Since we now know the typical dimensions of the current profiles, we can now predict the typical wavelength emitted by such a setup. However, we must note that the electron beam must not ionize the gas by itself, as that would incur in oscillations

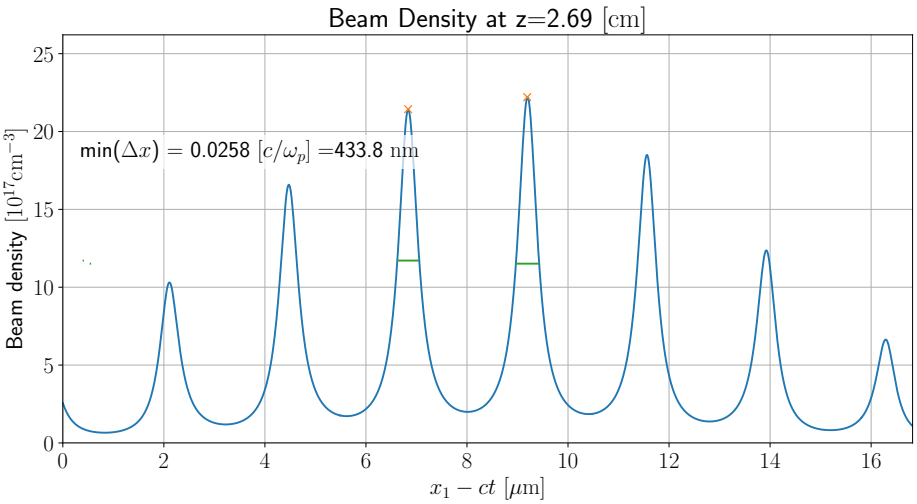

FIGURE 5.4: Snapshot of the on-axis beam density of the electron beam traveling through the plasma. The electron beam had $\sigma_z = 5\ \mu$m. For this plot, $n_e = 10^{17}\text{cm}^{-3}$, $\epsilon_N = 10\ \mu\text{m} \cdot \text{rad}$, and $v_m = 1.001c$. The two maximum values of the beam density are shown in orange and the FWHM is shown in green.

more alike the first column of Fig. 5.1, assuming the velocity distribution is contant along the beam (with the typical current profile of the order of the beam length). At the same time, to go into the nonlinear regime, the beam density must be larger than the plasma density. Since the FWHM scales with $\omega_p^{-2} \propto n_e$, we want to use as large of an electron plasma density (and electron beam density) as possible. The hardest gases to ionize are Hydrogen and Helium, which were used in our simulations. We found that a setup with a plasma density of $n_e = 10^{17}$ cm^{-3} and a beam density $n_b = 4 \times 10^{17}$ cm^{-3} did not ionize the gas prematurely and was able to generate a nonlinear plasma wave both for Hydrogen and Helium. Increasing both densities by a factor of 10 resulted in premature ionization of the plasma, which led us to the former values. Equation (5.16) does depend on v_b (beam speed) but assuming an ultra-relativistic electron beam ($E > 1$GeV) we realize that there is a very small dependency on the Lorentz factor γ, which allows going for smaller electron beam energies. As an example, an electron beam of 1 GeV and one of 10 GeV have the same speed up to the fourth decimal. Of course, if β_f is of the order of $1/\beta_b$ the effect starts to matter.

To get an estimate for ϵ_N, we assume that initially the beam is cold and therefore the emittance growth is due to the direct interaction between the laser pulse and the beam. This means that we can estimate $\epsilon_N \approx a_0\sigma_0$, where a_0 is the normalized vector potential of the laser pulse. Our tests showed that $a_0 = 0.08$, corresponding to a laser intensity of about $I_0 = 10^{16}$ W/cm^2, was enough to properly create a superluminal ionization front, and we could test this theory on laser pulses that were about

20 mJ. This is not a high-intensity laser, like the ones used in the previous chapter ($I_0 \approx 10^{18}$ W/cm^2). This small required laser energy is what enables this application to exist soon, as space-time wave packets have already been created at this energy level [78, 91].

As we know that these pulses can be produced, it makes sense to look at the real size of the current profiles in SI units. An engineering formula for the FWHM is given by

$$\text{FWHM} \approx 17 \frac{\beta_f - \beta_b}{0.001} \frac{a_0}{0.08} \frac{5}{\sigma_0[\mu\text{m}]} \frac{10^{17}}{n_e[\text{cm}^{-3}]} [\text{nm}] \tag{5.17}$$

Equation (5.17) shows we may reach coherent X-rays (below 10 nm) if $\beta_f - \beta_b = 0.0005$. Of course, there are several ways in which real experiments would differ from this idealized setup. For one, the assumption that the focusing force does not depend on the transverse direction is not true, as near the beginning of the plasma wave only the part of the beam that is closest to the axis is focused (most of the bunch is outside the focusing region). This effect can be attenuated by placing the ionising laser closer to the middle of the bunch at $t = 0$, as the bunch current in plasma is able to drive a plasma wave that resembles more a circle, encircling most of the beam. It is also true that longitudinal forces are acting on the beam, which can change the bunch shape we predicted, as $\omega_b(\gamma) = \omega_b[\gamma(z)]$ depends on propagation distance. This effect becomes less evident for bunches with higher energies. We therefore see this toy model above as the best-case scenario for radiation production. As in all nonlinear plasma dynamics, realistic results can only be predicted from particle-in-cell simulations.

5.3 Idealized simulations

To get an estimate for the radiation production, we used an external force that travels superluminally and focuses electrons. This is the ideal scenario that we described beforehand.

To simulate the longitudinal bunching effects on the electron beam, one must resolve the FWHM of the predicted bunching length. At the same time, one must also resolve the predicted minimum σ. To accomplish this, we use quasi-3D simulations, which use the cylindrical symmetry of the problem to reduce the computation load of the problem. Quasi-3D simulations decompose the problem in azimuthal modes, meaning we expand the fields, charge, and current densities into a Fourier series in ϕ [88],

$$\mathbf{F}(r, z, \phi) = \mathcal{R}\left\{ \sum_{m=0} \mathbf{F}^m(r, z) e^{im\phi} \right\}, \tag{5.18}$$

where $\mathbf{F}$ is any quantity and $\mathbf{F}^m$ is the m-th Fourier harmonic. The harmonics are complex quantities, but the quantity $\mathbf{F}$ is always a real number. The quasi-3D simulation

can be done at a much lower computational cost than a full 3D simulation, which is especially relevant for the transverse resolution needed for this problem.

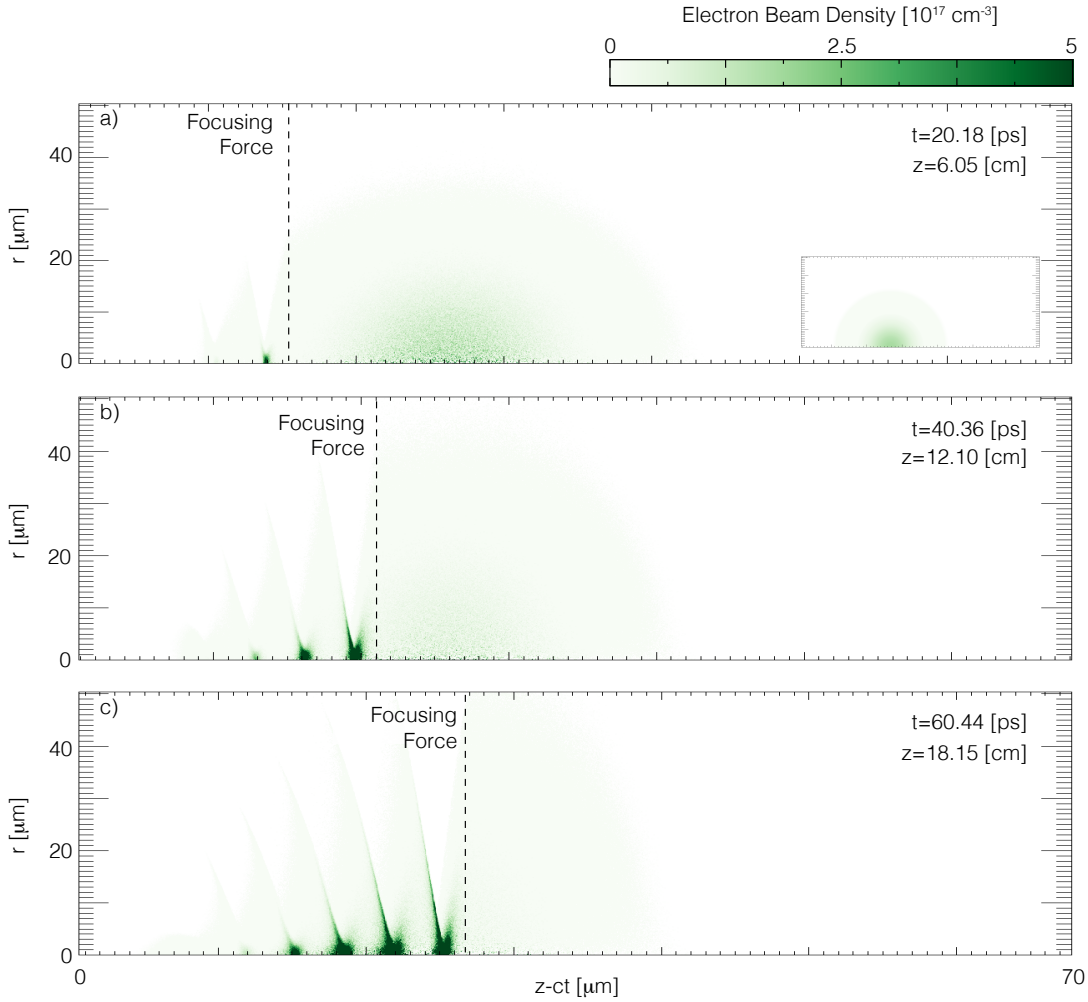

FIGURE 5.5: Snapshots of an OSIRIS simulation of the modulation of an electron beam via a superluminal external field at a) $t = 20.18$ ps, b) $t = 40.36$ ps, and c) $t = 60.44$ ps. The initial electron beam is shown in the inset of plot a). An ideal focusing force is applied to the electrons on the left of the dashed line.

In Fig. 5.5 the electron beam gets focused by an ideal focusing force travelling at a predetermined speed. The electron starts with no modulation (Fig. 5.5a, inset) but with the onset of the betatron oscillations it rapidly creates the first quasiparticle (Fig. 5.5b) (remember that each micro-bunch is a quasiparticle). The other quasiparticles start from further oscillations, which completely modulate the beam, as seen in Fig. 5.5c-d. We found that the predictions for the FWHM were matched by the simulation results.

5.4 REALISTIC SIMULATIONS

To use a more realistic laser profile, we used an injected laser based on the work of Ref. [73], which has recently been implemented in the particle-in-cell code OSIRIS [87]. This laser is created by reflecting a Gaussian laser out of an echelon optic [73], which separates the laser into several rings. After that, it interacts with an axiparabola, an optic whose focal spot depends on the radial reflection point [92]. This means that the several rings are focused at different places, which allows for the formation of a superluminal focus. The initial positions of the laser pulse and the particle beam can be seen in Fig. 5.6. A three-dimensional view of this laser can be found in Fig. 5.7.

To save computational time, the laser pulse was started already on top of the electron beam. It is possible to do simulations where the laser is behind every electron, but this requires the simulation box to increase both longitudinally and perpendicularly.

5.4.1 HELIUM

From Eq. (5.16) we should aim for the highest possible electron density to reach a small FWHM and hence smaller wavelengths. However, having a very dense ultra-relativistic electron beam (remember that n_b must be larger than the plasma density to enter the blowout regime) may ionize the gas. This suggests using gases with the largest ionization energies, reducing spurious ionization from the electron beam. The gas with the highest first ionization energy is Helium, which we used in our first sets of simulations.

The simulation results are available in Fig.5.8. In the first picture, we see that there are two ionization levels, which correspond to the two helium electrons. In Fig. 5.8a), the ionization front is still behind the electron beam, and the density lineout on-axis is still a Gaussian, as it started. In Fig. 5.8b), the ionization front is now in contact with the electron beam, and we already observe that the plasma density on-axis is smaller than off-axis, due to the plasma wave that is forming. The plasma is not in the bubble regime yet, as the current of the electron beam in contact with the plasma is still not enough to drive a nonlinear plasma wave. In Fig. 5.8c), we are fully in the nonlinear regime. Fig. 5.8 showcases major differences between the toy model and the real setup: the beam is not focused by the same force along the propagation distance and there is is a gap between the first and second ionization (in the case of Hydrogen that does not apply).

According to the equations developed in Chapter 2, the emitted intensity will grow with the number of participating particles squared. To have all the particles in the beam participating, the quasiparticle must travel through the whole beam, which requires increasing the window size both transversal and longitudinally while main-

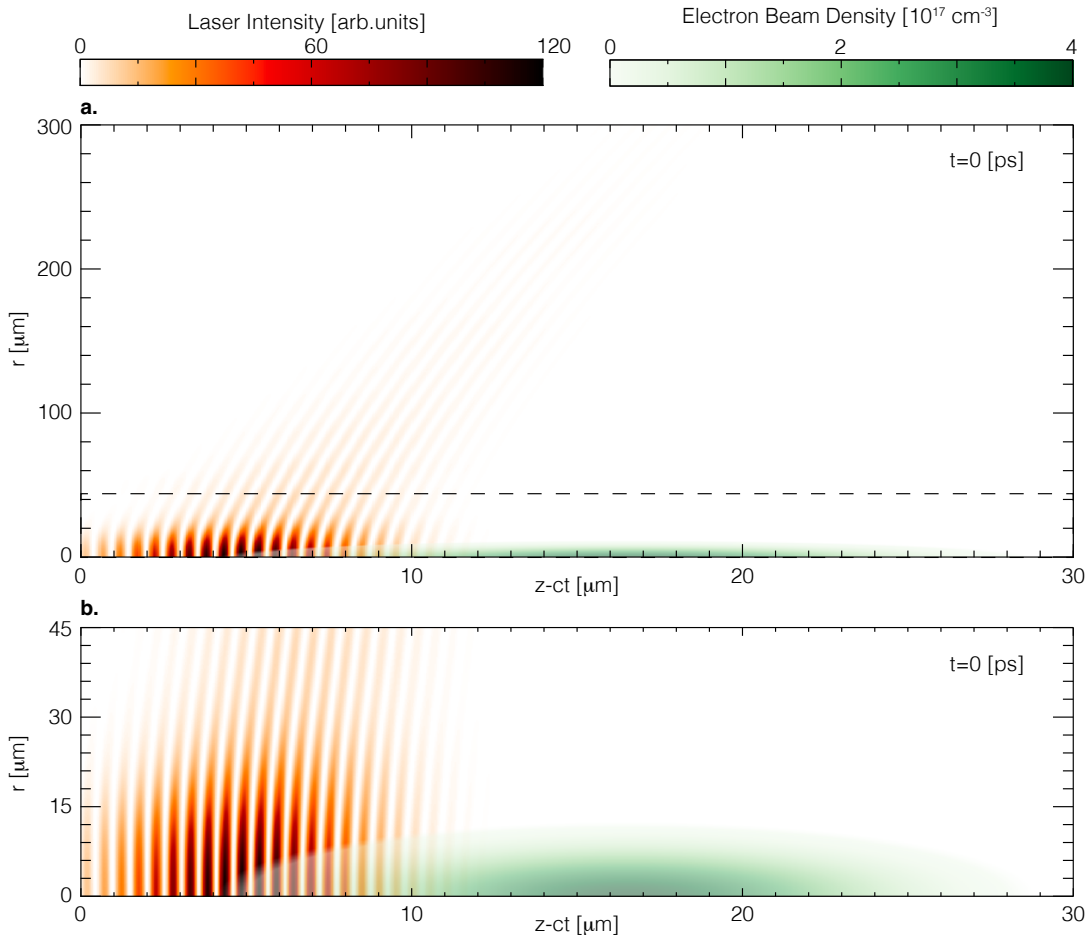

FIGURE 5.6: a. Initial configuration of simulations using realistic laser profile. Laser pulse in orange, electron beam in green. b. Zoomin of previous picture.

taining the resolution. To alleviate this issue, we used a smaller laser focal range and put a fully ionized plasma at a certain position. This means that after some time, the whole beam creates the nonlinear plasma wave and keeps the betatron motion going. A 3D picture of the interaction with the fully ionized plasma is shown in Fig. 5.9.

To verify the speed of the current spike, we took the lineout at every timestep and drew a waterfall plot. The plot is shown in Fig. 5.10. We observe that in these realistic conditions, even though some of the same features of the toy model are replicated, some of the assumptions are not valid. As we see from Fig. 5.8, the electron beam is never totally inside the ion bubble and therefore only the central part of the beam gets focused with the predicted K immediately after the ionization front moves through. As we can see from the lineouts from the same figure, there are still sub-100 nm current spikes, which we had anticipated, but the first betatron oscillation seems

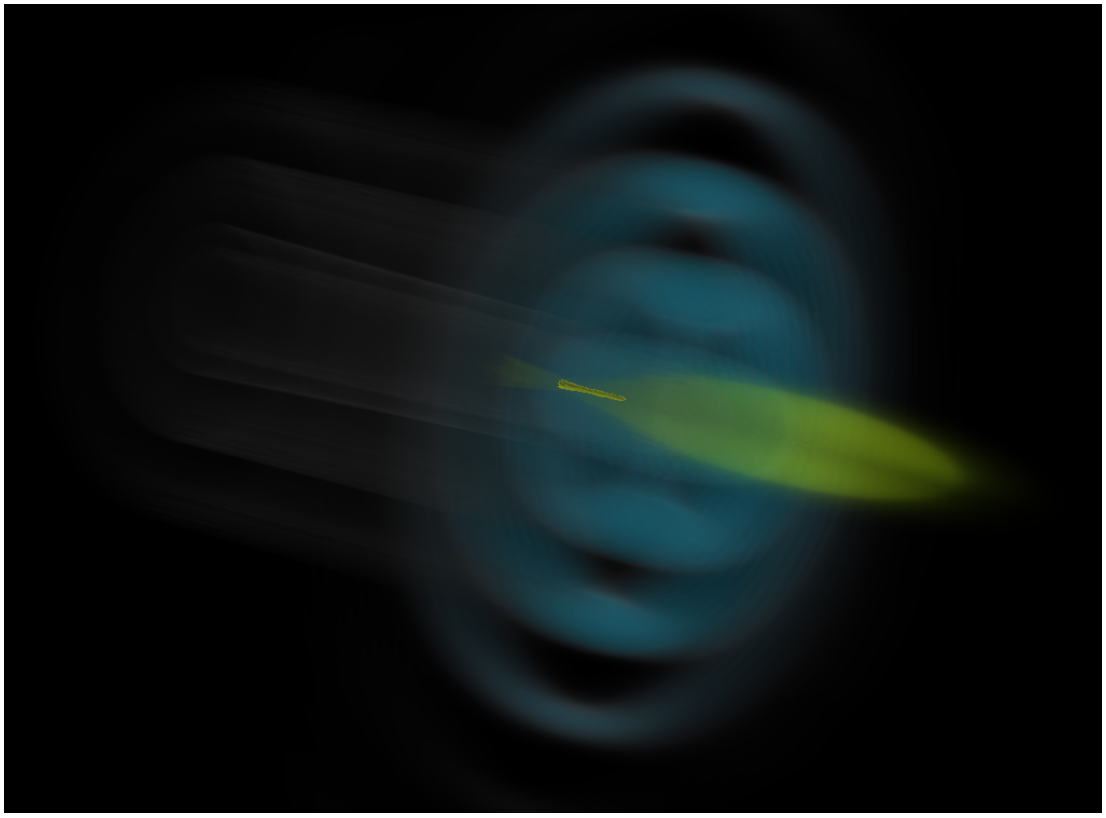

FIGURE 5.7: Three-dimensional view of the quasi-3D simulation showcasing the three different elements of the radiating setup, where the beam starts being modulated. In blue: Spatiotemporal laser pulse described in [73]. In gray: the plasma nonlinear wakefield. In yellow: Electron beam, larger opacity means larger beam density.

to be composed of several current spikes (at around $z - ct = 23\mu$m in Fig. 5.8c), where we only had anticipated one. This is very different from the same lineout taken from the toy model and shown in Fig. 5.4.

By using RaDiO [39], we were able to capture the radiation coming from this interaction. As shown in Chapter 2, we expect off-axis emission at the Cherenkov angle of the ionization front. The spatiotemporal structure of light is shown in Fig.5.11. Even though the majority of the radiation is for very small angles (typical of betatron radiation), we see a distinct off-axis peak very close to the Cherenkov angle. This peak is single-cycle, contrary to what we see on-axis (whose length is the beam length). The inset on Fig. 5.11a) shows that the duration of this single cycle pulse is sub fs. When taking the spectrum, shown in Fig.5.11b), we observe a distinct peak at the same angle, which already shows captured radiation up to 12 eV.

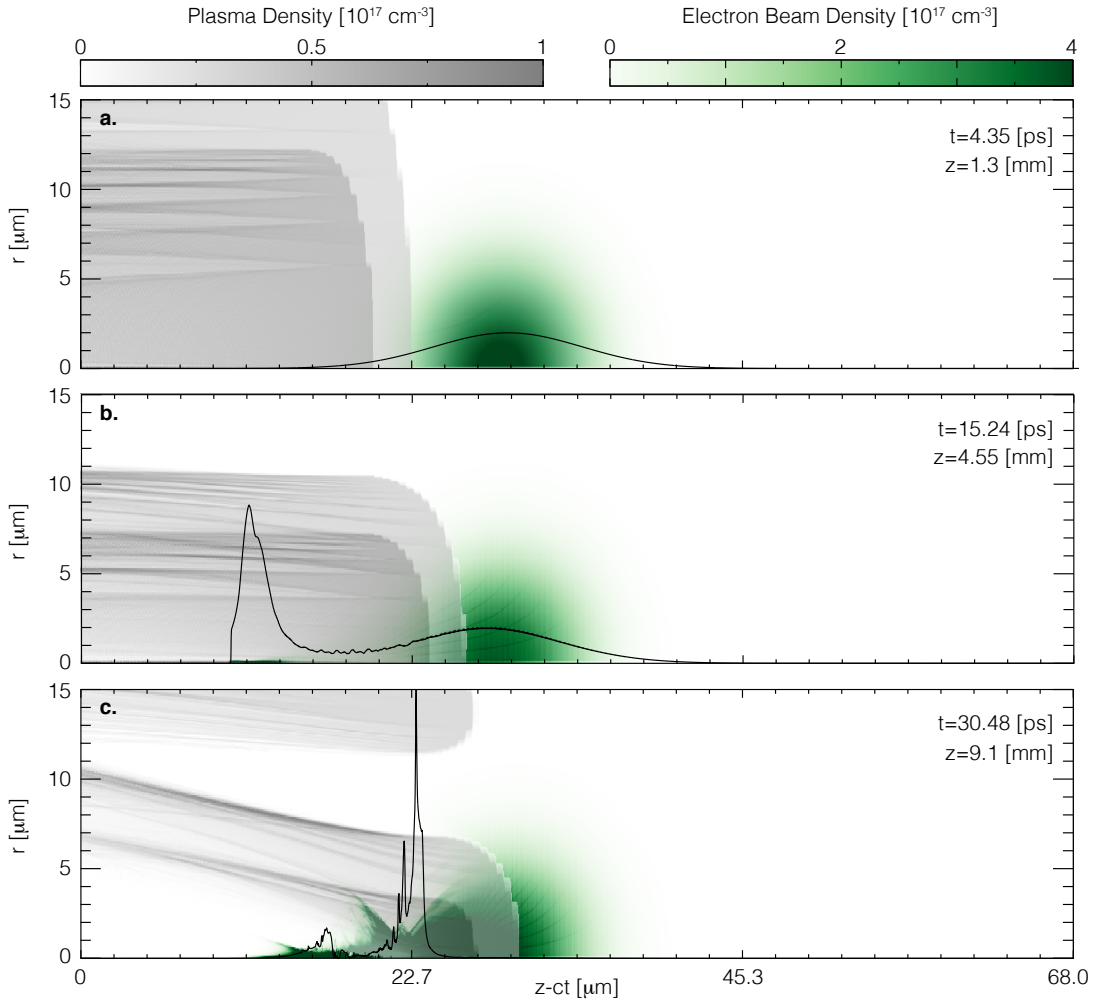

FIGURE 5.8: Snapshots of an OSIRIS simulation of the modulation of an electron beam via a superluminal pulse using Helium gas at a) $t = 4.35$ ps, b) $t = 15.24$ ps, and c) $t = 30.48$ ps. Lineouts of the density on-axis are shown in every plot [Peak Density in a) 4×10^{17} cm^{-3}, b) 20×10^{17} cm^{-3} and c) 2000×10^{17} cm^{-3}]. The ionizing laser pulse is not shown.

5.4.2 HYDROGEN

From subsection 5.4.1 it becomes evident that the two ionization levels of helium play a role in the beam modulation. We found out that even though the modulation occurs, it deviates from the theoretical expectation due to the two ionization fronts, separated by a micrometer-scale length. Using hydrogen instead of Helium eliminates one of the ionization fronts and therefore gets closer to the toy model we developed.

The simulation results are available in Fig.5.12. In Fig. 5.12a), the ionization front started in the middle of the electron bunch and had just formed. The density

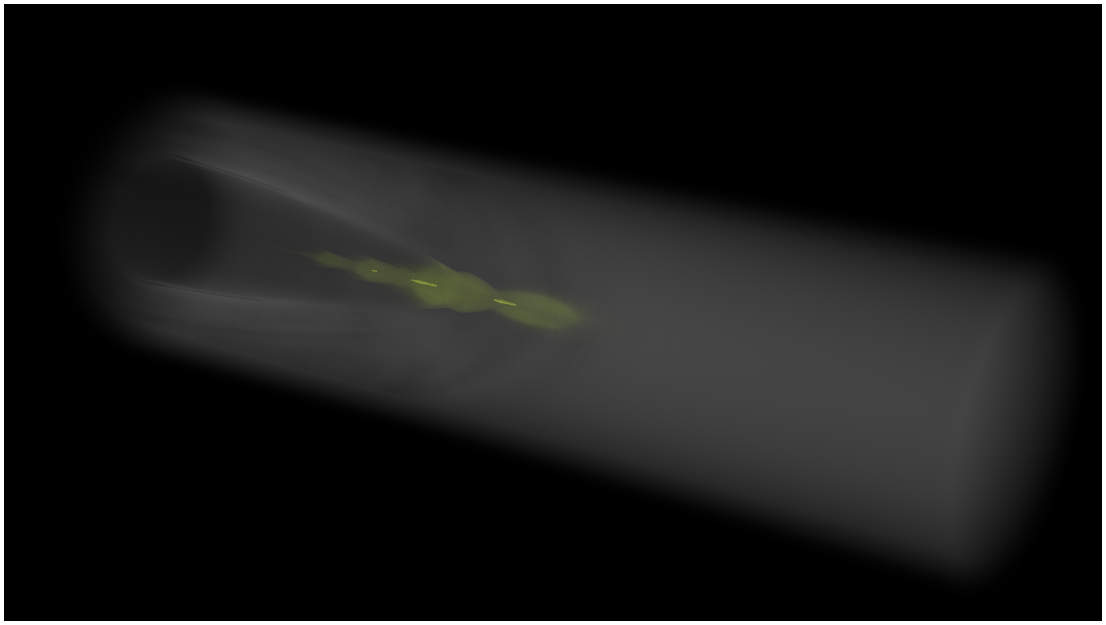

FIGURE 5.9: Three-dimensional view of the quasi-3D simulation showcasing the modulation of the beam after the beam started propagating through a fully ionized plasma after the focal range of the laser ended. In gray: the plasma nonlinear wakefield. In yellow: Electron beam, larger opacity means larger beam density.

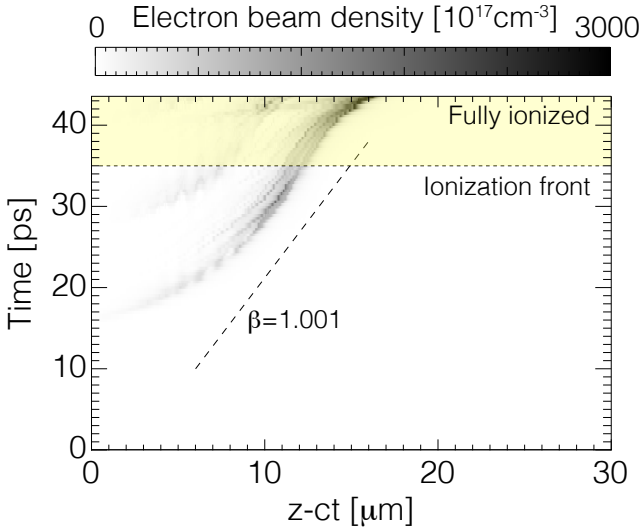

FIGURE 5.10: Waterfall plot of the electron beam density on-axis. Marked in a dashed line is the speed of the ionization front ($\beta_m = 1.001$). In this simulation, the electron beam starts interacting with a fully ionized plasma (instead of a superluminal ionization front) from $t = 35$ ps, which is shown in transparent yellow.

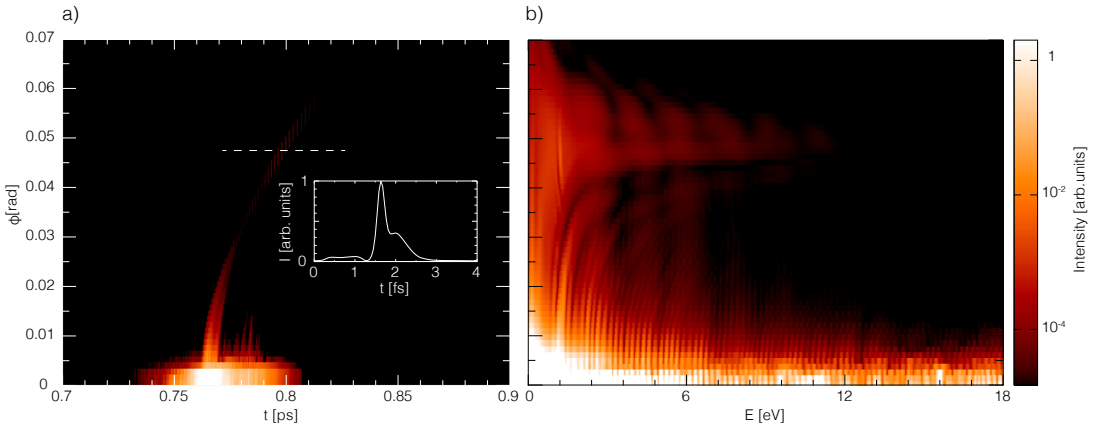

FIGURE 5.11: Spatiotemporal structure and spectrum of the emitted light (simulation using an external field). a) Detected light in a detector in the far field. At angle $\phi = 0$ rad we observe the typical betatron radiation, with the length equal to the beam length. At the Cherenkov angle of the ionization front, we observe sub-fs single-cycle light pulse. b) Spectrum of the emitted light. On-axis we see the appearance of regular betatron radiation while a broadband signal appears off-axis.

lineout on-axis is still a Gaussian, as it started. In Fig. 5.8b), the ionization front is now in contact with the electron beam, and we already observe that the plasma density on-axis is smaller than off-axis, due to the plasma wave that is forming. The plasma is not in the bubble regime yet, as the current of the electron beam in contact with the plasma is still not enough to drive a nonlinear plasma wave. In Fig. 5.8c), we are fully in the nonlinear regime.

An equivalent waterfall plot was taken for the Hydrogen case, and it is shown in Fig. 5.13. We observe a current profile at focus with a constant speed. Even though the pulse is not fully inside the bubble, the result is more similar to the toy model result (Fig. 5.2). The radiation emitted is shown in Fig. 5.14, which shows a temporal peak with about 100 as duration, as opposed to 300 as duration for Helium (shown in Fig. 5.11).

5.5 CONCLUSIONS AND FUTURE WORK

Flying foci pulses with low energy can already be produced in the laboratory. This chapter depicts one of the first possible applications of these pulses towards single-cycle radiation production. With the co-axial propagation of both an electron beam and a superluminal flying focus pulse, a superluminal ionization front is produced. As this front travels from the back to the head of the electron beam, the nonlinear wave that forms can focus the part of the electron beam that is behind the ionization

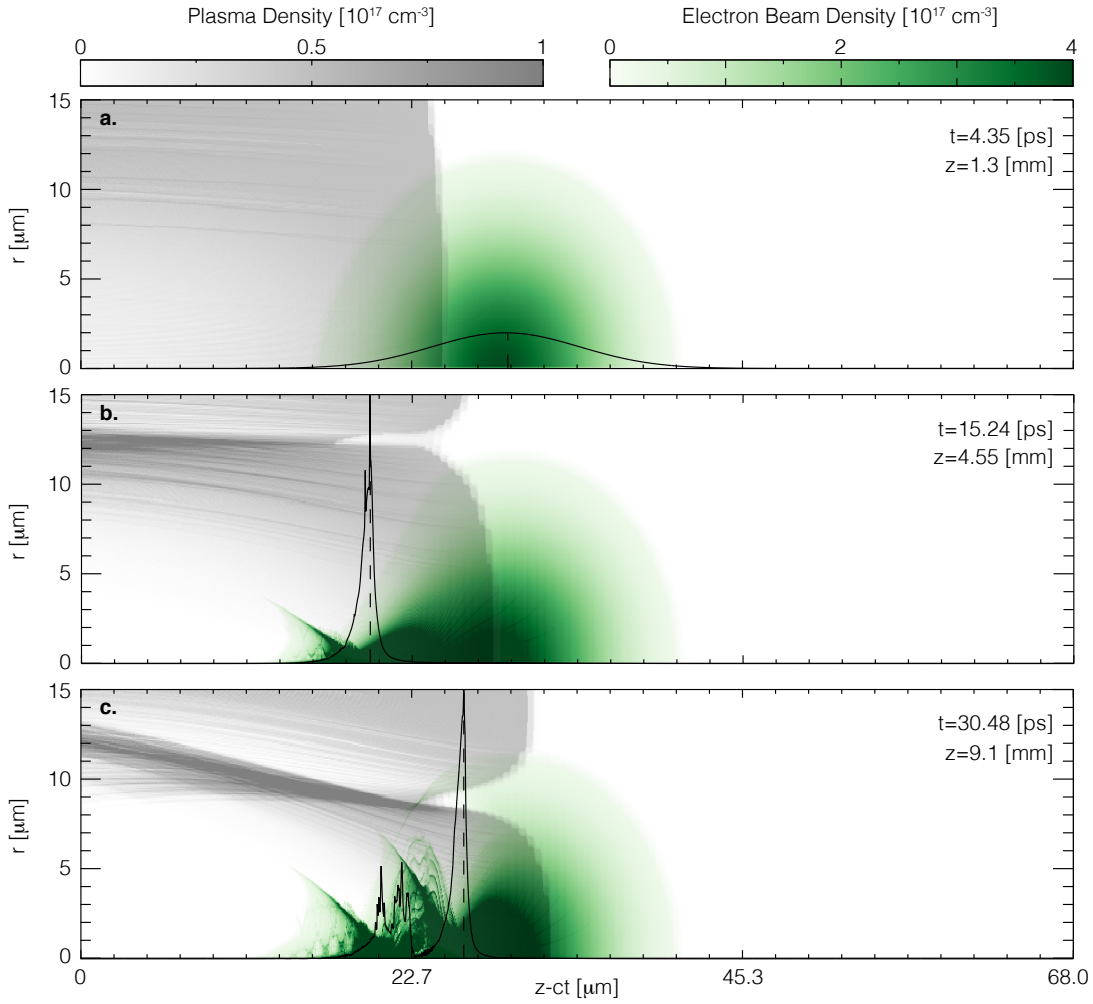

FIGURE 5.12: Snapshots of an OSIRIS simulation of the modulation of an electron beam via a superluminal pulse using Hydrogen gas at a) $t = 4.35$ ps, b) $t = 15.24$ ps, and c) $t = 30.48$ ps. Lineouts of the density on-axis are shown in every plot [Peak Density in a) 4×10^{17} cm^{-3}, b) 500×10^{17} cm^{-3} and c) 1600×10^{17} cm^{-3}. Vertical dashed lines at the peak density]. The ionizing laser pulse is not shown.

front. Because of the length-dependent start of the oscillation, a beam modulation appears.

We developed a theoretical model to get the correct modulation of the beam. Idealized simulations using external magnetic fields that provide the focusing force confirmed the theoretical results. As we moved to more realistic laser pulses, even though there were major differences from the ideal case, we still could measure 25 nm structures, which are already very close to X-ray wavelength.

We took the radiation emitted by the beam, which can be readily separated

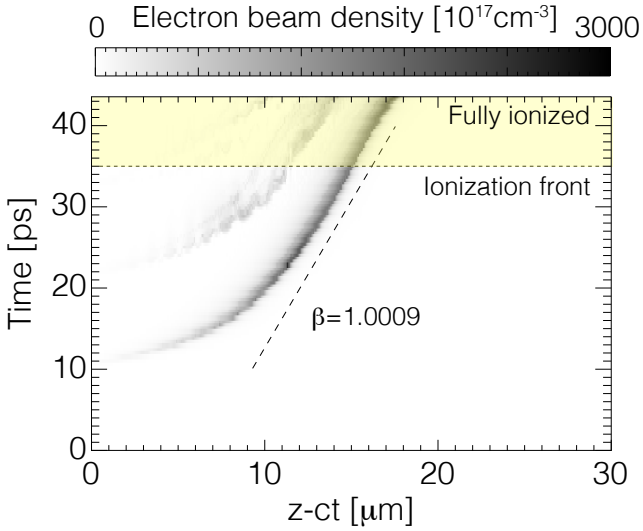

FIGURE 5.13: Waterfall plot of the electron beam density on-axis when propagating in Hydrogen. Marked in a dashed line is the speed of the ionization front ($\beta_m = 1.0009$). In this simulation, the electron beam starts interacting with a fully ionized plasma (instead of a superluminal ionization front) from $t = 35$ ps, which is shown in transparent yellow.

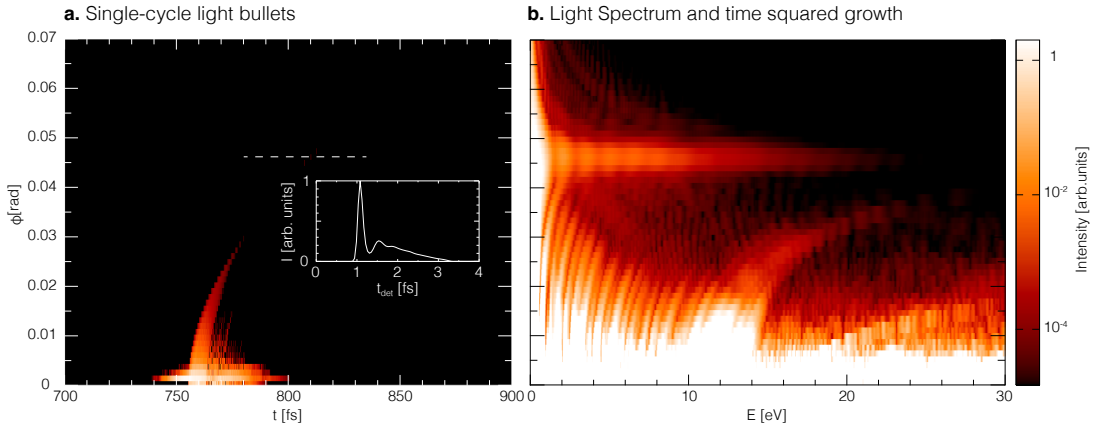

FIGURE 5.14: Spatiotemporal structure and spectrum of the emitted light using Hydrogen (simulation using an external field). a) Detected light in a detector in the far field. At angle $\phi = 0$ rad we observe the typical betatron radiation, with the length equal to the beam length. At the Cherenkov angle of the ionization front, we observe sub-fs single-cycle light pulse. b) Spectrum of the emitted light. On-axis we see the appearance of regular betatron radiation while a broadband signal appears off-axis.

into two parts. The first one propagates on-axis and it is related to the usual betatron radiation, which is incoherent and has the duration of the whole electron beam. The second one moves off-axis at the Cherenkov angle of the ionization front and is single-

cycle, superradiant, and broadband. We showed that this emission goes up to 20 eV.

As we proved in this chapter, by selecting smaller $(\beta_f - \beta_b)$, it is possible to increase the emitted frequencies. However, this makes simulations much harder to run in three different ways. Firstly, the resolution must increase to capture the current spike FWHM. Secondly, the time interval we need to simulate also increases, as the ionization front takes more time to overtake the beam. Thirdly, the transverse box size needs to increase as a property of a spatiotemporal pulse with the former characteristics. New injection methods are necessary to be able to shrink the transverse box size and simulate true X-ray production.

5.6 Papers in refereed journals

B. Malaca, K. Miller, J.P. Palastro and J. Vieira, Coherent Betatron Emission from Flying Foci setups, to be submitted (2024)

CHAPTER 6

CONCLUSIONS

6.1 SUMMARY

This thesis work started right before the first ever plasma-accelerated electrons were used in free-electron lasers. The amount of technological advances in the last few years points towards a future where radiation sources are powered by plasma sources, which translates into more funding for plasma physics and real impact in other fields, such as biology or material science. Our work tries to capitalize on all the advances from previous years and build a new set of possible coherent radiation sources with different properties than the ones already in existence.

In the first chapter, we developed a method that explores plasma density modulations to create superluminal current profiles. These current profiles can radiate as single entities, which led us to call them quasiparticles. If one can make the quasiparticle travel at precise speeds, the peak brightness from that quasiparticle can be as high as in an FEL. However, the scope of the work is even higher, as we could demonstrate also that an oscillating quasiparticle would radiate along the same spectrum lines as an FEL.

To realize the concept it is necessary to have very good control on the quasiparticle velocity and acceleration, as deviations stop the coherent process sooner. To do this, one must be able to precisely control the density profile in experiments. This automatically provides limits for 1) the time interaction during which the radiation is coherent, and 2) the total brightness. The quasiparticle radiation concept can enable a new class of temporally coherent, superradiant light sources. In the near term, quasiparticle radiation can be realized using existing experimental resources, and it is suitable for both LWFA and PWFA regimes. We showed coherent, single-cycle radiation up to 50 eV.

In the second chapter, we introduced spatiotemporal pulses in OSIRIS. One of the main properties of these pulses is the tunability of the group speed, which enables faster-than-light laser foci. We validated the implementation for both subluminal and superluminal pulses, showing that the pulses propagate diffraction-free and can self-heal when disturbed by an obstacle on-axis. We were also able to make them undergo selected trajectories, such as a sinusoid. We created an implementation of a 3D variation of the pulses, which allowed for further study of their interaction with plasma.

In the third chapter, the new class of lasers was used for two different applications, electron acceleration and radiation production. For acceleration, the use of superluminal plasma wakefields prevents dephasing and dark current, allowing acceleration of particles for larger distances. In these superluminal plasma wakefield setups, we observed good conditions for quasiparticle radiation. We showed how these pulses can enhance typical Thomson scattering configurations, increasing yield and brightness. This was mainly due to the possibility of accelerating the particle in the direction of the highest electric fields, instead of the usual deceleration in conventional cases.

In the last chapter, we studied one different class of radiation emission, which may allow coherent betatron radiation. We focused on flying foci pulses with low energy, as these can already be produced in the laboratory. With an electric field that is strong enough for ionization, the laser produces a superluminal ionization front as it travels through the gas. If we propagate an electron beam with the laser, the ionization front goes from the back to the head of the beam. The beam that travels on the plasma part of the configuration drives a nonlinear plasma wave that focuses the electron beam. This means that the betatron oscillations are started at a determined time and therefore they become coherent. The beam is conveniently modulated and quasiparticle radiation is also measured off-axis. We show that this emission can reach 70 eV, close to the X-ray limit. The coherent radiation is also off-axis, which means it is completely separated from the incoherent bit.

6.2 FUTURE DIRECTIONS

This work is purely theoretical and computational. Even though particle-in-cell simulations closely follow experimental results, only real experiments can show the real impact of these ideas. As for the quasiparticle radiation scheme, one can think of further implementations of the same method, without necessarily using the same parts that we used.

We proved that plasma setups can create single-cycle pulses very close to soft X-rays. It would be very important to get into the soft X-ray range, as that would mean a much different kind of pulse from the FEL. Since realistic flying foci are now

available in OSIRIS, it would be interesting to retackle some of the problems where we used idealized versions of these pulses.

In this work, we also developed a mini-diagnostic for radiation, as we used the current outputs from the simulations to estimate the total brightness. If this tool could be ported onto a particle-in-cell code, it would allow for quick estimates of the brightness and coherency at different timesteps. This would be more important for frequencies close to the Nyquist frequency, which may not be correctly propagated in the PIC simulation.

BIBLIOGRAPHY

[1] J.M. Cole, J.C. Wood, N.C. Lopes et al, Laser-wakefield accelerators as hard x-ray sources for 3D medical imaging of human bone, Scientific Reports **5**, 13244 (2015) https://doi.org/10.1038/srep13244

[2] Z. Wang, W. Yi, Q. Wu et al, Correlation between superconductivity and bond angle of CrAs chain in non-centrosymmetric compounds $A_2Cr_3As_3$ (A = K, Rb). Sci Rep **6**, 37878 (2016). https://doi.org/10.1038/srep37878

[3] J. M. Cole, K.T. Behm, E. Gerstmayr et al, Experimental Evidence of Radiation Reaction in the Collision of a High-Intensity Laser Pulse with a Laser-Wakefield Accelerated Electron Beam, Phys. Rev. X **8**, 011020 (2018) https://doi.org/10.1103/PhysRevX.8.011020

[4] David I Thwaites and John B Tuohy, Back to the future: the history and development of the clinical linear accelerator, Phys. Med. Biol. **51** R343 (2006) https://doi.org/10.1088/0031-9155/51/13/R20

[5] N. A. Solyak. Gradient limitations in room temperature and superconducting acceleration structures. AIP Conference Proceedings, **1086**(1):365-372, 2009. doi: 10.1063/1.3080933. http://aip.scitation.org/doi/abs/10.1063/1.3080933

[6] E. Esarey, C. B. Schroeder, and W. P. Leemans. Physics of laser-driven plasma-based electron accelerators. Rev. Mod. Phys. **81**:1229-1285 (2009) https://link.aps.org/doi/10.1103/RevModPhys.81.1229

[7] W. Lu, C. Huang, M. Zhou, W. Mori, and T. Katsouleas. Nonlinear theory for relativistic plasma wakefields in the blowout regime. Phys. Rev. Lett., 96(16):165002 (2006) https://doi.org/10.1103/PhysRevLett.96.165002

[8] T. Tajima and J. Dawson. Laser electron accelerator. Physical Review Letters, **43**(4):267-270, 1979. https://doi.org/10.1103/physrevlett.43.267

[9] P. Chen, J. M. Dawson, R. W. Huff, and T. Katsouleas. Acceleration of electrons by the interaction of a bunched electron beam with a plasma. Phys. Rev. Lett., **54**:693-696 (1985), https://doi.org/10.1103/PhysRevLett.54.693

[10] A. Caldwell, K. Lotov, A. Pukhov, and F. Simon. Proton-driven plasma-wakefield acceleration. Nature Physics **5**(5):363-367 (2009) https://doi.org/10.1038/nphys1248

[11] J. Rosenzweig, B. Breizman, T. Katsouleas, and J. Su. Acceleration and focusing of electrons in two-dimensional nonlinear plasma wake fields. Physical Review A, **44**(10):R6189 (1991) https://link.aps.org/doi/10.1103/PhysRevA.44.R6189

[12] J. P. Couperus Cabadağ et al, Gas-dynamic density downramp injection in a beam-driven plasma wakefield accelerator, Phys. Rev. Research **3**, L042005 (2021) https://doi.org/10.1103/PhysRevResearch.3.L042005

[13] Félicie Albert and Alec G R Thomas, Applications of laser wakefield accelerator-based light sources, Plasma Phys. Control. Fusion **58** 103001 (2016) https://dx.doi.org/10.1088/0741-3335/58/10/103001

[14] Eric Esarey, Sally K. Ride, and Phillip Sprangle, Nonlinear Thomson scattering of intense laser pulses from beams and plasmas, Phys. Rev. E **48**(4) 3003-3021 (1993) https://link.aps.org/doi/10.1103/PhysRevE.48.3003

[15] E. S. Sarachik and G. T. Schappert, Classical Theory of the Scattering of Intense Laser Radiation by Free Electrons, Phys. Rev. D **1**(10), 2737-2753 (1970) https://link.aps.org/doi/10.1103/PhysRevD.1.2738

[16] Brittni Pratt, Nicholas Atkinson, Daniel Hodge, Mahonri Romero, Christoph Schulzke, Yance Sun, Michael Ware, and Justin Peatross, Experimental confirmation of electron figure-8 motion in a strong laser field, Phys. Rev. A **103**(3) L031102 (2021) https://link.aps.org/doi/10.1103/PhysRevA.103.L031102

[17] E. Esarey, B. A. Shadwick, P. Catravas, and W. P. Leemans, Synchrotron radiation from electron beams in plasma-focusing channels, Phys. Rev. E **65**(5), 056505 (2002) https://link.aps.org/doi/10.1103/PhysRevE.65.056505

[18] M. J. Hogan, R. Assmann, F.-J. Decker, R. Iverson, P. Raimondi, S. Rokni, R. H. Siemann, D. Walz, D. Whittum, B. Blue, C. E. Clayton, E. Dodd, R. Hemker, C. Joshi, K. A. Marsh, W. B. Mori, S. Wang, T. Katsouleas, S. Lee, P. Muggli, P. Catravas, S. Chattopadhyay, E. Esarey, W. P. Leemans; E-157: A 1.4-m-long plasma wake field acceleration experiment using a 30 GeV electron beam from the Stanford Linear Accelerator Center Linac. Phys. Plasmas **7** (5): 2241-2248 (2000) https://doi.org/10.1063/1.874059

[19] Félicie Albert, Rahul Shah, Kim Ta Phuoc, Romuald Fitour, Fréderic Burgy, Jean-Philippe Rousseau, Amar Tafzi, Denis Douillet, Thierry Lefrou, and Antoine

Rousse, Betatron oscillations of electrons accelerated in laser wakefields characterized by spectral x-ray analysis, Phys. Rev. E **77** (5) 056402 (2008) https://link.aps.org/doi/10.1103/PhysRevE.77.056402

[20] J M Cole et al Tomography of human trabecular bone with a laser-wakefield driven x-ray source, Plasma Phys. Control. Fusion **58** 014008 (2016) https://doi.org/10.1088/0741-3335/58/1/014008

[21] S. Kneip, C. McGuffey, J. L. Martins, M. S. Bloom, V. Chvykov, F. Dollar, R. Fonseca, S. Jolly, G. Kalintchenko, K. Krushelnick, A. Maksimchuk, S. P. D. Mangles, Z. Najmudin, C. A. J. Palmer, K. Ta Phuoc, W. Schumaker, L. O. Silva, J. Vieira, V. Yanovsky, and A. G. R. Thomas; Characterization of transverse beam emittance of electrons from a laser-plasma wakefield accelerator in the bubble regime using betatron x-ray radiation, Phys. Rev. ST Accel. Beams **15**, 021302 (2012) https://link.aps.org/doi/10.1103/PhysRevSTAB.15.021302

[22] M. Heigoldt, A. Popp, K. Khrennikov, J. Wenz, S. W. Chou, S. Karsch, S. I. Bajlekov, S. M. Hooker, and B. Schmidt; Temporal evolution of longitudinal bunch profile in a laser wakefield accelerator, Phys. Rev. ST Accel. Beams **18**, 121302 (2015) https://doi.org/10.1103/PhysRevSTAB.18.121302

[23] C. B. Schroeder, E. Esarey, J. van Tilborg, and W. P. Leemans, Theory of coherent transition radiation generated at a plasma-vacuum interface, Phys. Rev. E **69**, 016501 (2004) https://doi.org/10.1103/PhysRevE.69.016501

[24] Wang, W., Feng, K., Ke, L. et al. Free-electron lasing at 27 nanometres based on a laser wakefield accelerator. Nature **595**, 516-520 (2021). https://doi.org/10.1038/s41586-021-03678-x

[25] M. Labat, J. Cabadag, A. Ghaith et al, Seeded free-electron laser driven by a compact laser plasma accelerator. Nat. Photon. 17, 150–156 (2023) https://doi.org/10.1038/s41566-022-01104-w

[26] R. Pompili, D. Alesini, M.P Anania, et al. Free-electron lasing with compact beam-driven plasma wakefield accelerator. Nature **605**, 659-662 (2022). https://doi.org/10.1038/s41586-022-04589-1

[27] I. Nam, CK. Min, B. Oh, et al. High-brightness self-seeded X-ray free-electron laser covering the 3.5 keV to 14.6 keV range. Nat. Photonics **15**, 435-441 (2021). https://doi.org/10.1038/s41566-021-00777-z

[28] R. H. Dicke, Coherence in Spontaneous Radiation Processes , Phys. Rev. **93**, 99 (1954).

[29] L. Giannessi, P. Musumeci, S. Spampinati; Nonlinear pulse evolution in seeded free-electron laser amplifiers and in free-electron laser cascades. J. Appl. Phys. **98** (4): 043110. (2005) https://doi.org/10.1063/1.2010624

[30] N.S. Mirian, M. Di Fraia, S. Spampinati, et al. Generation and measurement of intense few-femtosecond superradiant extreme-ultraviolet free-electron laser pulses. Nat. Photon. **15**, 523-529 (2021). https://doi.org/10.1038/s41566-021-00815-w

[31] H. Zen, R. Hajima, and H. Ohgaki, Full characterization of superradiant pulses generated from a free-electron laser oscillator. Sci Rep **13**, 6350 (2023). https://doi.org/10.1038/s41598-023-33550-z

[32] R. W. Warren, J. C. Goldstein, and B. E. Newnam, Spiking mode operation for a uniform-period wiggler. Nucl. Instrum. Methods A 250, 19-25 (1986) https://doi.org/10.1016/0168-9002(86)90854-5

[33] B. A. Richman, J. M. J. Maday, and E. Szarmes, First observation of spiking behaviour in the time domain in a free-electron laser. Phys. Rev. Lett. **63**, 1682 (1989) https://doi.org/10.1103/PhysRevLett.63.1682

[34] K. Yee, Numerical solution of initial boundary value problems involving maxwell's equations in isotropic media. IEEE Transactions on Antennas and Propagation, **14**(3):302-307 (1966) https://doi.org/10.1109/TAP.1966.1138693.

[35] R. A. Fonseca, L. O. Silva, F. S. Tsung, et al, OSIRIS: A Three-Dimensional, Fully Relativistic Particle in Cell Code for Modeling Plasma Based Accelerators, Lecture Notes in Computer Science (Springer, Berlin, Heidelberg, 2002), Vol. 2331. https://doi.org/10.1007/3-540-47789-6_36

[36] R. A. Fonseca, J. Vieira, F. Fiuza, et al, Exploiting multi-scale parallelism for large scale numerical modelling of laser wakefield accelerators, Plasma Phys. Control. Fusion **55**, 124011 (2013) https://doi.org/10.1088/0741-3335/55/12/124011

[37] J.L. Martins, S.F. Martins, R.A. Fonseca, L.O. Silva, Harnessing Relativistic Plasma Waves as Novel Radiation Sources from Terahertz to X-Rays and Beyond, **7359**, p. 73590V, SPIE (2009), https://doi.org/10.1117/12.820736

[38] H. Burau et al., PIConGPU: A Fully Relativistic Particle-in-Cell Code for a GPU Cluster, IEEE Transactions on Plasma Science **38** (10), 2831-2839 (2010) https://doi.org/10.1109/TPS.2010.2064310.

[39] M. Pardal, A. Sainte-Marie, A. Reboul-Salze et al, RaDiO: an efficient spatiotemporal radiation diagnostic for particle-in-cell codes, Comp. Phys. Communs **285** 108634 (2023) https://doi.org/10.1016/j.cpc.2022.108634

[40] A. Gover, Superradiant and stimulated-superradiant emission in prebunched electron-beam radiators. I. Formulation, Phys. Rev. ST-AB **8** 030701 (2005) https://doi.org/10.1103/PhysRevSTAB.8.030701

[41] Patrick G. O'Shea and Henry P. Freund, Free-Electron Lasers: Status and Applications, Science **292**, 1853 (2001). https://doi.org/10.1126/science.1055718

[42] A. Rousse, K. T. Phuoc, R. Shah et al, Production of a keV X-Ray Beam from Synchrotron Radiation in Relativistic Laser-Plasma Interaction, Phys. Rev. Lett. **93**, 135005 (2004). https://link.aps.org/doi/10.1103/PhysRevLett.93.135005

[43] S. Kneip, C. McGuffey, J. L. Martins et al, Bright spatially coherent synchrotron X-rays from a table-top source, Nature Physics **6**, 980 (2010) https://doi.org/10.1038/nphys1789

[44] J. C. Wood, D. J. Chapman, K. Poder et al., Ultrafast Imaging of Laser Driven Shock Waves using Betatron X-rays from a Laser Wakefield Accelerator, Scientific Reports **8**, 11010 (2018) https://doi.org/10.1038/s41598-018-29347-0

[45] Z.-H. He, B.Beaurepaire, J.A.Nees, et al, Capturing Structural Dynamics in Crystalline Silicon Using Chirped Electrons from a Laser Wakefield Accelerator, Scientific Reports **6**, 36224 (2016) https://doi.org/10.1038/srep36224

[46] F. Albert, A.G.R. Thomas, S.P.D. Mangles et al, Laser wakefield accelerator based light sources: potential applications and requirements, Plasma Phys. Control. Fusion **56**, 084015 (2014) https://doi.org/10.1088/0741-3335/56/8/084015

[47] W. T. Wang, W. T. Li,J. S. Liu et al, High-Brightness High-Energy Electron Beams from a Laser Wakefield Accelerator via Energy Chirp Control, Phys. Rev. Lett. **117** 124801 (2015) https://doi.org/10.1103/PhysRevLett.117.124801

[48] X. Davoine, F. Fiúza, R.A. Fonseca et al, Ion-channel laser growth rate and beam quality requirements, Journal Plasma Phys. **84**, 905840304 (2018) https://doi.org/10.1017/S0022377818000429

[49] J. Vieira, M. Pardal, J.T. Mendonça et al, Generalized superradiance for producing broadband coherent radiation with transversely modulated arbitrarily diluted bunches, Nature Physics **17**, 99-104 (2021) https://doi.org/10.1038/s41567-020-0995-5

[50] J. Xu, A. Buck, S.-W. Chou et al, Dynamics of electron injection in a laser-wakefield accelerator, Phys. Plasmas **24**, 083106 (2017) https://doi.org/10.1063/1.4996906

[51] J. Wenz, A. Dopp, K. Khrennikov et al, Dual-energy electron beams from a compact laser-driven accelerator, Nature Photonics **13**, 263 (2019) https://doi.org/10.1038/s41566-019-0356-z

[52] A. Fedenev, A. Morozov, R. Krücken et al, Applications of a broadband electron-beam pumped XUV radiation source, J. Phys. D:Appl. Phys. **37**, 1586 (2004) https://doi.org/10.1088/0022-3727/37/11/013

[53] B. Cline, I. Delahunty, J. Xie, Nanoparticles to mediate X-ray-induced photodynamic therapy and Cherenkov radiation photodynamic therapy, WIREs Nanomed. Nanobiotechnol. **11**, e1541 (2019) https://doi.org/10.1002/wnan.1541

[54] Classical Electrodynamics, Ch. 14, page 676, J.D.Jackson, 3rd edition, John Wiley & Sons Inc

[55] Wan, Y., Tata, S., Seemann, O. et al. Femtosecond electron microscopy of relativistic electron bunches. Light Sci Appl **12**, 116 (2023). https://doi.org/10.1038/s41377-023-01142-1

[56] Wan, Y., Seemann, O., Tata, S. et al. Direct observation of relativistic broken plasma waves. Nat. Phys. **18**, 1186-1190 (2022). https://doi.org/10.1038/s41567-022-01717-6

[57] A. Pukhov, J. Meyer-ter-Vehn, Appl. Phys. B **74**, 355 (2002).

[58] W. Lu, C. Huang, M. Zhou et al, Nonlinear Theory for Relativistic Plasma Wakefields in the Blowout Regime, Phys. Rev. Lett. **96**, 165002 (2006) https://doi.org/10.1103/PhysRevLett.96.165002

[59] M. Burza, A. Gonoskov, K. Svensson et al, Laser wakefield acceleration using wire produced double density ramps, Phys. Rev ST AB **16**, 011301 (2013) https://doi.org/10.1103/PhysRevSTAB.16.011301

[60] C.G.R. Geddes, K. Nakamura, G.R. Plateau et al, Plasma-Density-Gradient Injection of Low Absolute-Momentum-Spread Electron Bunches, Phys. Rev. Lett. **100**, 215004 (2008) https://doi.org/10.1103/PhysRevLett.100.215004

[61] A.J. Gonsalves, K. Nakamura, C. Lin et al, Tunable laser plasma accelerator based on longitudinal density tailoring, Nature Physics **7**, 862 (2011) https://doi.org/10.1038/nphys2071

[62] M. P. Tooley, B. Ersfeld, S. R. Yoffe et al, Towards Attosecond High-Energy Electron Bunches: Controlling Self-Injection in Laser-Wakefield Accelerators Through Plasma-Density Modulation, Phys. Rev. Lett. **119**, 044801 (2017) https://doi.org/10.1103/PhysRevLett.119.044801

[63] H. Suk, N. Barov, J.B. Rosensweig et al, Plasma Electron Trapping and Acceleration in a Plasma Wake Field Using a Density Transition, Phys. Rev. Lett. **86**, 1011 (2001) https://doi.org/10.1103/PhysRevLett.86.1011

[64] A. Martinez de la Ossa, Z. Hu, M.J.V. Streeter et al, Optimizing density downramp injection for beam-driven plasma wakefield accelerators, Phys. Rev. Accel. Beams **20**, 091301 (2017) https://doi.org/10.1103/PhysRevAccelBeams.20.091301

[65] X.L. Xu, F. Li, W. An et al, High quality electron bunch generation using a longitudinal density-tailored plasma-based accelerator in the three-dimensional blowout regime, Phys. Rev. Accel. Beams **20**, 111303 (2017) https://journals.aps.org/prab/abstract/10.1103/PhysRevAccelBeams.20.111303

[66] C. Zhang, C.-K. Huang, K. Marsh et al, Effect of fluctuations in the down ramp plasma source profile on the emittance and current profile of the self-injected beam in a plasma wakefield accelerator, Phys. Rev. Accel. Beams **22**, 111301 (2019) https://doi.org/10.1103/PhysRevAccelBeams.22.111301

[67] J. P. Palastro, B. Malaca, J. Vieira, D. Ramsey, T. T. Simpson, P. Franke, J. L. Shaw, D. H. Froula; Laser-plasma acceleration beyond wave breaking, Phys. Plasmas **28** (1): 013109 (2021) https://doi.org/10.1063/5.0036627

[68] C. Zhang, Z. Nie, Y. Wu et al, Ionization induced plasma grating and its applications in strong-field ionization measurements, Plasma Phys. Control. Fusion **63**, 095011 (2021) https://doi.org/10.1088/1361-6587/ac1751

[69] B. D. Layer, A. York, T. M. Antonsen et al, Ultrahigh-Intensity Optical Slow-Wave Structure, Phys. Rev. Lett. **99**, 035001 (2007) https://doi.org/10.1103/PhysRevLett.99.035001

[70] B. D. Layer, A. G. York, S. Varma et al, Periodic index-modulated plasma waveguide, Optics Express **17**, 4263 (2009) https://doi.org/10.1364/OE.17.004263

[71] A. Sainte-Marie, O. Gobert, and F. Quéré, Controlling the velocity of ultrashort light pulses in vacuum through spatio-temporal couplings, Optica **4**, 1298 (2017) https://doi.org/10.1364/OPTICA.4.001298

[72] D.H. Froula, D. Turnbull, A. S. Davies et al, Spatiotemporal control of laser intensity, Nat. Photonics **12**, pages 262-265 (2018) https://doi.org/10.1038/s41566-018-0121-8

[73] J. P. Palastro, J. L. Shaw, P. Franke, D. Ramsey, T. T. Simpson, and D. H. Froula, Dephasingless Laser Wakefield Acceleration, Phys. Rev. Lett. **130**, 159902 (2020) https://doi.org/10.1103/PhysRevLett.124.134802

[74] Jacob R. Pierce, John P. Palastro, Fei Li et al, Arbitrarily structured laser pulses, Phys. Rev. Research **5**. 013085 (2023) https://doi.org/10.1103/PhysRevResearch.5.013085

[75] D. Ramsey, P. Franke, T.T. Simpson et al, Vacuum acceleration of electrons in a dynamic laser pulse, Phys. Rev. E **102**, 043207 (2020) https://doi.org/10.1103/PhysRevE.102.043207

[76] X. Shi, X. Lin, I. Kaminer et al, Superlight inverse Doppler effect, Nature Physics **14**, 1001 (2018) https://doi.org/10.1038/s41567-018-0209-6

[77] J. Vieira, J. T. Mendonça and F. Queré, Optical Control of the Topology of Laser-Plasma Accelerators, Phys Rev Lett **121**(5) 054801 (2018) https://link.aps.org/doi/10.1103/PhysRevLett.121.054801

[78] Kondakci, H.E., Abouraddy, A.F. Optical space-time wave packets having arbitrary group velocities in free space. Nat Commun **10**, 929 (2019) https://doi.org/10.1038/s41467-019-08735-8

[79] M. Yessenov and Ayman F. Abouraddy, Accelerating and Decelerating Space-Time Optical Wave Packets in Free Space, Phys. Rev. Lett. **125** 233901 (2020) https://doi.org/10.1103/PhysRevLett.125.233901

[80] M. V. Ambat, J. L. Shaw, J. J. Pigeon, K. G. Miller, T. T. Simpson, D. H. Froula, and J. P. Palastro, Programmable-trajectory ultrafast flying focus pulses, Opt. Express **31**, 31354-31368 (2023)

[81] J. P. Palastro, B. Malaca, J. Vieira, D. Ramsey, T. T. Simpson, P. Franke, J. L. Shaw, D. H. Froula; Laser-plasma acceleration beyond wave breaking. Physics of Plasmas **28** (1): 013109 (2020) https://doi.org/10.1063/5.0036627

[82] P. Sprangle, A. Ting, E. Esarey, A. Fisher; Tunable, short pulse hard x-rays from a compact laser synchrotron source. J. Appl. Phys. **72** (11): 5032–5038 (1992) https://doi.org/10.1063/1.352031

[83] E. Esarey, Sally K. Ride and Phillip Sprangle, Nonlinear Thomson scattering of intense laser pulses from beams and plasmas, Physical Review E **48** 3003-3021 (1993); https://doi.org/10.1103/PhysRevE.48.3003

[84] Sy., Chen, A. Maksimchuk, and D. Umstadter, Experimental observation of relativistic nonlinear Thomson scattering. Nature **396**, 653–655 (1998). https://doi.org/10.1038/25303

[85] Ramsey, D. and Malaca, B. and Di Piazza, A. and Formanek, M. and Franke, P. and Froula, D. H. and Pardal, M. and Simpson, T. T. and Vieira, J. and Weichman, K. and Palastro, J. P., Physical Review E **105** 6-065201 (2022) https://link.aps.org/doi/10.1103/PhysRevE.105.065201

[86] K. Weichman, K.G. Miller, B. Malaca, W.B. Mori, J.R. Pierce, D. Ramsey, J. Vieira, M. Vranic, J.P. Palastro, Analytic pulse technique for computational electromagnetics, Computer Physics Communications **298** 109096 (2024) https://doi.org/10.1016/j.cpc.2024.109096

[87] K.G. Miller, J.R. Pierce, M.V. Ambat, et al. Dephasingless laser wakefield acceleration in the bubble regime. Sci Rep **13**, 21306 (2023). https://doi.org/10.1038/s41598-023-48249-4

[88] A. Davidson, A. Tableman, W. An, F.S. Tsung, W. Lu, J. Vieira, R.A. Fonseca, L.O. Silva, W.B. Mori, Implementation of a hybrid particle code with a PIC description in r-z and a gridless description in ϕ into OSIRIS, Journal of Computational Physics **281**, 1063-1077 (2015) https://doi.org/10.1016/j.jcp.2014.10.064

[89] M. V. Berry, N. L. Balazs; Nonspreading wave packets. Am. J. Phys. **47** (3): 264–267 (1979) https://doi.org/10.1119/1.11855

[90] C. E. Clayton, B. E. Blue, E. S. Dodd, C. Joshi, et al; Transverse Envelope Dynamics of a 28.5-GeV Electron Beam in a Long Plasma; Phys. Rev. Lett. **88**, 154801 (2002) https://doi.org/10.1103/PhysRevLett.88.154801

[91] Aaron Liberman, Ronan Lahaye, Slava Smartsev, Sheroy Tata, Salome Benracassa, Anton Golovanov, Eitan Levine, Cedric Thaury, and Victor Malka, Optics Letters **49** (4): 814-817 (2024) https://doi.org/10.1364/OL.507713

[92] Slava Smartsev, Clément Caizergues, Kosta Oubrerie, Julien Gautier, Jean-Philippe Goddet, Amar Tafzi, Kim Ta Phuoc, Victor Malka, and Cédric Thaury, Axiparabola: a long-focal-depth, high-resolution mirror for broadband high-intensity lasers, Optical Letters **44** (14):3414-3417 (2019) https://doi.org/10.1364/OL.44.003414

[93] P. A. Cherenkov, Visible emission of clean liquids by action of γ radiation, Doklady Akademii Nauk SSSR **2**: 451 (1934)